Doctoral Dissertation

Diagnosis of the Blowing Snow Potential and Development of a Snowdrift Model with the Lattice Boltzmann Method

吹雪発生可能性の診断と格子ボルツマン法を用いた吹きだまりモデルの開発

Seika Tanji

丹治　星河

Division of Earth and Planetary Dynamics, Department of Natural History Sciences,

Graduate School of Science, Hokkaido University

北海道大学大学院理学院自然史科学専攻

地球惑星ダイナミクス講座

2023 年 3 月

Abstract

Transport of snow particles by blowing and drifting snow contributes to the snow surface formation in cold regions. Blowing and drifting snow are also important phenomena for the traffic engineering because they cause low visibility and snowdrifts which can be obstacles to drivers. In the former part of this doctoral dissertation, we diagnosed blowing snow potential for typical blowing snow cases around Sapporo, Japan. We calculated snow concentration and visibility by dynamically downscaled meteorological data with 1-km resolution. The results were consistent with the blowing-snow records on time and place of traffic disruption when the dynamical downscaling (DDS) reproduced wind speed well for cases. The diagnosis with mesoscale model analysis with 5-km resolution did not reproduce the blowing snow events in most areas, however. Hence, the DDS potentially, not perfectly, added value to estimate blowing snow potential, despite a large-scale gap from an explicit representation of small-scale turbulence related to blowing snow. Sensitivity tests clarified that blowing snow required strong wind and freezing temperature at the surface.

We developed a new snowdrift model to evaluate snowdrifts around snow fences in the latter part of this doctoral dissertation. The model consisted of the conventional computational fluid dynamics (CFD) solver and a module for tracing snow particles with the Lagrangian method. The lattice Boltzmann method was used as the CFD solver for the first time in the snowdrift simulation model in order to calculate turbulent flow with high parallel performance. The estimated wind flow over the two-dimensional fence was characterized by a swirling eddy in the cross-section, whereas the wind flow in the three-dimensional fence experiment was horizontally diffluent with a dipole vortex pair on the leeward side of the fence. Almost all the snowdrifts formed on the windward side of the two-dimensional and three-dimensional fences, although the

snowdrift also formed along the split streaks on the leeward side of the three-dimensional fence. These results were qualitatively similar to the results of the previous of observational and modeling studies. The three-dimensional fence experiment was also conducted with the inflow boundary condition which was based on the observed wind speed during a drifting snow event. In order to compare the result of the experiment with the 1-dimensional snowdrift height in the observation quantitatively, we imposed the model with the sub-processes of drifting snow particles, such as the resuspension and rebound processes. The snowdrift estimated by the model could reproduce the features of the observed snowdrift, such as the peak height and the peak position on the windward of the fence because the snow particle module calculated sub-processes of drifting snow particles explicitly. Sensitivity tests indicated that the snowdrift distribution was clearly dependent on the physical properties of snow particles which decided the potential of the accumulated snow particles' resuspension. The snowdrift model developed in this doctoral dissertation is expected to be used to simulate snowdrift distribution not only around roads and fences in the traffic engineering motivation but also on the mountainous terrain in the earth science motivation where snowdrift can trigger avalanches and affect the mass balance of water.

日本語要旨

吹雪による雪粒子の移動は寒冷地域における雪面の形成に寄与する. 吹雪はドライバーにとって障害となる視程障害や吹きだまりをもたらすため, 交通工学の分野でも重要な現象である.

本博士論文の前半では, 札幌周辺の典型的な吹雪事例に対して吹雪発生可能性を診断した．まず，力学的ダウンスケーリングを施した 1 km 解像度の気象データを用いて雪粒子空間濃度と視程を計算した．その結果は，力学的ダウンスケーリングによって風速が良く再現された場合について, 吹雪発生の場所と時刻が吹雪による交通障害の記録とよく一致した．次に，5 km 解像度のメソ解析データを使用して診断した．その結果，多くの地点で吹雪事例を再現できなかった．よって，吹雪発生は小さなスケールの乱流によってもたらされるにもかかわらず, 力学的ダウンスケーリングは吹雪発生可能性の推定に関して付加価値があるということが分かった．感度実験では，吹雪は強い風と氷点下の気温によってもたらされるということが明らかになった.

本博士論文の後半では, 防雪柵まわりに形成される吹きだまり分布を推定するための吹きだまりモデルを開発した．このモデルは，数値流体計算(CFD)を行うモジュールと, ラグランジュ的手法を用いて雪粒子を追跡するモジュールとで構成されている. 計算に必要な数 cm 程度の解像度の計算を効率よく実施するために，並列化効率が高い格子ボルツマン法を CFD モジュールとして使用して乱流の計算を行った．モデルによって推定された 2 次元フェンスまわりにおける風の流れは, 鉛直断面で渦巻くという特徴を持っていた．一方，3 次元フェンス周りでは，鉛直断面の渦に加え，水平断面に対となる渦の組が現れた．吹きだまりは，2 次元フェンスまわりでも 3 次元フェンスまわりでもほとんどが風上側で形成された．しかし，3 次元フェンスまわりでは，フェンスの端から枝分かれした吹きだまりが風下で形成された. このような吹きだまりの結果は, 先行研究の観測結果やモデルの結果と定性的に一致する．3 次元フェンスについては, 吹雪イベント中に観測された風速や雪粒子の流入量を境界条件とした実験も行った. フェンス中央の吹きだまりの高さを観測結果とモデルの結果で定量的に比較するために, 再飛散過程やリバウンド過程といった吹雪粒子のサブプロセスをモデルに組み込んだ.

その結果，モデルによる推定は．フェンス風上で観測された吹きだまりのピークの高さや位置をよく再現できた．これは，雪粒子モジュールで吹雪粒子のサブプロセスを陽に解いたためである．感度実験を行うと，積雪粒子の再飛散の起こりやすさを決定する雪粒子の物性が，吹きだまりの分布に大きく寄与するということが明らかになった．本博士論文で開発されたモデルは，交通工学における道路や柵まわりの吹きだまりだけでなく，地球科学における山岳地域の吹きだまりのシミュレーションにも使用されることが期待される．

Table of contents

Chapter 1. General Introduction

The snow and ice science is one of the academic fields of the earth science. It targets snow crystals, snowfall, snowpack, glaciers, ice sheets, frozen soil, and sea ice. Most of subjects in the snow and ice science have a common interest in snow cover distribution through snow accumulation. Snow accumulation is produced by not only snowfall particles but also drifting and blowing snow particles. Drifting and blowing snow are the horizontal movements of snow particles by the strong wind. Drifting snow particles move at a low level above the surface mainly by creep and saltation and blowing snow particles move at a high level above the surface mainly by a suspension (Fig. 1.1). Snowfall particles blown by the strong wind are also called blowing snow particles. Horizontal movement of snow particles by drifting and blowing snow is important in the snow and ice science because they often cause inhomogeneous snow cover distribution, so-called snowdrifts. In polar regions such as the Antarctic, snowdrifts by drifting and blowing snow plays an important role in storing water resources (Lehning et al. 2006; Lehning et al. 2008; Mott

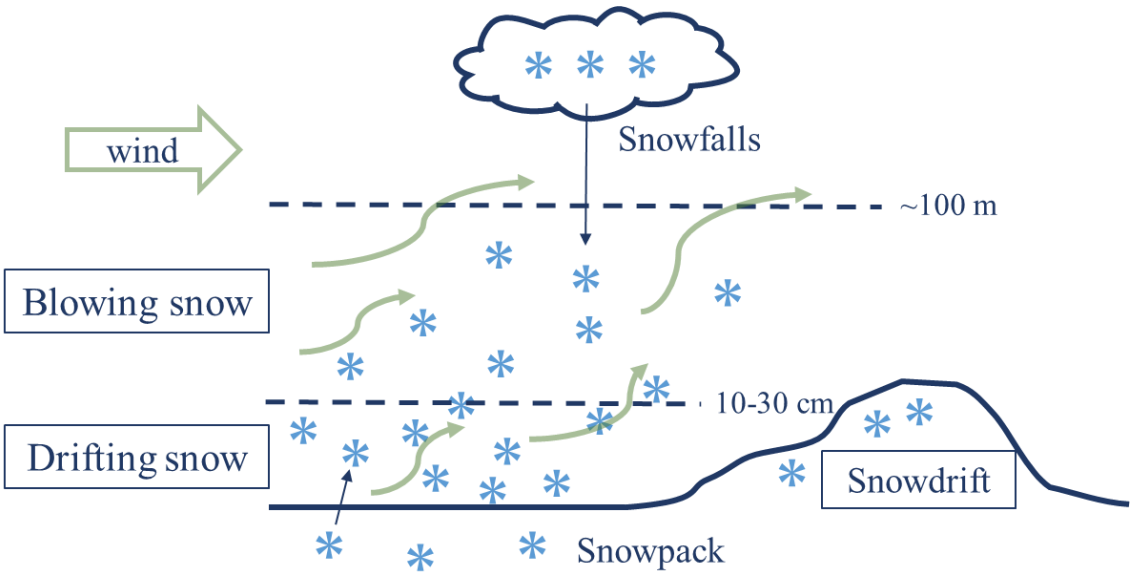

Fig. 1.1. Schematic of blowing and drifting snow and snowdrift. Star marks display snow particles.

et al. 2010; Vionnet et al. 2017). Snowdrifts in the mountainous area can trigger avalanches and cause snow cornices. Many previous studies were devoted to drifting and blowing snow mechanisms mainly in polar regions and mountainous areas with observation (Nemoto and Nishimura 2004; Nishimura et al. 2014), wind tunnel experiments (Delpech et al. 1998), and numerical simulations (Nemoto and Nishimura 2004; Zwaaftink et al. 2014; Ohara et al. 2022).

Drifting and blowing snow are important phenomena not only in the earth science but also in the traffic engineering in cold regions because drifting and blowing snow often cause traffic disruptions. For example, two traffic accidents involving 25 cars happened due to low visibility by drifting and blowing snow on expressways in Hokkaido, Japan on Feb 24 in 2016, and a express was closed for a long time. From Mar 2 to 3 in 2013, there were eight casualties due to carbon monoxide poisoning in the cars and froze to death on the outside because cars were filled with snowdrifts and got stuck. Drifting and blowing snow particles have a feature that the instantaneous increase of transport amount of them is generally larger than that of snowfall particles (Matsuzawa and Takeuchi 2002). In order to defend people on roads from these drifting and blowing snow disasters, some previous studies investigated wind speed, snow concentration and snow-drift flux during drifting and blowing snow events. Visibility can be estimated by the snow-drift flux because incidental image of snow particles or sunlight attenuation due to snow particles are considered the reason for low visibility during drifting and blowing snow events (Saito 1971; Takeuchi and Fukuzawa 1976; Matsuzawa and Takeuchi 2002). Large transport amount of snow particles also makes snowdrifts on roads which cause vehicles to stack and stagnate on roads even with a snow depth of 15 cm (Kaneko et al. 2011). Therefore, some previous studies set snow fences beside the road to protect roads from snowdrift formation and evaluated the fences with observation (Tabler 1980; Takeuchi 1980; Takeuchi et al. 1986; Tabler 1994), wind tunnel experiments (Iversen 1981; Takeuchi et al. 2001) and numerical simulation (Beyers

et al. 2004; Tominaga et al. 2011a, 2011b; Zwaaftink et al. 2014; Okaze et al. 2018; Wang and Jia 2018; Zhang et al. 2021).

Wind speed around the surface is a primary cause of drifting and blowing snow and contributes to the transport amount of snow particles. In order to estimate the transport amount of snow particles due to drifting and blowing snow, the meteorological model output such as wind speed in the upper air is a powerful tool for diagnosis of the drifting and blowing snow potential because wind speed around the surface is dependent on the meso-scale wind profile. Wind speed around the surface is also influenced by landforms. However, operated methods of the blowing and drifting snow estimation use the meteorological data with 5-km resolution at best and did not consider the influence of under 5-km-scale landforms (http://www.northern-road.jp/navi/touge/fubuki.htm). In this operating system, we could not estimate sudden and local drifting and blowing snow development which causes low visibility and snowdrifts on roads. In order to overcome this point, acquiring meteorological data with higher resolution is required because simulation with higher resolution brought better representation of the model terrain (Takemi and Ito 2020).

When the transport amount of snow particles due to drifting and blowing snow is diagnosed in the macroscopic scale, snowdrift formation around roads should be estimated. Snowdrift formation around roads depends on the wind profiles with a smaller scale, such as tens of centimeters to tens of meters which is the microscopic scale. In this scale, not only landforms but also buildings and obstacles contribute to wind profiles and snowdrift distributions. Therefore, the turbulent flow around the surface should be researched to estimate snowdrift distribution. Studies of numerical simulation in drifting and blowing snow increase with advance of the computer technology because numerical simulation has an advantage (Uematsu et al. 1991; Liston et al. 1993; Beyers et al. 2004; Tominaga et al. 2011a, 2011b; Zwaaftink et al. 2014; Okaze et al.

2018; Wang and Jia 2018; Zhang et al. 2021). The numerical simulation is independent of limited opportunities of drifting snow events in the observation and frees us from the presence of the facilities and scaling effects in the wind tunnel experiments. These previous studies of the numerical simulation calculated the turbulent wind flow with some conventional fluid dynamics (CFD) methods such as the Reynolds-averaged Navier–Stokes equations (RANS) and the large-eddy simulation (LES). Some studies which target to investigate drifting snow mechanism combined the CFD methods and the Lagrangian method to trace drifting snow particles. However, these previous CFD methods and tracing snow particles methods required a large computational cost were not suitable for simulating snowdrifts formation. Therefore, previous studies of the numerical snowdrift simulation model did not calculate turbulent flow and snow particles' trajectories explicitly. The lattice Boltzmann method, one of the CFD method, has potential to overcome these problems due to its higher efficiency in parallel computation and suitability for complicated boundary conditions.

In this study, the development of drifting and blowing snow events are diagnosed with the meteorological data, and a numerical simulation model for snowdrift formation is developed. The former part contains a single chapter (Chapter 2) based on Tanji and Inatsu (2019). Blowing and drifting snow development was estimated by the data of wind speed, temperature, and snowfall around the surface which were resolved with the dynamical downscaling. The latter part of this thesis consists of Chapter 3 based on Tanji et al. (2021) and Chapter 4. The numerical simulation model of snowdrifts was developed which used the lattice Boltzmann method as the CFD method and the sensitivity tests of the model were conducted. Chapter 5 provides a general summary of this thesis.

Chapter 2. Blowing Snow Potential Diagnosis

2.1. Introduction

Blowing snow is a phenomenon that strong wind resuspends surface snow particles or blows snowfall particles. Blowing snow brings disasters such as traffic accidents due to low visibility and avalanches on a slope due to snow cornices accompanied by snowdrifts. Moreover, it significantly transports water mass in Antarctica, with less precipitation and strong downslope wind. Blowing snow is thus worth simulating or diagnosing for not only natural science but also disaster mitigation.

Studies on blowing snow simulation have emphasized resolving turbulent surface flow at a single site such as a flat field in Antarctica (Nemoto and Nishimura 2004) and a mountainous spot in the Alps (Zwaaftink et al. 2014). Another simulation study in a technology field investigated the block effect of an artificial snow fence in Japan (Uematsu et al. 1991). These simulations explicitly coped with the turbulent flow essential for the generation and maintenance of blowing snow with a sub-kilometer horizontal scale. On the other hand, a forecast of blowing snow or its potential over a much wider area may provide helpful information for disaster mitigation. Though an explicit calculation of sub-kilometer turbulence with blowing snow could hardly expand to wide-area forecasting due to computational cost, blowing snow potential with a horizontal scale of about 1 km can be diagnosed with background wind speed, snowfall intensity, and surface air temperature (Shiotani 1953; Matsuzawa and Takeuchi 2002). Such a diagnostic forecast of blowing snow has been operated in some parts of Hokkaido, Japan (http://www.northern-road.jp/navi/touge/fubuki.htm), based on coarse-resolution weather forecast data with at most 5-km grid mesh. In Canadian Prairies, seasonal snow accumulation is operated with the Prairie Blowing Snow Model (Pomeroy et al. 1993). In Switzerland,

Alpine3D/SNOWPACK chain has been introduced to snow cover dynamics for avalanche warning and permafrost development and applied to the Swiss Alps (Lehning et al. 2006). In France, SAFRAN/Crocus/MEPRA chain by Météo France was developed to evaluate avalanche risks in French Alps (Durand et al. 1999) and has been recently improved the resolution (Durand et al. 2005).

Dynamical downscaling (DDS) is a powerful method to create high-resolution physically-consistent data with a limited-area atmospheric model formulating a Reynolds averaging or a large eddy simulation (Wang et al. 2004). In cryology, downscaling has been used to evaluate snow accumulation change (Cayan et al. 2008), snow metamorphosis (Katsuyama et al. 2017), and glacier distribution (Akhtar et al. 2008). Many studies were also conducted on water-mass redistribution in a snow-covered mountainous region and around the river (Vionnet et al. 2017; Bernhardt et al. 2010; Lehning et al. 2008; Nijssen et al. 2001). A large-scale gap between turbulence on blowing snow and weather forecast data makes it difficult to explicitly resolve blowing snow with downscaling. However, downscaling expectedly improves the resolution of background wind speed, snowfall intensity, and surface temperature by high-resolution topography imposed as the model boundary. The blowing snow potential could be thus better estimated with the diagnostics based on the high-resolution downscaled data, yet this kind of study have not been conducted in the estimation of blowing snow potential.

The chapter aims to investigate the advantage of the downscaled data in the blowing snow estimation. In order to make it clear, we diagnosed blowing snow potential around Sapporo, Japan, for two typical cases. Because no dense monitoring network for the direct detection of blowing snow is operated over Hokkaido, we choose the cases with a blowing snow record on traffic problems. The comparison between the estimates based on 1-km resolution DDS data and that based on the original mesoscale-model analysis with 5-km resolution moreover reveals an

added value of DDS. we also estimated visibility with an empirical relation to snow concentration and wind speed. The results are validated with a blowing-snow record related to traffic problems with an aid of meteorological observation at sites near the traffic problems. Sensitivity tests clarify the impact of wind speed, snowfall intensity, and surface air temperature.

2.2. Data and Method

We used the 3-hourly MesoScale Model (MSM) analysis provided by the Japan Meteorological Agency (JMA) with the horizontal grid mesh of 5 km (Saito et al. 2006). The DDS was performed with Scalable Computing for Advanced Library and Environment (SCALE; Nishizawa et al. 2015; Sato et al. 2015) developed in RIKEN Center of Computational Science (R-CCS), Japan, with the MSM analysis prescribed as initial and boundary conditions. We used the six-class one-moment bulk scheme (Tomita et al. 2008) as a cloud micro-physics scheme, the hybrid use of the boundary layer parameterization (Smagorinsky 1963; Lilly 1962; Brown et al. 1994; Scotti et al. 1993) and sub-grid scale turbulence model (Mellor and Yamada 1982; Nakanishi and Niino 2004) as a turbulence scheme, and the single-layer canopy model (Kusaka et al. 2001) as an urban model. The model domain was 141.0°E – 141.8°E by 42.7°N – 43.4°N, including three cities of Sapporo, Kita-Hiroshima, and Eniwa (Fig. 2.1). We set the horizontal gird mesh to 1 km, the vertical layers of 32, the model top was 19,981 m, and the output time interval of 1 hour.

We performed a 72-hour model integration each for two blowing-snow cases on 6 Jan 2018 and on 24 Feb 2016. The first date included a close of the same expressway between Sapporo and Eniwa from 0835 UTC because of low visibility, and the second date included a traffic accident on the Hokkaido Expressway in Kita-Hiroshima city at 0245 UTC. For an indirect validation, we used the AMeDAS (Automated Meteorological Data Acquisition System) data at

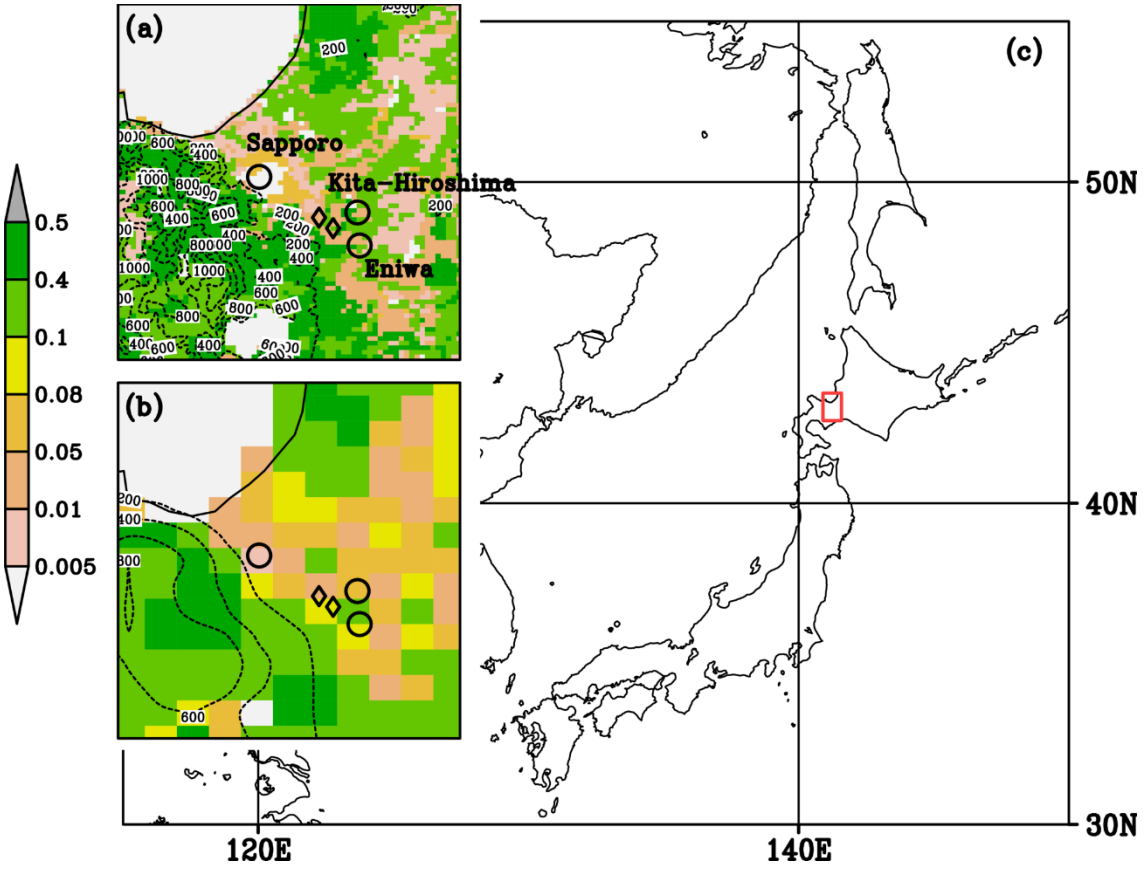

Fig. 2.1. (a,b) Surface height (contour interval is 200 m) and roughness length (m; shading as per the reference in the left) for (a) 1-km resolution and (b) 5-km resolution. Observation points of Sapporo and Eniwa-Shimamatsu, and the city center of Kita-Hiroshima, are marked by circles, and observation points of Ohmagari-Chuou and Wattu are marked by diamonds from north to southeast. (c) The map zooming out from the model domain is shown by the red box.

Eniwa-Shimamatsu operated by the JMA for the first case and the telemeter data at Ohmagari-Chuou observed by Hokkaido Regional Development Bureau and the meteorological observation at Wattsu by East Nippon Expressway Company Ltd. for the second case (Fig. 2.1). A further integration including 0000 UTC on 29 Feb 2016 was conducted to clarify the effect of snowfall and temperature to diagnose blowing snow potential. We diagnosed blowing snow potential based on SCALE outputs of 2-m temperature and specific humidity, 10-m wind vector, and precipitation intensity. We used the land use data in SCALE as roughness length data with about 1-km resolution and took an average of them for 5-km resolution (Figs. 2.1a, b)

Snow concentration measured blowing snow potential in this chapter Because blowing snow particles mostly follow the turbulent diffusion theory (Shiotani 1953; Nemoto and Nishimura 2004), the mass conservation law relates snow concentration n (g m^{-3}) to snowfall intensity P (g m^{-2} s^{-1}) and friction velocity u_* (m s^{-1}; Matsuzawa and Takeuchi 2002):

$$n = \frac{P}{w_f} + \left(n_1 - \frac{P}{w_f}\right)\left(\frac{z}{z_1}\right)^{-\frac{w_b}{ku_*}}. \quad (2.1)$$

Following Matsuzawa and Takeuchi (2002), the falling velocity of snowfall particles w_f and that of blowing snow particles w_b were assumed to be constant, 1.2 m s^{-1} and 0.35 m s^{-1}, respectively, n_1 is 30 g m^{-3}, z_1 is 0.15 m, and the von Karman's constant k was set to 0.4. Assuming the wind logarithmic distribution, the friction velocity could be estimated from 10-m wind speed U_{10} (m s^{-1}) as,

$$u_* = \frac{kU_{10}}{\ln(10/z_0)}, \quad (2.2)$$

where z_0 (m) was the roughness length. Snowfall intensity equals precipitation intensity when we identified precipitation as snowfall from a rain-snow discrimination relation (Matsuo and Sasyo 1981). Visibility V (m) could be estimated with an empirical relation (Matsuzawa and Takeuchi 2002),

$$\log(V) = -0.773\log(M_f) + 2.845, \quad (2.3)$$

where drift flux M_f (g m^{-2} s^{-1}) was given as

$$M_f = n_z U_z, \quad (2.4)$$

where n_z (g m^{-3}) and U_z (m s^{-1}) were snow concentration and wind speed at the height of z (m), respectively. Moreover, accumulated snow particles were assumed to be drifted when satisfying the conditions that a surface air temperature was below 0 °C and 10-m wind speed exceeds 5 m s^{-1} (*cf.* Takeuchi et al. 1986; Maeno 1982). When wind speed and surface air temperature did not

meet these thresholds, the second term of Eq. (2.1) was neglected. We estimated snow concentration and visibility at 1.2 m from the surface, a height at the general eye level of cars.

2.3. Results

2.3.1. An added value of the DDS

We diagnosed blowing snow potential for a case of 6 Jan 2018. The snow concentration estimated with the DDS became large along the northern coast and around Eniwa city in 0700-

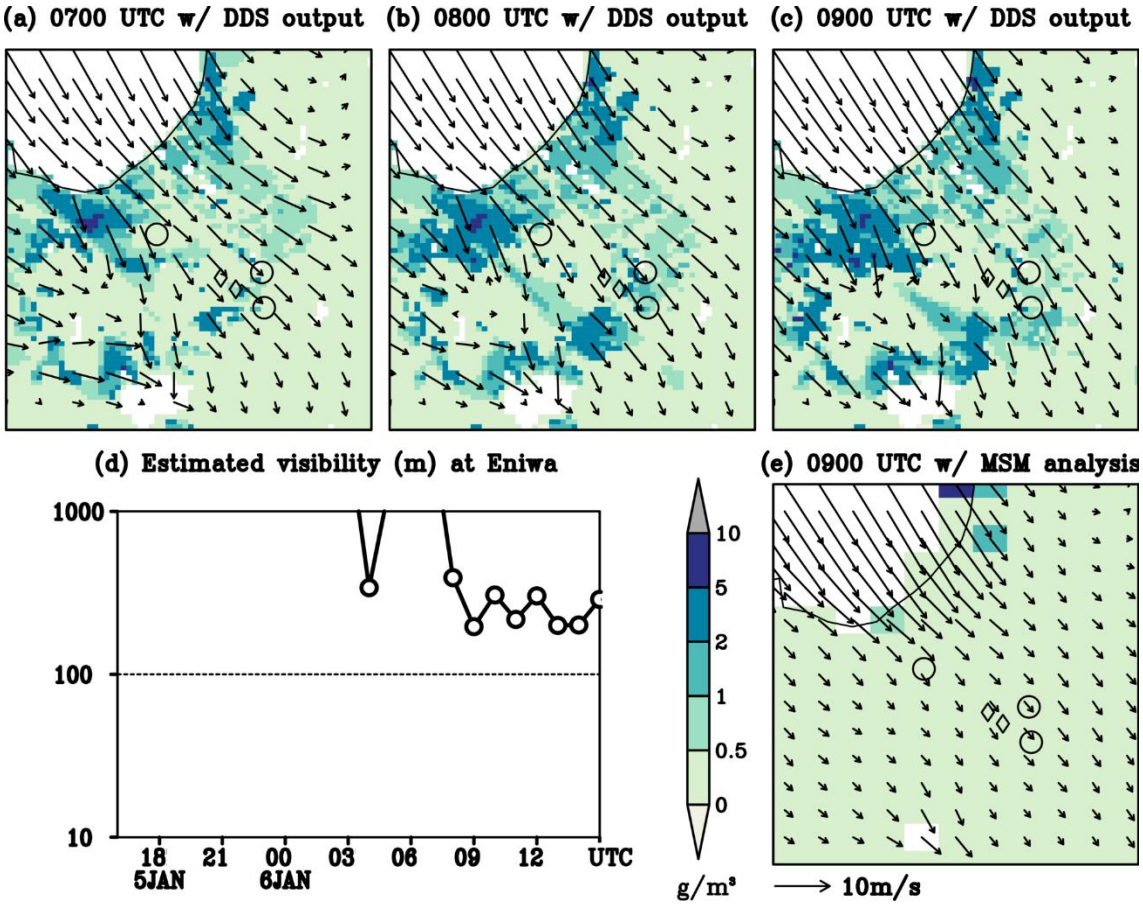

Fig. 2.2. (a-c) Snow concentration based on DDS data at (a) 0700 UTC, (b) 0800 UTC, (c) 0900 UTC on 6 Jan 2018. (d) Time-series of visibility at 141.56°N, 42.87°E in Eniwa city empirically estimated DDS data from 1500 UTC on 5 Jan to 1500 UTC on 6 Jan 2018. (e) Same as (c), but for the meso-scale model analysis. The circle marks denote Sapporo, Kita-Hiroshima, and Eniwa-Shimamatsu, and the diamond marks denote Ohmagari-Chuou and Wattsu.

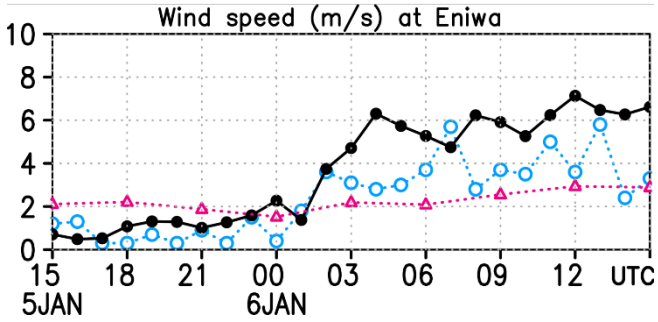

Fig. 2.3. Time-series of surface wind speed at 141.57°E, 42.93°N at Eniwa-Shimamatsu AMeDAS station from 1500 UTC 5 Jan 2018 to 1500 UTC on 6 Jan. A black line with filled circles indicates the results of DDS at the nearest gridpoint, a pink line with triangles indicates MSM analysis, a blue line with open circles indicates AMeDAS observation.

0900 UTC (Figs. 2a-c). The snow concentration increased up to 1.3 g m^{-3} at the nearest gird point to Eniwa Expressway Interchange in Eniwa city in three hours. The visibility became low to ca. 200 m at 0900 UTC (Fig. 2.2d), corresponding to a close of the Hokkaido Expressway. In contrast, related to weaker wind over the land, the snow concentration estimated with MSM analysis was uniformly low less than 0.5 g m^{-3} (Fig. 2.2e). The visibility estimated based on MSM analysis always surpassed 1000 m near the Interchange (not shown). According to the AMeDAS observation at Eniwa-Shimamatsu, the DDS reproduced a gradual increase with a slight overestimation in wind speed after 0300 UTC on the date, whereas the MSM analysis provided a rather constant wind speed throughout the date (Fig. 2.3). The DDS had an add-value in the blowing snow estimate for this case, despite a slight difference in precipitation between DDS and observation (not shown).

Another case of 24 Feb 2016 is displayed in Fig. 2.4. The snow concentration distribution estimated based on the DDS result in 0100-0300 UTC is shown in Figs. 2.4a-c. This result showed a large snow-concentration area rapidly expanding from west to east in two hours. The snow concentration increased from up to 1.9 g m^{-3} at the nearest gird point to the traffic accident in Kita-Hiroshima city at 0245 UTC. The visibility empirically estimated suddenly

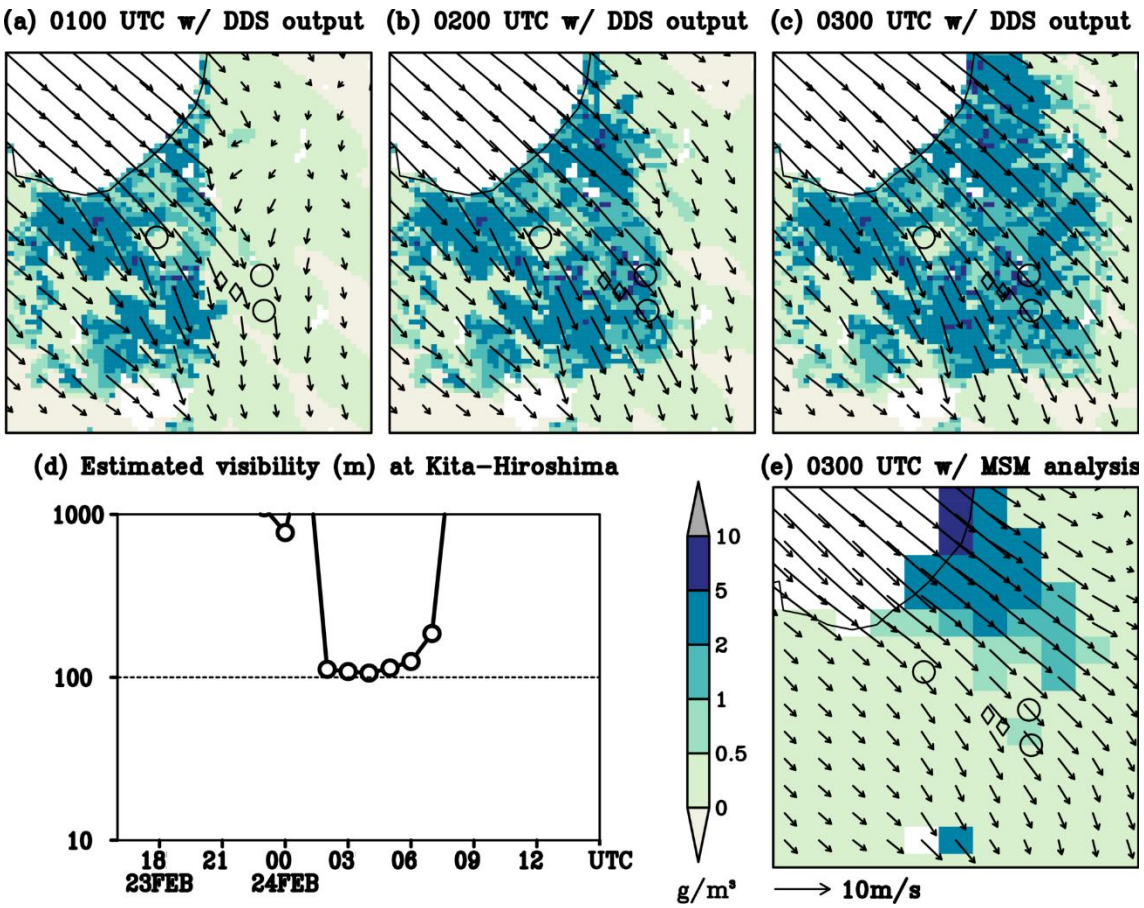

Fig. 2.4. (a-c) Snow concentration based on the dynamical downscaled (DDS) data shown by shading as per the reference between (d) and (e), superimposed with the 10-m wind vector scaled as the 10 m s^{-1} reference in the bottom right, at (a) 0100 UTC, (b) 0200 UTC, (c) 0300 UTC on 24 Feb 2016. (d) Time-series of visibility at 141.48°E, 42.97°N in Kita-Hiroshima city empirically estimated DDS data from 1500 UTC 23 Feb to 1500 UTC 24 Feb. (e) Same as (c), but for the meso-scale model analysis.

became low to 100 m from 0100 UTC to 0200 UTC consistent with a possible cause for the accident (Fig. 2.4d). Compared with the DDS, the MSM analysis showed weaker wind speed uniformly over the land (Fig. 2.4e). This reduced the snow concentration except for the area along the northern coastline normal to the north-westerly. Related to this, visibility estimated based on MSM analysis kept exceeding 1000 m in the accident point throughout the day (not shown). However, according to the operational wind observation at Ohmagari-Chuou (Fig. 2.5a) and Wattsu (Fig. 2.5b), both near the target point, the DDS moderately over-estimated wind speed

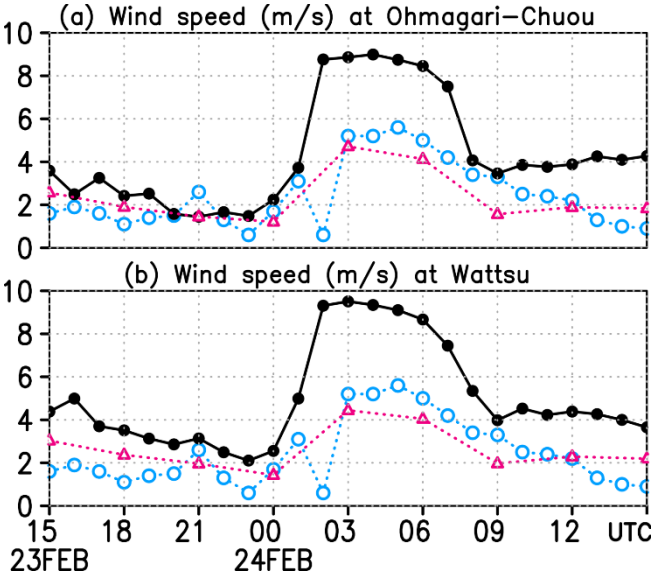

Fig. 2.5. Time-series of surface wind speed (a) at Ohmagari-Chuou, 141.47°E, 42.98°N and (b) at Wattsu, 141.50° E, 42.96°N, from 1500 UTC 23 Feb 2016 to 1500 UTC 24 Feb. It is remarked that the model outputs are at 10 m above the ground level (AGL) while the anemometer is installed at 15 m AGL at Ohmagari-Chuou and at 5 m AGL at Wattsu. A black line with filled circles indicates the results of DDS at the nearest gridpoint, a pink line with triangles indicates MSM analysis, a blue line with open circles indicates AMeDAS observation.

there whereas it reproduced the frozen temperature and no snowfall at the time (not shown). The blowing snow estimated here by the DDS was hence exaggerated due to the wind speed bias in the meaning of the spatial and temporal average.

2.3.2. Effects of snowfall and surface air temperature

A sensitivity test was conducted for the case at 0000 UTC on 29 Feb 2016 (Fig. 2.6). In this case, strong southeasterly encouraged drifting snow by resuspending accumulated snow, whereas relatively high temperatures partially suppressed the resuspension. Moreover, snow fell in most regions with a maximum intensity of 2.5 mm h^{-1}, at Kita-Hiroshima city, which affected an increase in the snow concentration. The snow concentration in the reference estimation with the full conditions (Fig. 2.6a) showed a noticeable blowing snow area over mountains in the southwest of Sapporo city center. The snow concentration ranged from 0 to 1 g m^{-3} in the urban area of Sapporo and no blowing occurred in the southeast area.

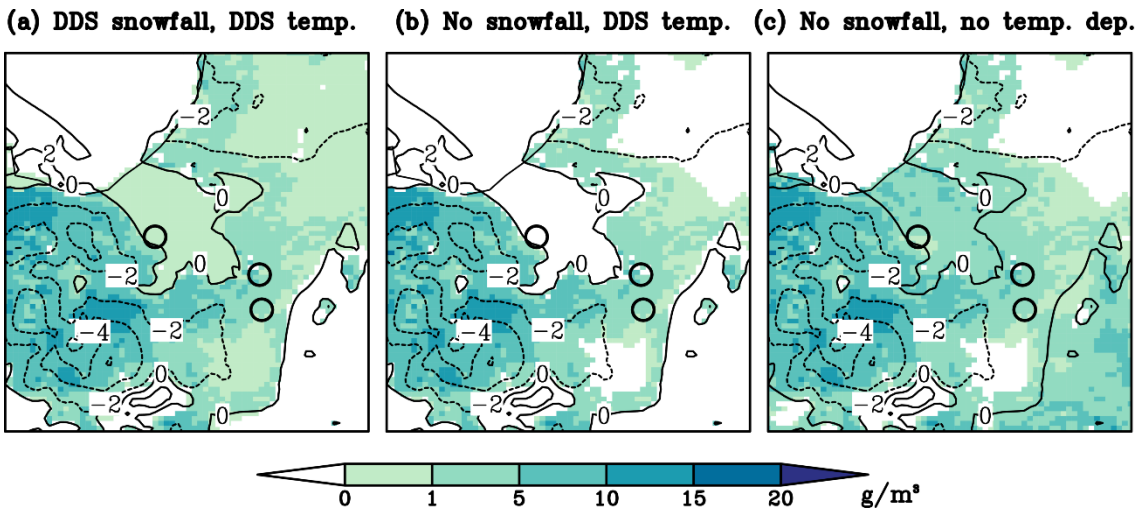

Fig. 2.6. (a) Snow concentration estimated based on the DDS data with the full conditions on temperature and wind shown by shading, superimposed contours describing 2-m temperature (°C), at 0000 UTC on 29 Feb 2016. (b) Snow concentration estimated without the snowfall effect in Eq. (2.1). (c) Snow concentration estimated without the snowfall effect in Eq. (2.1) and further without the temperature dependencies.

Without the snowfall effect from Eq. (2.1), the snow concentration reduced to zero in the area where surface air temperatures exceeded 0 °C, including the urban area of Sapporo, because accumulated snow particles could not lift from the melting surface even in strong wind environment (Fig. 2.6b). The difference from the full estimates suggested that a large snow concentration in mountains was attributed to resuspending surface snow particles by wind and less snow concentration in the urban area was attributed to blowing snowfall particles. Switching off the temperature condition, furthermore, snow concentration exceeded 1 g m^{-3} in most areas (Fig. 2.6c). This estimation showed the blowing snow potential solely considering resuspension by the strong surface wind. The difference between Figs. 2.6b, c thus means the suppression of resuspension under a warm environment.

2.4. Concluding Remarks

We have estimated snow concentration and visibility based on the dynamically

downscaled data with 1-km resolution. The results for two typical blowing-snow cases in Hokkaido, Japan, suggested that high snow concentration and low visibility are estimated in the site where blowing snow was recorded. The sudden development of blowing snow could also be diagnosed in the DDS-based estimation. The blowing snow potential analysis with the meso-scale model analysis with 5 km resolution, in contrast, did not reproduce the blowing snow development. In an indirect validation of our results based on the wind observation, the DDS certainly improved the surface wind speed and then the blowing-snow estimate for a case at Eniwa in Feb 2018. In contrast, for another case at Kita-Hiroshima in Feb 2016, even though the blowing-snow estimate in the DDS was consistent with the record of the traffic accident, the DDS overestimated wind speed in a comparison with observations, indicative of a DDS limitation in the blowing-snow evaluation. We found a slight difference in temperature and precipitation between DDS and observation, but these were not much related to the blowing-snow evaluation. The primary importance of surface wind speed in the blowing-snow estimate was also emphasized in the sensitivity test, which provided a consistent result with Matsuzawa et al. (2014).

The blowing snow potential analysis that we have performed can be possibly applied to the forecast. Toward a practical forecast of blowing snow potential, we now provide two caveats. As has been demonstrated in the case study, the blowing snow is mainly caused by strong surface wind. Higher-resolution simulation likely improves the horizontal distribution and temporal evolution of surface wind vectors because of the fine topography prescribed as the model boundary. However, as shown in the second case, whichever model one used, a systematic model bias must deteriorate the surface wind estimate and forecast. The problem could be relieved if one made a state-of-the-art bias correction before the evaluation of blowing snow potential. The use of ensemble forecasts might realize the probabilistic representation of blowing snow potential. These are expectedly possible add-values of high-resolution simulation and forecast for blowing

snow potential. On the other hand, if the DDS surface wind estimate were perfect as an hourly mean and a 1-km gridcell average, it would be quite different a sudden, spot wind captured in the observation. Hence, a practical estimate of blowing snow, not its potential, requires an estimate of possible maximum wind speed within a single gridcell of the high-resolution simulation, through highly-dense observation and realistic turbulent simulation. This problem is actually beyond the scope of the chapter and should be investigated elsewhere.

Moreover, as we have shown in the sensitivity test, high temperature strongly suppresses blowing snow. The temperature condition in this chapter roughly treated the snow surface status. Even over the frozen point, if the surface is covered with fresh-snow, snow particles are likely resuspended. Snow property at the surface is affected by various processes such as fresh-snow supply, melting in a high temperature, and metamorphosis for temperature gradient and compression. Hence, we require the snowpack simulation to know the snow surface character for an accurate forecast of blowing snow potential.

Chapter 3. Development of a Snowdrift Model with the Lattice Boltzmann Method

3.1. Introduction

Snowdrifts are patchy accumulations of snow resulting mainly from the redistribution of snow particles on the ground by drifting snow, which is the horizontal movement of snow particles by creep and saltation on the surface. Snowdrifts can severely affect human activities; for example, snowdrifts in mountainous terrain can trigger avalanches and affect the mass balance of water (Lehning et al. 2006; Lehning et al. 2008; Mott et al. 2010; Vionnet et al. 2017). Moreover, snowdrifts cause traffic disruption because vehicles tend to stack and stagnate on roads with a snow depth of 15 cm (Kaneko et al. 2011). Snow fences are one of the solutions to mitigate the problems caused by snowdrifts, especially on roads in snowy, windy locations. Snowdrift distribution around snow fences depends strongly on their design parameters, such as height, thickness, bottom gap, space between panels, penetration rate of porous fences, and distance from the road (Tabler 1986; Uematsu et al. 1991; Alhajraf 2004). Some studies have examined the onset of drifting snow and snow accumulation in wind tunnel experiments (Delpech et al. 1998; Okaze et al. 2012; Zhou et al. 2014). Other studies have reported the effect of snow fence design on the size of snowdrifts on roads based on field observations (Tabler 1980; Takeuchi 1980; Takeuchi et al. 1986; Tabler 1994). However, field observations provide limited opportunities to sample drifting snow events at a certain site, and wind tunnel experiments do not always correspond to real situations owing to scaling effects. Moreover, it is generally costly to obtain sufficient data to design snow fences using these methods. However, the advancement of computer technology has enabled numerical simulations of snowdrift development to be performed to search for an optimal snow-fence design at a target site.

Numerical simulations of drifting snow require computational fluid dynamics (CFD) and the estimation of snowdrift distribution. Numerical simulations of drifting snow were pioneered in the 1990s by Uematsu et al. (1991) and Liston et al. (1993). These studies used a wind simulation based on the Reynolds-averaged Navier–Stokes equations model with turbulence parameterizations, such as K-theory and the k-ε model. These models reproduced the snowdrift distribution around a simple snow fence. Some studies extended these models to include drifting snow processes due to multiple snow events that were more complicated (Beyers et al. 2004; Tominaga et al. 2011a, 2011b). The large-eddy simulation (LES) has been applied to snow transport simulations to describe turbulence more accurately (Okaze et al. 2018; Wang and Jia 2018). For example, Zwaaftink et al. (2014) combined the LES and a Lagrangian stochastic model and described the temporal and spatial variability of drifting snow with their model. Some studies have considered the momentum exchange between particles and background wind (Elghobashi 1994). Moreover, turbulent wind is strongly affected not only by the fixed boundaries, including topography and artificial obstacles, but also by snow surfaces that vary temporally due to snowdrifts.

The lattice Boltzmann method (LBM) is a CFD algorithm for quick calculations [see McNamara and Zanetti (1988) for an introduction and Benzi et al. (1992), Qian et al. (1995), and Chen and Doolen (1998) for comprehensive reviews]. In the LBM, the Navier–Stokes equations are replaced with a distribution function equation called the lattice Boltzmann equation that treats the fluid flow as microscopic fictitious particles in the space lattice (Chen et al. 1992; Qian et al. 1992). The lattice Boltzmann equation can be numerically solved by the translation of the distribution function and the relaxation to the equilibrium state. The LBM algorithm is characterized by simpler implementation and higher efficiency in parallel computation than the conventional CFD algorithm (Chen and Doolen 1998). Han et al. (2019) demonstrated that the

LBM was three-fold faster than the finite volume method in 16-core parallel processing. The LBM has been applied to various fields, such as wind flow in the urban environment with 1 m resolution (Onodera et al. 2013), canopy turbulence in neutrally stratified conditions (Watanabe et al. 2020), flow in porous media (Liu et al. 2016), and flow in blood vessels (Zhang et al. 2008; Bernasch et al. 2009). In cryology, Wang et al. (2006) simulated dynamic snowing scenes for various weather conditions and snow crystal types with LBM. Lu et al. (2009) also used the LBM to reproduce dendric snow crystal growth in clouds. These studies suggest that the LBM is appropriate for modeling blowing snow and snowdrift distribution; however, no such studies have been performed.

In this chapter, we develop an LBM model for snowdrift distribution around an artificial snow fence. The model consists of the CFD module based on the LBM and a module for calculating the snow particles' motion and accumulation following Nishimura and Hunt (2000). The present work focuses on checking the feasibility of applying the LBM to blowing snow and snowdrift modeling in typical experiments. Because the computational efficiency of the LBM has been demonstrated (King et al. 2017; Han et al. 2019), we did not compare the LBM with other CFD modeling methods. The remaining part of this chapter is organized as follows: in Sections 3.2 and 3.3, we describe the model and experiments in detail; in Section 3.4, we show the results of the model simulation, compare them with previous observation and numerical simulation studies, and discuss the effect of snow fences on snowdrift distribution; and in Section 3.5 we conclude the chapter.

3.2. Model

3.2.1. CFD module

The CFD module in the model we developed was based on a three-dimensional LBM

model that delivered microscopic fictitious particles to 19 neighbor nodes, usually referred to as a D3Q19 configuration with the single-relaxation time collision operator (Fig. 3.1). This LBM configuration has been established in a sufficiently accurate turbulent simulation (Onodera et al. 2013; King et al. 2017; Deiterding and Wood 2016; Noh 2019), although other sophisticated methods have been proposed to reduce the error (Geier et al. 2009; Geier et al. 2015; Suga et al. 2015). The discretized lattice Boltzmann equation is a prognostic equation of the distribution function for particles in the i-th direction, f_i,

$$f_i(\boldsymbol{r} + \boldsymbol{c}_i\Delta t, t + \Delta t) = f_i(\boldsymbol{r}, t) + \Omega_{\mathrm{i}}\,\Delta t, \tag{3.1}$$

where $\boldsymbol{r}$ is the particle position vector, Δt is the time increment, Ω_i is the collision term, and $\boldsymbol{c}_i$ is the particle velocity vector.

The Bhatnagar-Gross-Krook approximation reduced collision term Ω_{i} to the relaxation to the equilibrium state of the distribution function (Chen et al. 1992; Qian et al. 1992),

$$\Omega_{\mathrm{i}} = -\frac{1}{\tau}\left(f_i - \widehat{f_i}\right). \tag{3.2}$$

Here, τ is the relaxation time as a function of viscosity ν_*,

$$\tau = \frac{1}{2} + \frac{3\nu_*}{c^2\Delta t} \tag{3.3}$$

where c is the discrete speed, defined as $\frac{\Delta x}{\Delta t}$, with spatial increment Δx. ν_* is defined as $\nu_* = \nu_{0n} + \nu_t$, where ν_{0n} is the non-dimensional viscosity of the air (4.0×10^{-6}) and ν_t is the eddy viscosity, given in Eq. (3.7). $\widehat{f_i}$ is the equilibrium distribution function for particles in the i-th direction, calculated in the D3Q19 configuration as

$$\widehat{f_i} = w_i\rho\left[1 + \frac{(\boldsymbol{c_i}\cdot\boldsymbol{u})}{c_s^2} + \frac{(\boldsymbol{c_i}\cdot\boldsymbol{u})^2}{2c_s^4} - \frac{|\boldsymbol{u}|^2}{2c_s^2}\right], \tag{3.4}$$

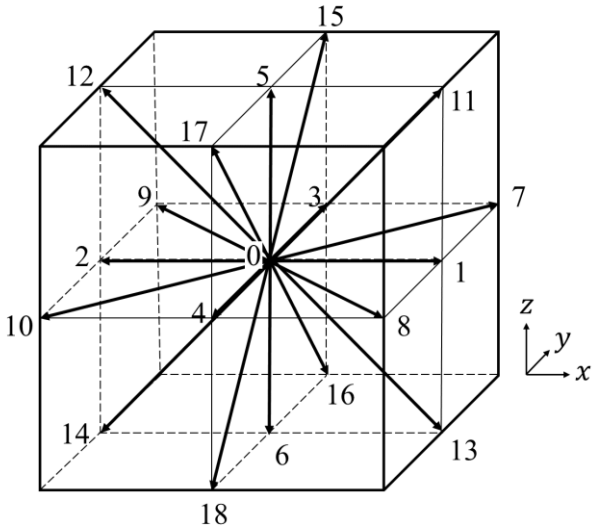

Fig. 3.1. Schematic of the particle velocity vector, $\boldsymbol{c_i}$, in the D3Q19 configuration of the lattice Boltzmann model.

where

$$w_i = \begin{cases} \frac{1}{3} & (i = 0) \\ \frac{1}{18} & (i = 1, 2, \dots, 6), \\ \frac{1}{36} & (i = 7, 8, \dots, 18) \end{cases} \tag{3.5}$$

the lattice speed of sound $c_s = 1/\sqrt{3}$, and ρ and $\boldsymbol{u}$ are the macroscopic density and velocity, respectively, calculated in the D3Q19 configuration as

$$\rho = \sum_{i=0}^{18} f_i, \quad \text{and} \quad \boldsymbol{u} = \frac{1}{\rho}\sum_{i=0}^{18} f_i \boldsymbol{c}_i. \tag{3.6}$$

The dimensional variables are transferred from the non-dimensional distribution function by multiplying the non-dimensional value by 50.0 to give the same Reynold numbers.

The sub-grid scale parameterization (Feng et al. 2007; Onodera et al. 2013; Wang et al. 2014; Suga et al. 2015) was implemented to estimate the eddy kinematic viscosity, ν_t. We used the Smagorinsky model (Smagorinsky 1963), in which ν_t is related to velocity gradient tensor $\mathbf{S}$ by

$$\nu_t = C\Delta^2|\bar{\mathbf{S}}|, \tag{3.7}$$

where Smagorinsky coefficient $C = 0.12$ (Tominaga et al. 2008; Okaze et al. 2021) and $C = 60$ in the damping zone, which consists of 15 grids from the outlet boundary to damp the numerical oscillation near the outlet (Inagaki et al. 2017). Δ is the cubic root of the local mesh volume. $|\bar{\mathbf{S}}|$ was estimated in the D3Q19 configuration as

$$|\bar{\mathbf{S}}| = \frac{3}{2\rho\tau}\sqrt{2\sum_{k=1}^{3}\sum_{j=1}^{3}\sum_{i=0}^{18}(f_i - \hat{f}_i)c_{ij}c_{ik}}, \tag{3.8}$$

where c_{ij} and c_{ik} are the j-th and k-th components of $\boldsymbol{c_i}$, respectively.

The model domain was a finite channel in the three-dimensional space spanned by the wind direction, x, the horizontal direction normal to x (or fence direction), y, and the vertical direction, z. Hereafter, for convenience, the negative and positive ends of x in the domain are called the western and eastern boundaries, those of y are called the southern and northern boundaries, and those of z are called the bottom and top boundaries, respectively. The horizontal direction is rotationally invariant in this system.

The LBM represents the western boundary condition with inflow $u_0(x,y,z) = (u_0(y,z), v_0(y,z), w_0(y,z))$ (Section 3.2.2) as

$$\begin{aligned}
f_1 &= f_2 + \frac{\rho u_0}{3}, \\
f_7 &= f_{10} + \frac{f_4 + f_{17} + f_{18} - f_3 - f_{15} - f_{16}}{2} + \frac{\rho(u_0 + v_0)}{6} + \frac{\rho v_0}{3}, \\
f_8 &= f_9 + \frac{f_3 + f_{15} + f_{16} - f_4 - f_{17} - f_{18}}{2} + \frac{\rho(u_0 - v_0)}{6} - \frac{\rho v_0}{3}, \\
f_{11} &= f_{14} + \frac{f_6 + f_{16} + f_{18} - f_5 - f_{15} - f_{17}}{2} + \frac{\rho(u_0 + w_0)}{6} + \frac{\rho w_0}{3},
\end{aligned} \tag{3.9}$$

and

$$f_{13} = f_{12} + \frac{f_5 + f_{15} + f_{17} - f_6 - f_{16} - f_{18}}{2} + \frac{\rho(u_0 - w_0)}{6} - \frac{\rho w_0}{3}.$$

On the other side, the LBM represents the free-flow condition at the eastern boundary (Hecht and Harting 2010) as

$$\begin{aligned} f_2 &= f_1 - \frac{u_e}{3}, \\ f_{10} &= f_7 - \frac{f_4 + f_{17} + f_{18} - f_3 - f_{15} - f_{16}}{4} - \frac{u_e}{6}, \\ f_9 &= f_8 - \frac{f_3 + f_{15} + f_{16} - f_4 - f_{17} - f_{18}}{4} - \frac{u_e}{6}, \\ f_{14} &= f_{11} - \frac{f_6 + f_{16} + f_{18} - f_5 - f_{15} - f_{17}}{4} - \frac{u_e}{6}, \text{and} \\ f_{12} &= f_{13} - \frac{f_5 + f_{15} + f_{17} - f_6 - f_{16} - f_{18}}{2} - \frac{u_e}{6}, \end{aligned} \tag{3.10}$$

where

$$\begin{aligned} u_e = -1 + f_0 + f_3 + f_4 + f_5 + f_6 + f_{15} + f_{16} + f_{17} + f_{18} \\ + 2(f_1 + f_7 + f_8 + f_{11} + f_{13}). \end{aligned} \tag{3.11}$$

The southern and northern boundaries are periodic. Distribution functions f_3, f_7, f_9, f_{15}, and f_{16} at the southern boundary are equal to those at the northern boundary; and distribution functions f_4, f_8, f_{10}, f_{17}, and f_{18} at the northern boundary are equal to those at the southern boundary. The top boundary was a free-slip boundary (*i.e.,* $\frac{d\boldsymbol{u}}{dz} = 0$). The LBM representation was

$$f_6 = f_5, f_{13} = f_{11}, f_{14} = f_{12}, f_{16} = f_{15}, \text{and } f_{18} = f_{17}. \tag{3.12}$$

The bottom boundary was no-slip (*i.e.*, $\boldsymbol{u} = 0$), so that the LBM represented it as bounce-back,

$$f_5 = f_6, f_{11} = f_{14}, f_{12} = f_{13}, f_{15} = f_{18}, \text{and } f_{17} = f_{16}. \quad (3.13)$$

The boundary on the fence was also no-slip as bounce-back and was written similarly to Eq. (3.13).

3.2.2. Inflow turbulence generation

We generated the artificial inflow turbulence and imposed it as the inflow on the western boundary. The inflow turbulence was generated as two-dimensional digital-filtered random data by controlling the time and spatial autocorrelations of the resultant inflow turbulence (Okaze and Mochida 2017; Xie and Castro 2008). The total inflow, $\boldsymbol{u_0}(y,z,t)$, from the western boundary was divided into the time average, $\langle \boldsymbol{u_0} \rangle$, and the deviation from the time average, $\boldsymbol{u_0'}$. We assumed that the model domain was the constant flux layer. The wind direction of the time-averaged vector was only eastward, and the wind speed followed the logarithmic profile of

$$\langle u_0(z) \rangle = \frac{u_*}{\kappa} \ln\left(\frac{z}{z_0}\right), \quad (3.14)$$

where u_* is the friction velocity (a parameter to be given), z_0 is the roughness length for flat snow surface (0.1 mm; Nishio and Ishida 1973), and κ is von Karman's constant (0.4). Using other common assumptions (Okaze and Mochida 2018), Reynolds stress tensor $\mathbf{R}$ for the inflow turbulence was parameterized as

$$\mathbf{R} = \begin{pmatrix} \langle u_0'u_0' \rangle & \langle u_0'v_0' \rangle & \langle u_0'w_0' \rangle \\ \langle v_0'u_0' \rangle & \langle v_0'v_0' \rangle & \langle v_0'w_0' \rangle \\ \langle w_0'u_0' \rangle & \langle w_0'v_0' \rangle & \langle w_0'w_0' \rangle \end{pmatrix} = u_*^2 \begin{pmatrix} 10/3 & 0 & -1 \\ 0 & 5/3 & 0 \\ -1 & 0 & 5/3 \end{pmatrix}. \quad (3.15)$$

The deviation from the time average was computed as $\boldsymbol{u_0'}(y,z,t) = \widetilde{\mathbf{R}}\,\boldsymbol{\Psi}(y,z,t)$, where $\widetilde{\mathbf{R}}$ is the Cholesky decomposition of $\mathbf{R}$ and $\boldsymbol{\Psi}$ is the numerical solution of the stochastic equation (Xie and Castro 2008) of

$$\boldsymbol{\Psi}(y,z,t+\Delta t) = \boldsymbol{\Psi}(y,z,t)\exp\left(-\frac{\Delta t}{T}\right) + \boldsymbol{\psi}(y,z,t+\Delta t)\left\{1-\exp\left(-\frac{2\Delta t}{T}\right)\right\}^{1/2}, \tag{3.16}$$

from the initial condition of $\boldsymbol{\Psi}(y,z,0) = \boldsymbol{\psi}(y,z,0)$. Here, T is the characteristic timescale and $\boldsymbol{\psi}$ is the digital-filtered normal random numbers that satisfy a spatial autocorrelation with characteristic length L (Klein et al. 2003). $\boldsymbol{\psi}(y,z,t)$ was generated at each time step with a different random number. Following the modified Prandtl theory (Okuma et al. 1996), L was parameterized as

$$L = \frac{1}{3}\kappa z. \tag{3.17}$$

Then, by assuming Taylor's hypothesis of frozen turbulence, characteristic timescale T was parameterized as

$$T = \frac{1}{3}\kappa z\langle u_0(z)\rangle. \tag{3.18}$$

The inflow was numerically generated with the same grid spacing and the same time interval as the CFD module.

3.2.3. Snow particle module

The snow particle module in the model followed Nishimura and Hunt (2000) and Nemoto and Nishimura (2004). Assuming that drifting snow particles were spherical, made of ice, electrically neutral, and not driven by the lift force, the equation of motion for the particles is written as

$$\frac{d\boldsymbol{u_p}}{dt} = -\frac{3}{4}\left(\frac{\rho_a}{\rho_p d}\right)C_d V_R\left(\boldsymbol{u_p}-\boldsymbol{u}\right) - g\boldsymbol{k}, \tag{3.19}$$

where $\boldsymbol{u_p}$ (m s^{-1}) is the particle velocity vector, $\boldsymbol{u}$ (m s^{-1}) is the wind vector, $V_R = |\boldsymbol{u_p} - \boldsymbol{u}|$, g is gravity (9.8 m s^{-2}), ρ_a and ρ_p are the densities of air (1.34 kg m^{-3}) and the particle (910 kg m^{-3}), respectively, and d is the particle diameter (100 μm; Nishimura et al. 2014). C_d is the drag coefficient for the particle (White 1974), calculated as

$$C_d = \frac{24\nu_0}{V_R d} + \frac{6}{1 + V_R d/\nu_0} + 0.4, \tag{3.20}$$

where ν_0 is the viscosity of the air (10^{-5} m^2 s^{-1}). The terminal fall velocity of a snow particle was estimated from the vertical component of Eq. (3.19) and Eq. (3.20) as 0.30 m s^{-1}.

Observation results indicated that accumulated snow particles jumped out of the snow surface when the friction velocity was high enough to lift them (Shao and Li 1999; Nemoto and Nishimura 2004). Based on this result, we assumed that a snow particle fell on the bottommost level and occupied the first grid-cell when the friction velocity on the snow surface was below the threshold. The friction velocity, u_* (m s^{-1}), on the snow surface was estimated with a wall function by a two-layer model in Werner and Wengle (1991) as

$$u_* = \begin{cases} \sqrt{\dfrac{2\nu_0 |\boldsymbol{u}(z_b)|}{z_b}} & \text{for } |\boldsymbol{u}(z_b)| \le \dfrac{\nu_0}{2z_b} A^{\frac{2}{1-B}} \\ \left\{ \dfrac{1-B}{2} A^{\frac{1+B}{1-B}} \left(\dfrac{\nu_0}{z_b}\right)^{1+B} + \dfrac{1+B}{A} \left(\dfrac{\nu_0}{z_b}\right)^{B} |\boldsymbol{u}(z_b)| \right\}^{\frac{1}{1+B}} & \text{for } |\boldsymbol{u}(z_b)| \ge \dfrac{\nu_0}{2z_b} A^{\frac{2}{1-B}} \end{cases}, \tag{3.21}$$

where z_b is the height of the bottommost grid just above the snow surface, $A = 8.3$, and $B = 1/7$. This is a different definition of the friction velocity from the inflow generation. The wind velocity at the first grid point varied in time, and then the wall unit in the first grid point was also changed. This approach automatically considered the linear and power law distributions with an instantaneous wall unit calculated with the wind speed in the first grid point. The threshold of the friction velocity, u_{*t} was computed following Bagnold (1941) and Clifton et al. (2006) as

$$u_{*t} = 0.2\sqrt{\frac{\rho_p - \rho_a}{\rho_a} gd} \sim 0.163 \text{ m s}^{-1}. \quad (3.22)$$

We assumed that no snow particles accumulated when the friction velocity was larger than this threshold. The aerodynamic entrainment, rebound, splash, mass loss by sublimation and disruption, the drag force on the fluid, and coalescence of snow particles by the collision were all neglected.

3.3. Experiments

We performed three experiments: with no fence, with a two-dimensional fence, and with a three-dimensional fence of 1.5 m in width (Fig. 3.2). The fence was set 4 m from the western boundary and was centered in the channel. The fence was non-porous, solid, and the thickness was 0.1 m and the height was 1 m. The following model settings were independent of the presence of the fence. The channel size was 15.75 × 5 × 5 m, with the grid spacing at 0.05 m. The origin of the x-coordinate was 4 m from the western boundary, at the position of the fence. In the CFD calculation, the integration time was 30 s and the time interval was 1 ms; the results were sampled every 0.02 s from the initial time. In the generation of the inflow turbulence, the 40 s data was stored with an interval of 4 ms. The inflow turbulence was generated with the friction velocity, such that the time-averaged wind speed was 6 m s^{-1} westerly at 10 m aloft in the log profile and the initial wind profile over the calculation domain was imposed as the same value. We used 30 s data for the generated inflow turbulence after the spin-up as the western boundary condition after linear interpolation as every 1 ms.

We numerically integrated the equation of motion of snow particles [Eq. (3.19)] with a time interval of 1 ms. The particles were uniformly distributed on the western boundary plane per

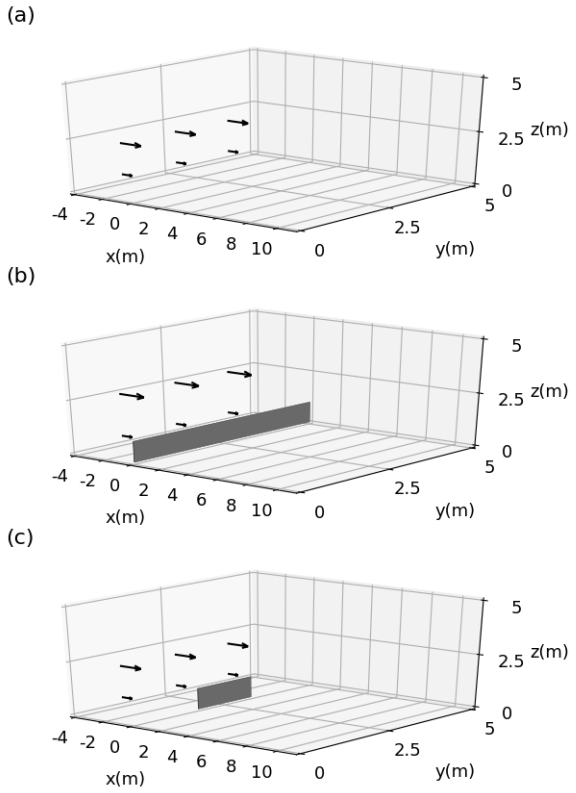

Fig. 3.2. Schematic of the calculation domain and initial wind vectors in the experiment with (a) no fence, (b) a two-dimensional fence, and (c) a three-dimensional fence.

5.0 cm horizontally and per 2.5 cm vertically at the initial time, but we assumed that a single particle in the snow module represented snow mass corresponding to snow volume flux depending on the height (Fig. 3.3b) as

$$v_f(z) = \alpha \frac{n(z)\langle u_0(z)\rangle}{\rho_p}. \tag{3.23}$$

Here, $\alpha = 1500$ to accelerate the snow accumulation, and snow concentration $n(z)$ (g m^{-3}) is given (Fig. 3.3a; Shiotani 1953; Matsuzawa and Takeuchi 2002) by

$$n(z) = \min\left(30, 30\left(\frac{z}{0.15}\right)^{-\frac{0.30}{\kappa u_*}}\right), \tag{3.24}$$

where the friction velocity u_* was estimated by Eq. (3.14). The snow particles' motion was

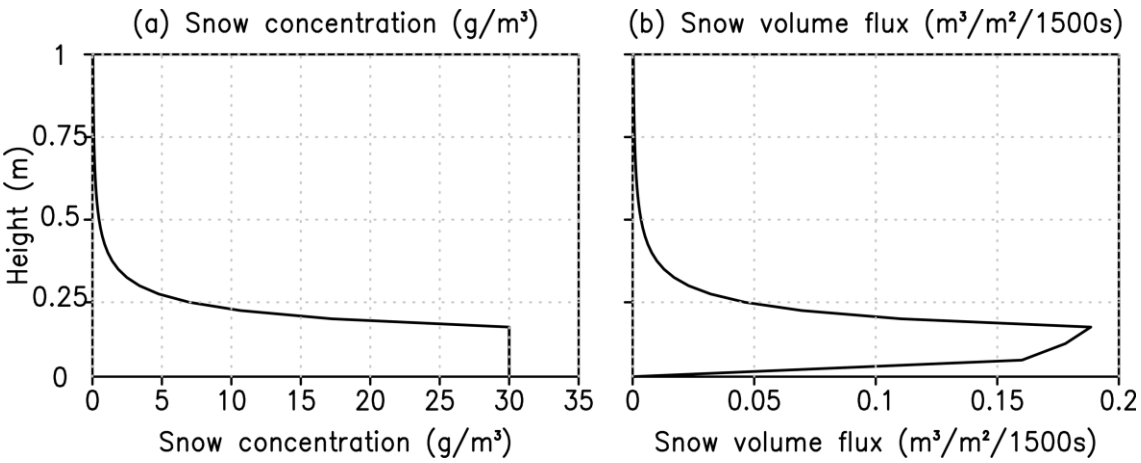

Fig. 3.3. Vertical profiles of (a) snow concentration and (b) snow volume flux of the initial condition on the western boundary plane of the snow particle module.

driven by the sampled time segments of wind data obtained from each experiment with or without a fence; several snow particle integrations were conducted with the CFD output starting from a different time. The initial wind profile based on the CFD module was given to the snow module every 0.1 s and the wind profile in the snow module was renewed every 0.02 s. The integration ended when all snow particles had fallen or flowed out of the calculation domain. Accumulated snow particles gave a height on the grid corresponding to the snow volume per grid area. Snow particles within the snowdrift did not move, collapse, melt, or sublimate. The estimated snowdrift was spatially smoothed by averaging data with their neighbors.

3.4. Results

3.4.1. Artificial inflow turbulence

First, we checked whether the inflow turbulence followed the target wind profile [Eq. (3.14)] and its corresponding Reynolds stress tensor [Eq. (3.15)]. The time-averaged inflow turbulence had a vertical profile quite similar to the target log profile with 6 m s^{-1} westerly at 10 m height (not shown). The Reynolds stresses also agreed with the prescribed values of $\langle u'u' \rangle \sim 10/3\, u_*^2$, $\langle v'v' \rangle \sim \langle w'w' \rangle \sim 5/3\, u_*^2$, $\langle u'w' \rangle \sim -u_*^2$, and $\langle v'u' \rangle \sim \langle v'w' \rangle \sim 0$ (Fig.

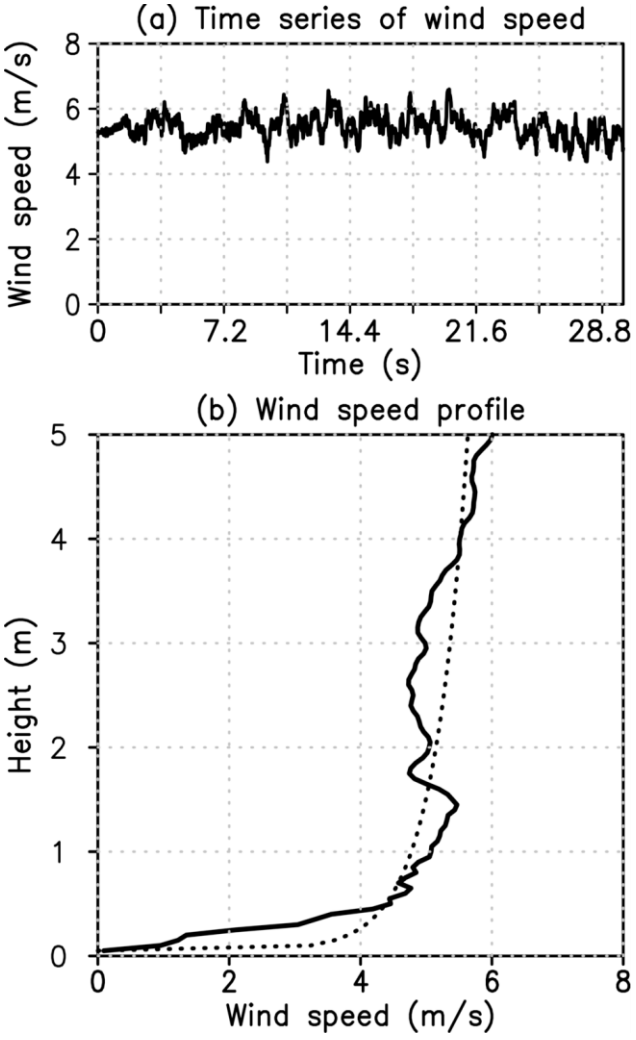

Fig. 3.4. (a) Time series of wind speed for the no-fence experiment at the center of the calculation domain from 0 to 30 s. (b) Vertical wind speed profile for the no fence experiment at $(x, y, t) = (3.5\ \mathrm{m}, 2.5\ \mathrm{m}, 0\ \mathrm{s})$ (dotted line) and at $(x, y, t) = (3.5\ \mathrm{m}, 2.5\ \mathrm{m}, 30\ \mathrm{s})$ (solid line).

3.5a).

3.4.2. No-fence experiment

A reference experiment without a fence was performed to demonstrate the validity of the model and to check the spin-up time. Figure 3.4a displays the time series of the wind speed at the center of the calculation domain over the integration period. The calculation was computationally stable during the period. Moreover, because the initial profile occupied the whole calculation domain, it almost took 2.6 s to run the information from the western boundary to the eastern end. This time span was the spin-up period of the model. The effect of the inflow turbulence was observed at the central position after half of the period (Fig. 3.4a). The wind data

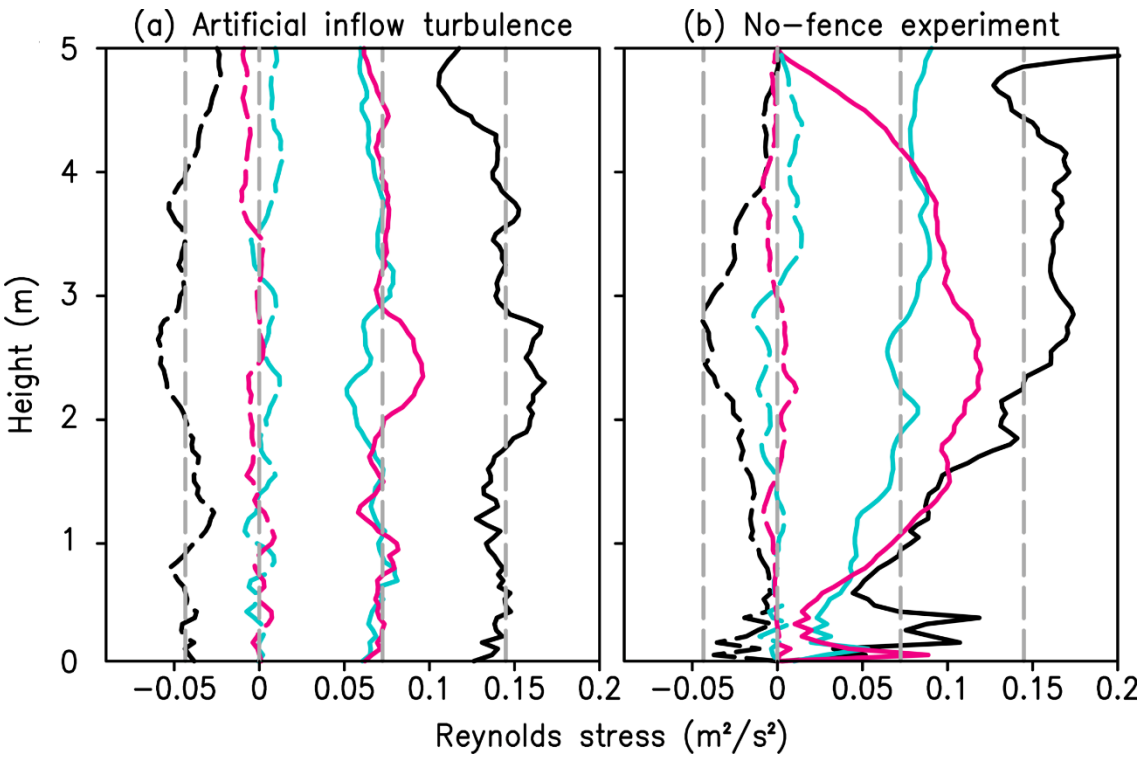

Fig. 3.5. Vertical profile of six components of Reynolds stress (a) in the artificial inflow turbulence at the center of the y-axis and (b) in the no-fence experiment at $(x, y) = (3.5\ \mathrm{m}, 2.5\ \mathrm{m})$. Solid lines are $\langle u'u' \rangle$ (black), $\langle v'v' \rangle$ (blue), and $\langle w'w' \rangle$ (pink). Broken lines are $\langle u'w' \rangle$ (black), $\langle u'v' \rangle$ (blue), and $\langle v'w' \rangle$ (pink). The grey dotted line indicates the target values of $\langle u'w' \rangle$, $\langle u'v' \rangle$ and $\langle v'w' \rangle$, $\langle v'v' \rangle$ and $\langle w'w' \rangle$, and $\langle u'u' \rangle$ from left to right.

calculated in the CFD module was discarded before 10 s, and the data segment selected after 10 s was input into the snow module. Therefore, we used 201 ensemble members to calculate a snowdrift amount and the snow particles' trajectories. The vertical profile of the wind speed at the final time step is shown in Fig. 3.4b. The instantaneous westerly wind fluctuated around the logarithmic low imposed as the mean value at the inflow boundary. Figure 3.5 shows the second-order turbulent statistics at the inflow boundary in Fig. 3.5a and the center of the calculation domain ($x = 3.5\ \mathrm{m}, y = 2.5\ \mathrm{m}$) in Fig. 3.5b. Although $\langle u'u' \rangle$ decreased slightly and $\langle w'w' \rangle$ increased above z = 1.0 m at the center of the domain, the turbulent kinetic energy, defined as $\frac{1}{2}(\langle u'u' \rangle + \langle v'v' \rangle + \langle w'w' \rangle)$, was comparable with that at the inflow boundary. The distribution

of the three components of the normal stress assumed at the inflow boundary was only slightly modified. Due to the effect of the no-slip condition at the ground surface, $\langle w'w' \rangle$ was decreased near the surface, which could decrease $\langle u'w' \rangle$, especially near the surface at the center of the domain. However, $\langle u'w' \rangle$ at the center was still half the prescribed value at the inflow boundary.

Figure 3.6 shows the snowdrift distribution as the sum of the amount of snow accumulation in each trajectory calculation. According to Eqs. (3.19) and (3.24), the terminal fall velocity of snow particles was 0.3 m s^{-1}, and snow particles below a height of 0.5 m at the initial position had a large volume flux. Snow particles were advected by the background flow of ~4 m s^{-1} until deposition. Hence, most of the snow particles fell within 7 m of the western boundary (Fig. 3.6). The horizontal distribution of the snowdrift depended on the vertical distribution of the snow volume flux. The height of the snowdrift was expected to be about 0.2 m in the calculation domain if the snow volume flux exceeded 6.0×10^{-7} m^3 m^{-2} s^{-1}, corresponding to the flux at a height of 0.6 m. No more snow accumulation was possible after the friction velocity exceeded the threshold [Eq. (3.22)]. The results indicated that we could test the blocking effect of a fence at $x = 0$ because a snowdrift was formed beyond the point without the fence.

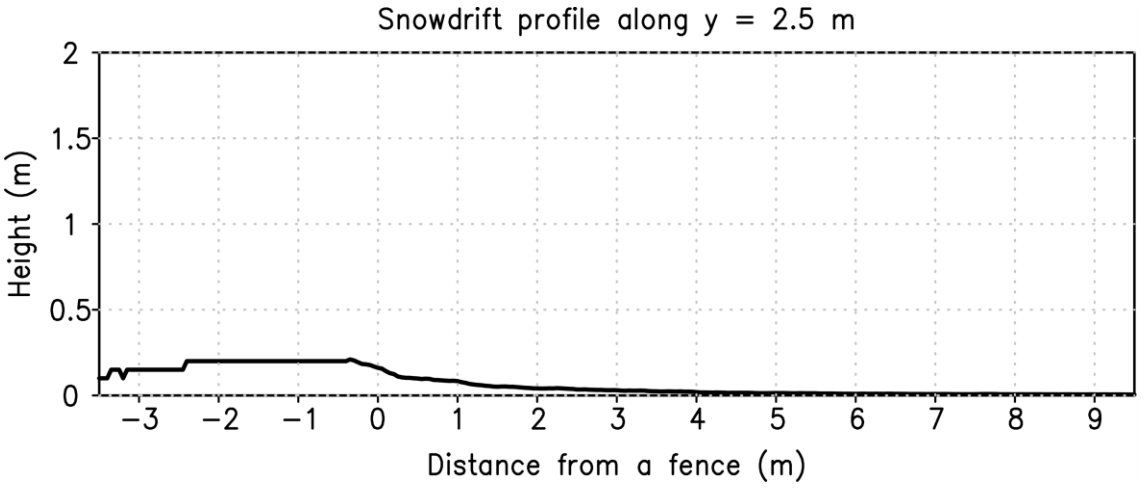

Fig. 3.6. Snowdrift profile for the no-fence experiment in the cross section along $y = 2.5$ m, as the sum of the amount of snow accumulation for each trajectory calculation.

3.4.3. Two-dimensional fence experiment

The horizontal wind observed in the no-fence experiment was distorted by the two-dimensional fence normal to the dominant wind direction, which created an ascending motion on the windward side and a swirling eddy in the cross section on the leeward side (two snapshots in Fig. 3.7). The upper-level wind was intensified around the top of the fence. These wind profile features were consistent with previous studies (Uematsu et al. 1991; Liu et al. 2016). However, the eddies were generated successively from the leeward side of the fence and flowed downstream following the dominant wind flow, and the size and position of the eddies in the cross section varied irregularly over time (Fig. 3.7). At 10 s, a single eddy extended 1 m from the fence and

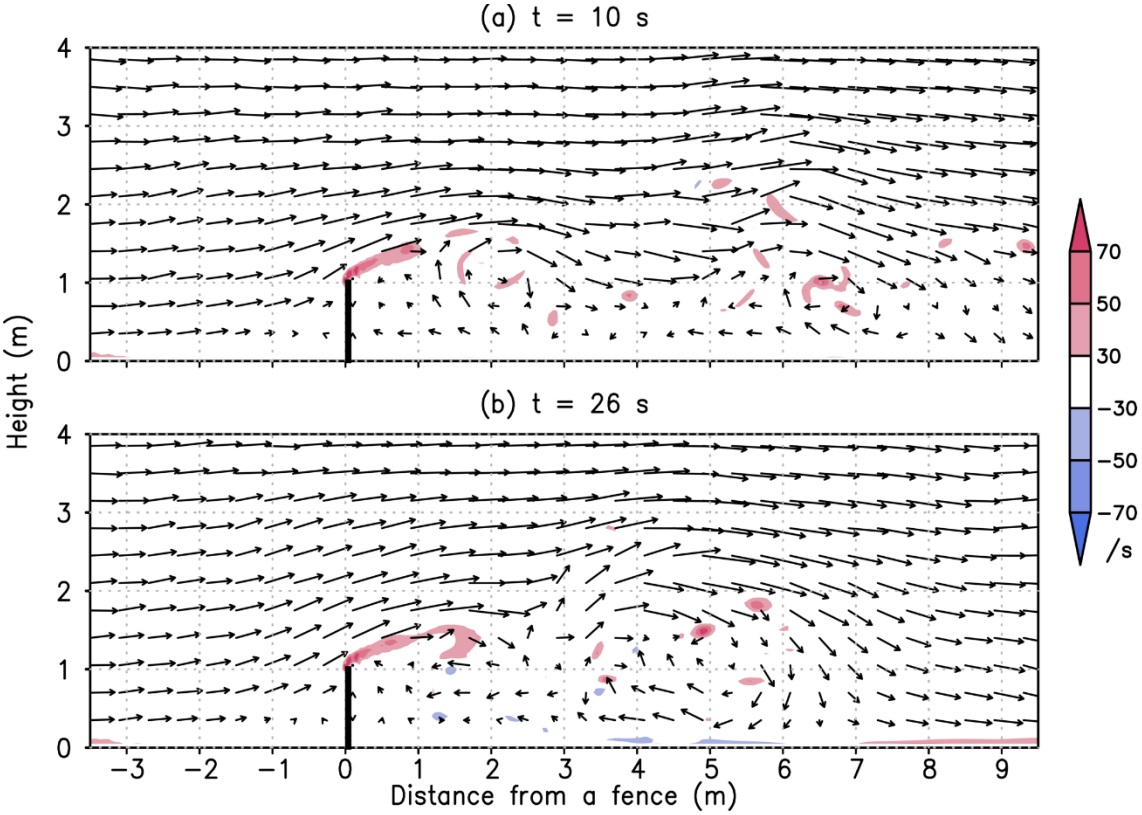

Fig. 3.7. Snapshots of the wind vectors (vectors) and vorticity (shading) around the two-dimensional fence in the cross section along $y = 2.5$ m at (a) 10 and (b) 26 s. The solid line at $x = 0$ shows the two-dimensional fence.

there was another larger eddy from $x = 6$ to 8 m (Fig. 3.7a). The large eddy flowed in the eastern direction and left the domain after 11 s (not shown). At 26 s, there were large eddies just to the east of the fence and further downstream from $x = 3$ to 6 m (Fig. 3.7b). These larger eddies had a strong reverse flow near the surface because the intensified wind at the top of the fence was separated behind the fence. Eddies successively separated from the east side of the fence. The eddies caused by the fence augmented the fluctuations with a larger scale and a lager timescale.

The snowdrift distribution in the two-dimensional fence experiment (Fig. 3.8a) was different from that in the no-fence experiment (Fig. 3.6). Almost all of the snowdrift was distributed on the windward side of the fence because the surface wind speed was attenuated just to the west of the fence. The highest snowdrift was about 0.5 m high at $x = -1.3$ m. These results were consistent with previous studies using a conventional numerical simulation (Uematsu et al. 1991; Alhajraf 2004) and observations (Tabler 1994). On the leeward side of the fence, few snowdrifts formed except for from $x = 5$ to 7 m. This distribution was consistent with the first snowdrift development regime in Tabler (1994), which is explained in detail in Section 3.5. There were three reasons for this result. First, most of the snow particles that went over the fence did not accumulate just east of the fence because the strong wind above the fence accelerated the snow particles. Figures 3.8b-d show the trajectories of three initial positions of the snow particles driven by all the wind profile data segments. Most of the particles starting from higher heights went over the fence and were blown through the calculation domain, such as the particles that started from a height of 1.4 m (Fig. 3.8d). However, most of the particles starting from a height of 0.3 m did not get over the fence (Fig. 3.8b) because these particles reached the grid on the windward side of the fence that had a friction velocity below the threshold [Eq. (3.22)]. Second, the eddies that were successively generated on the leeward side of the fence disturbed the

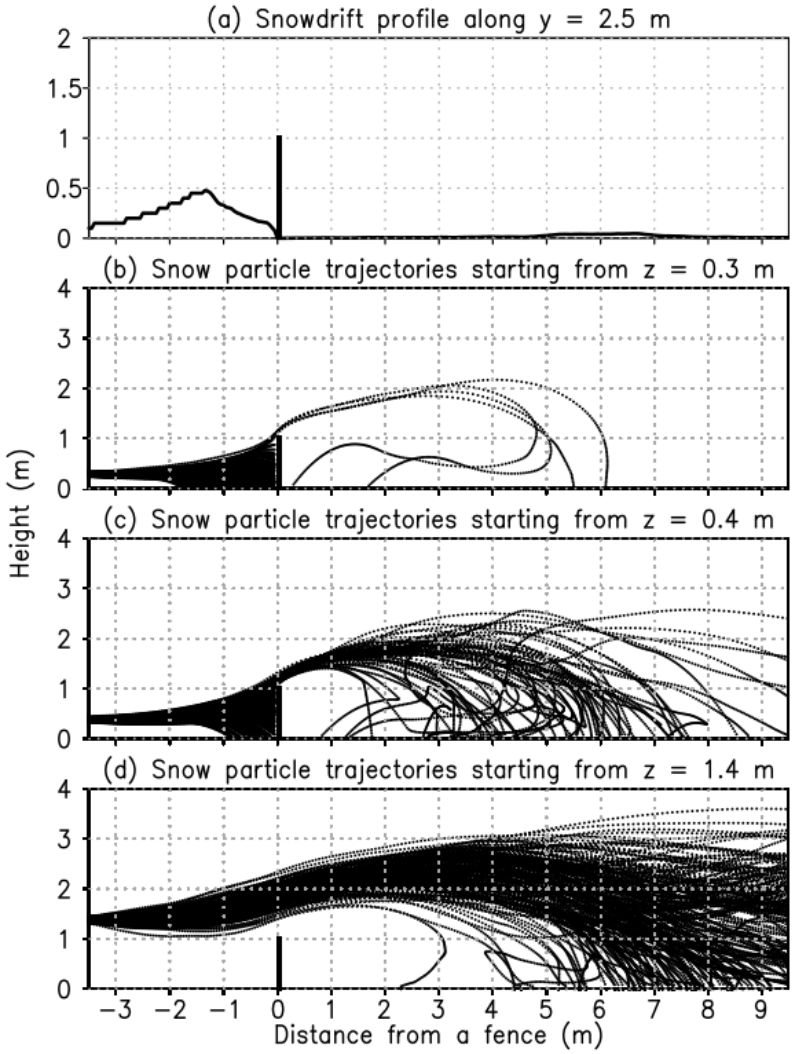

Fig. 3.8. (a) Snowdrift profile around the two-dimensional fence in the cross section along $y = 2.5$ m, as the sum of the amount of snow accumulation of each trajectory calculation. (b, c, d) Ensemble trajectories of snow particles at the center of the y-axis around the two-dimensional fence driven by all the wind data segments. The initial heights of the particles are (b) 0.3, (c) 0.4, and (d) 1.4 m. The position of the fence is shown by a solid line.

snowdrift development at a certain point because these transient eddies were generated by inflow turbulence and the snow accumulation in a single trajectory calculation depended on the transient eddies. For example, some particles starting from a height of 0.4 m subsequently followed the streamlines of the swirling eddies and fell to the east of the fence (Fig. 3.8c), but these particles fell on different grids in each wind profile data segment. Third, most of the snow particles

accumulating on the leeward side of the fence had a small snow volume flux, such as the particles starting from a height of 1.4 m. The snowdrift at the point where these particles fell was less than 5 cm high (Fig. 3.8a) because these particles had a small snow volume flux. In contrast, most of the snow particles starting at a height of 0.3 m with a large snow volume flux fell on the surface of the windward side. Thus, the two-dimensional snow fence was an effective obstacle to snowdrift development on the leeward side compared with the snowdrift distribution in the no-fence experiment (Fig. 3.6).

3.4.4. Three-dimensional fence experiment

The three-dimensional fence greatly changed the wind flow around the fence (Figs. 3.9, 3.10). In contrast to the two-dimensional fence experiment, the wind flow vector was three-

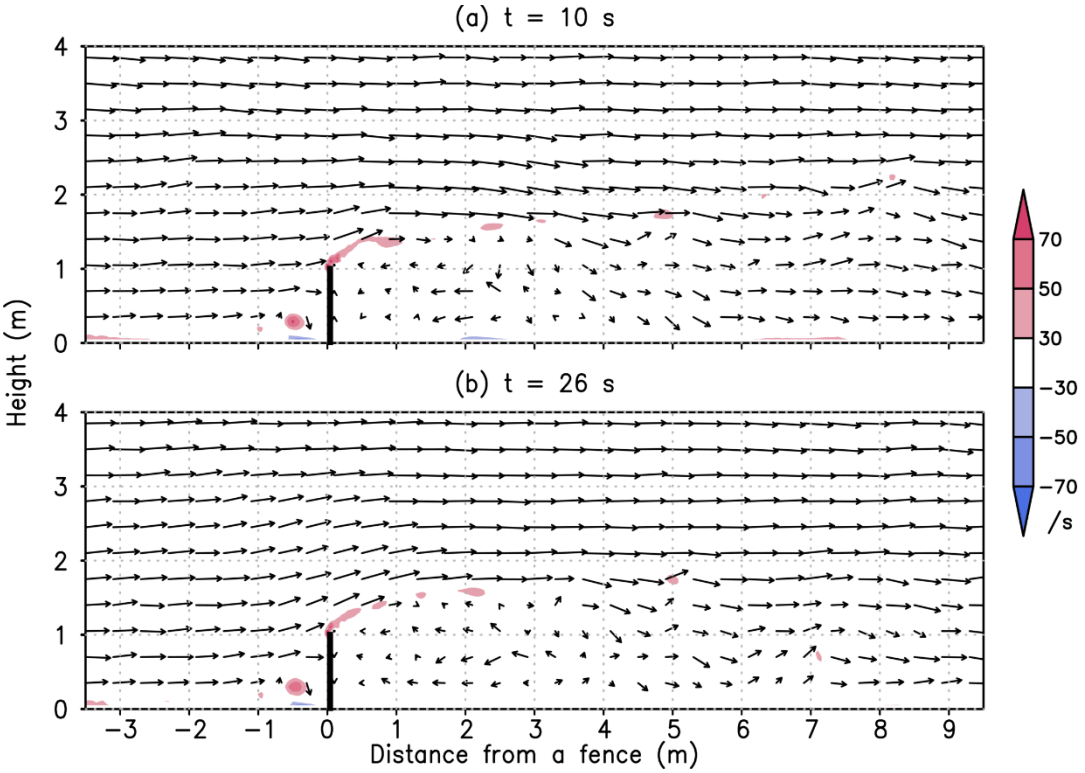

Fig. 3.9. Snapshots of wind vectors (vectors) and vorticity (shading) around the three-dimensional fence in the cross section along $y = 2.5$ m at (a) 10 and (b) 26 s. The position of the fence is shown by a solid line.

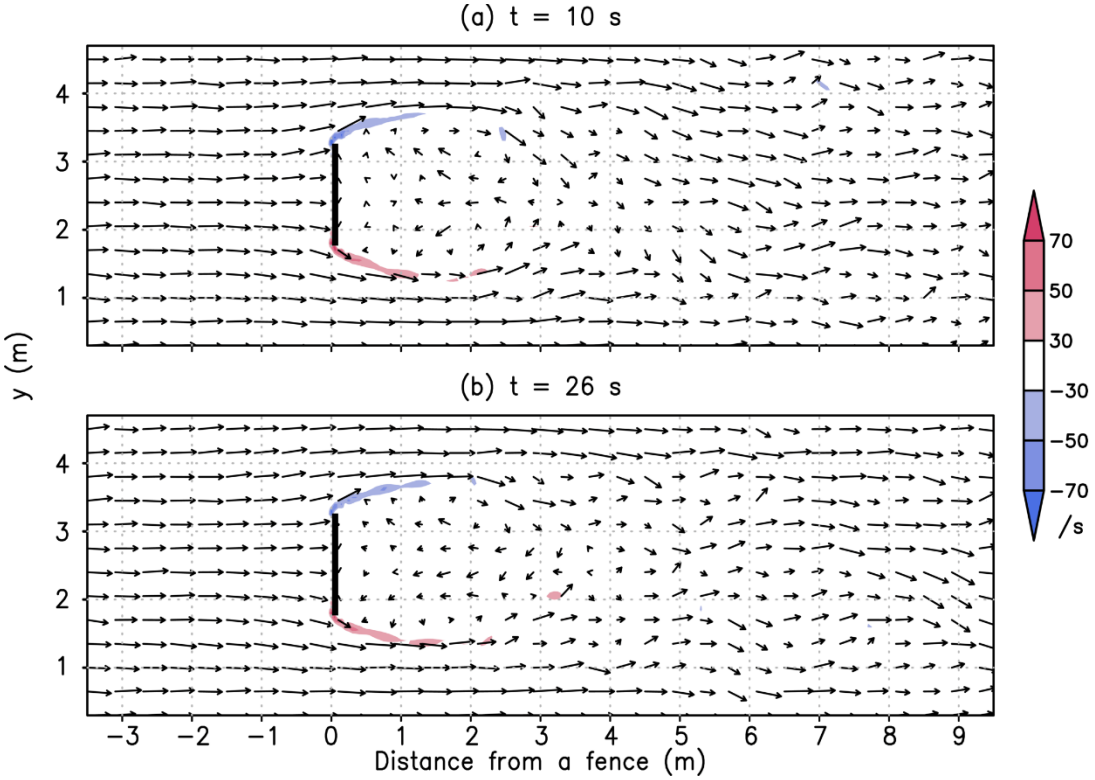

Fig. 3.10. Snapshots of wind vectors (vectors) and vorticity (shading) around the three-dimensional fence on the horizontal plane along $z = 0.5$ m at (a) 10 and (b) 26 s. The position of the fence is shown by a solid line.

dimensional in the three-dimensional fence experiment. The reverse flow along the center of the fence was weaker than that in the two-dimensional fence experiment around the surface on the leeward side around $x = 2$ m at 10 s (Fig. 3.9a). The low-level wind flow was horizontally diffluent and went round the fence, and there was a dipole pattern on the leeward side, with a weak wake flow toward the center of the fence on the horizontal plane at $z = 0.5$ m (Fig. 3.10a). The wind flow at 26 s had a weak eddy from $x = 1$ to 3 m on the vertical plane (Fig. 3.9b). These features were consistent with a previous study that simulated wind flow around a three-dimensional obstacle with the LBM (Han et al. 2021). On the horizontal plane, there was still a dipole pattern, but the turbulent flow 4 m east of the fence was more intense after a while due to the spread of turbulence generated by eddies on the horizontal plane on the leeward side (Fig. 3.10b).

In the three-dimensional fence experiment, the snowdrift had a two-dimensional distribution (Fig. 3.11a). The snowdrift along the center of the *y*-axis on the windward side was similar to that in the two-dimensional fence experiment (Fig. 3.11b). On the leeward side, snowdrift was not formed behind the fence along the center of the *y*-axis, but it was formed in the no-fence zone (Fig. 3.11c). This snowdrift developed ahead of the split flow because there were weak flow lines around the surface (Fig. 3.10). This snowdrift profile associated with the split flow was consistent with previous studies of snowdrifts around cubes (Beyer et al. 2004; Okaze et al. 2013). The snow particles clarified the three-dimensional trajectories for snow deposition. All of the particles starting from heights of 0.3 (not shown) and 0.4 m (Fig. 3.12a) fell on the windward side of the fence, whereas some particles from the same heights went over the fence in the two-dimensional fence experiment. This difference was probably caused by the lower wind

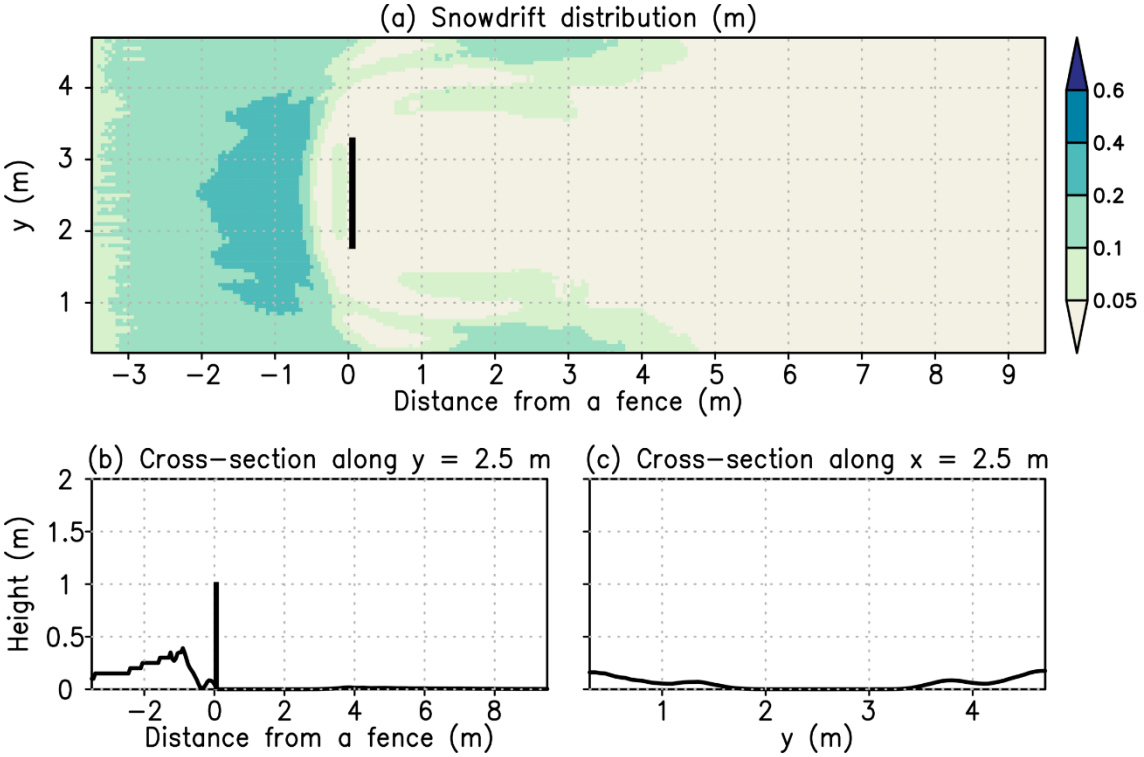

Fig. 3.11. (a) Snowdrift height around the three-dimensional fence in the cross section along (b) $y = 2.5\,\mathrm{m}$ and (c) $x = 2.5\,\mathrm{m}$. The snowdrift is the sum of the amount of snow accumulation of each trajectory calculation. The position of the fence is shown by a solid line in (a) and (b).

speed just above the three-dimensional fence due to the energy loss accompanied by the horizontal diffluent flow (Fig. 3.10). The snow particles' trajectories on a horizontal plane indicated the snowdrift formation process along the split streaks on the leeward side. For example, some snow particles from $(y,\ z) = (2.5\ \mathrm{m}, 0.5\ \mathrm{m})$ did not flow over the fence because they collided with the fence, whereas most of the snow particles from $(y,\ z) = (1.5\ \mathrm{m}, 0.5\ \mathrm{m})$ did not collide with the fence and fell along the stream of the horizontal diffluent flow (Fig. 3.12c, d). These low-level

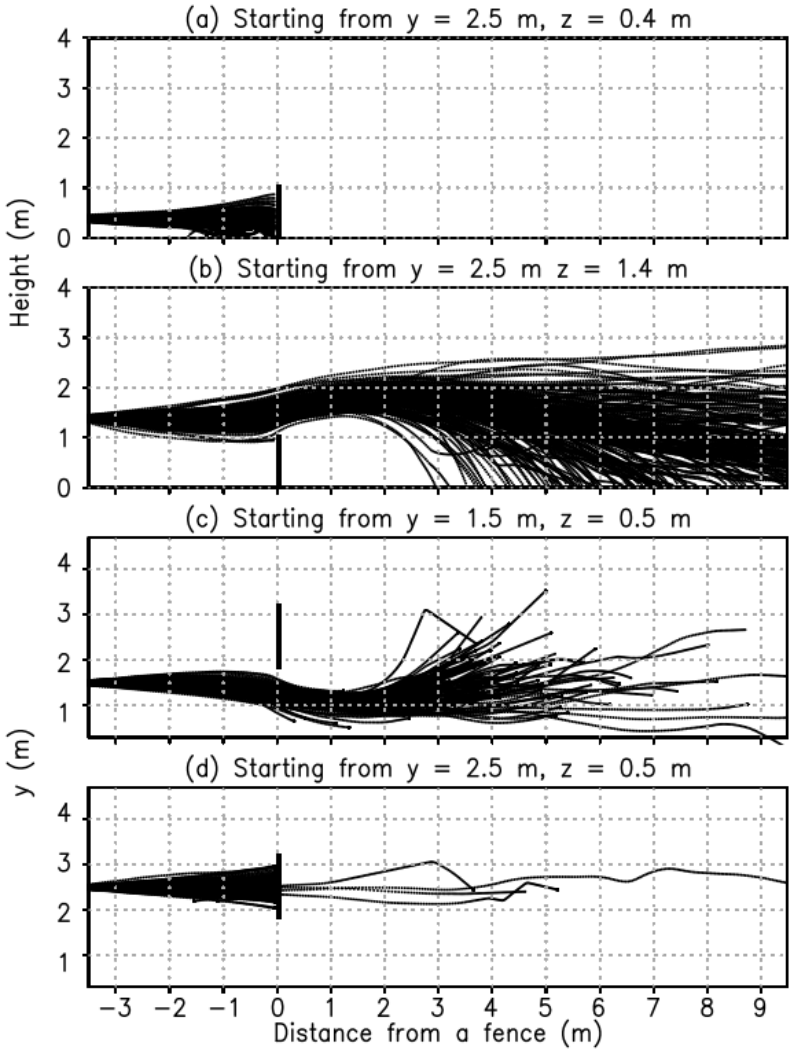

Fig. 3.12. Ensemble trajectories of snow particles at (a, b) the center of the y-axis and (c, d) along $z = 0.5\ \mathrm{m}$ around the three-dimensional fence driven by all the wind data segments. The initial positions of the particles are (y, z) = (a) (2.5 m, 0.4 m), (b) (2.5 m, 1.4 m), (c) (1.5 m, 0.5 m), and (d) (2.5 m, 0.5 m). The position of the fence is shown by a solid line.

particles formed the forking snowdrift on the leeward side.

3.4.5. Snowdrift potential

We introduced the snowdrift potential, based on 201 pieces of the snowdrift simulation using the different initial background flow sampled from the CFD calculation from 10 to 30 s. For example, a 50% snowdrift potential meant that about 100 initial wind profiles satisfied the condition of the development of a snowdrift with a height of > 5 cm, corresponding to a single vertical grid interval, when an infinite number of snow particles flowed in from the western boundary. Figure 3.13 shows the snowdrift potential for the three experiments. Snowdrift potential in the no-fence experiment was more than 80% over the calculation area because the friction velocity under a height of about 0.3 m was below the threshold. This result indicated that the

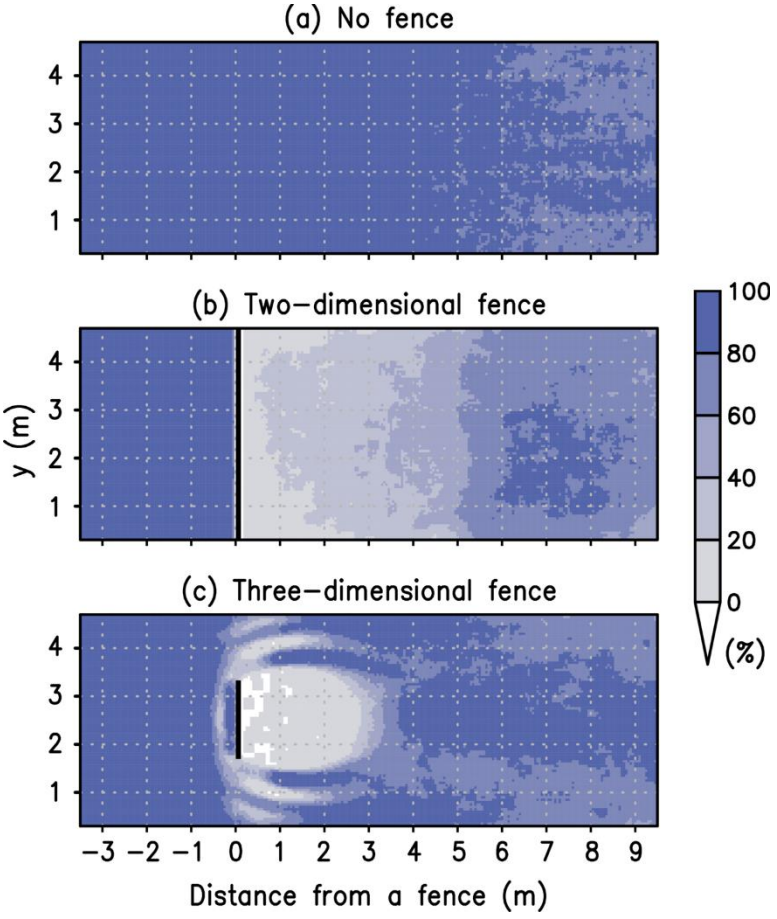

Fig. 3.13. Snowdrift potential (a) for no fence, (b) around the two-dimensional fence, and (c) around the three-dimensional fence. The position of the fence is shown by a solid line.

snowdrift could form anywhere in the calculation domain from accumulating snow particles blowing from the western boundary. In contrast, snowdrift potential around the two-dimensional fence decreased greatly on the leeward side of the fence, to less than 40% just 4 m to the right of the fence. The snowdrift potential was low just behind the three-dimensional fence but high elsewhere. The higher probability region extended along two arcs from the borders of the fence to the downstream area. In addition, most of the snowdrift potential over 4 m behind the fence was more than 80%. These results showed that snow fences could prevent snowdrift formation on the leeward side of the fences even if a large number of snow particles were blown by a strong drifting snow event. However, the two-dimensional fence was more effective than the three-dimensional fence. The three-dimensional fence used in this study was not sufficiently long, with a width of 1.5 m compared with a height of 1 m. Therefore, the separation of eddies near the sides of the fence induced a flow behind the fence, which led to a more region of low wind speed behind the fence compared with that for the two-dimensional fence. As a consequence, the small snowdrift potential region for the three-dimensional fence was shorter than that of the two-dimensional fence, but the region with a potential of less than 20% extended up to 3 m behind the fence.

3.5. Conclusions and discussion

We developed the CFD and snow particle modules to evaluate the snow accumulation around snow fences. The snow particles were driven by the wind flow in the channel sampled from the CFD model experiment with the LBM. The snow particles' motion was modeled following Nishimura and Hunt (2000) and Nemoto and Nishimura (2004) and the accumulation was computed as a function of the friction velocity in the viscosity layer. We designed an experiment with no fence, and experiments with a two-dimensional fence or a three-dimensional

fence, both installed normal to the dominant wind direction. The snowdrift distributions in both the two-dimensional fence and the three-dimensional fence experiments were high on the windward side of the fence because most snow particles from lower levels did not go over the fence due to the weak wind, and a varying, strong swirling eddy on the east of the fence often blew snow particles from higher levels to out of the domain. However, around the three-dimensional fence, the snow accumulation was found on the leeward side along the horizontally diffluent wind flow. The CFD integration in the three-dimensional fence experiment increased the vorticity activity of the vertical component, whereas that in the two-dimensional fence experiment increased the vorticity activity of the horizontal component. The three-dimensional fence experiment was designed with the fence blocking 30% of the channel width, but the ratio of the fence length to channel width probably affected which horizontal or vertical vorticity was dominant in the downward energy cascade.

The snowdrift model in this chapter has two main advantages compared with previous models. First, the ensemble simulation in our model is useful for evaluating the effect of the fence; it enables us to estimate not only the quantitative snowdrift distribution (Figs. 3.8a, 3.11), but also the probability of the snowdrift development (Fig. 3.13). This kind of information helps us to warn drivers by capturing low-probability snowdrift formation events that can cause traffic disruption. Second, temporal variation of the boundary conditions of the CFD module due to snowdrift formation can be added easily to our model. Most previous studies did not update the snow surface boundary in the calculation because of the high computational cost of conventional CFD algorithms and the technical complexity of updating boundary conditions during the simulation.

Even though this chapter focused on model development, we discuss the feasibility of our model on a qualitative reproduction by our model of three regimes of snowdrift formation

around a solid fence described by Tabler (1994). In Regime I, the snowdrift developed on the windward side of the fence with cavity between the fence and the snowdrift, and the snowdrift was 0.6 times the height of the fence. Our simulation result for the two-dimensional fence was consistent with the characteristics of Regime I (Fig. 3.8a). However, the simulation results did not reproduce the other regimes of filling the cavity (Regime II) and snowdrift development on the leeward side of the fence (Regime III). Our model should be parallelized to enable a longer integration time to reproduce these regimes in a reasonable computational time. Moreover, the boundary condition in the CFD module must be updated successively, so as to include a possible change of flow due to a change in snowdrift surface. Furthermore, the resuspension and redeposition of the particles should be included in the snow particle module to estimate snowdrifts more accurately.

To achieve a more accurate snowdrift simulation, other snow motion and accumulation processes must be included. For example, resuspension of snow particles from the surface is an important process in drifting snow. In the present model, this process was implicitly included in the prohibition of snow accumulation on the surface by strong wind. However, we did not consider the trajectories and redeposition of resuspended snow particles. The resuspension processes are aerodynamic entrainment, rebound and splash (Shao and Li 1999; Ammi et al. 2009). Moreover, the initial condition of the snow surface should be prescribed because snow particles on the surface drift when the friction velocity exceeds the threshold velocity.

This chapter was limited to experiments with no interactions between snow and wind. In this study, snow particles were affected by the wind, but the wind was not affected by the snow particles; thus, the coupling was one-way. By considering the interaction between snow and wind as a two-way coupling, the wind velocity is slightly reduced by the momentum exchange between snow particles and wind. This modification may change the trajectory of snow particles (Figs.

3.8b, c, d, 3.12) so that they fall short on the windward side of the fence. Moreover, there is an interaction between the snow surface and wind flow. The snow accumulation changes the bottom boundary condition in the CFD calculation. Our model can be extended easily to allow temporal variation of the boundary conditions because the LBM is simpler than other algorithms and more suitable for complicated boundary conditions. Because the snow particles generally accumulated where the wind speed was low on the windward side of the three-dimensional fence (Fig. 3.11), we can easily presume that the snow surface on the windward side is asymptotic to a streamline that crosses the top of the fence. We can readily implement this interaction process simply by combining the CFD and the snow particle modules, but this will be addressed in future work.

Although this chapter is limited to examining the feasibility of applying the LBM to drifting snow and snowdrift modeling, we can still compare the simulation results with observations. An Observation of drifting snow around a long, wide, solid fence in Teshikaga, a small town in eastern Hokkaido, on February 18, 2019 were recorded over several hours (Okaze et al. 2019). The height and width of the fence were 1 and 6 m, respectively. The snow depth was measured along a line orthogonal to the center of the fence. The wind direction did not change

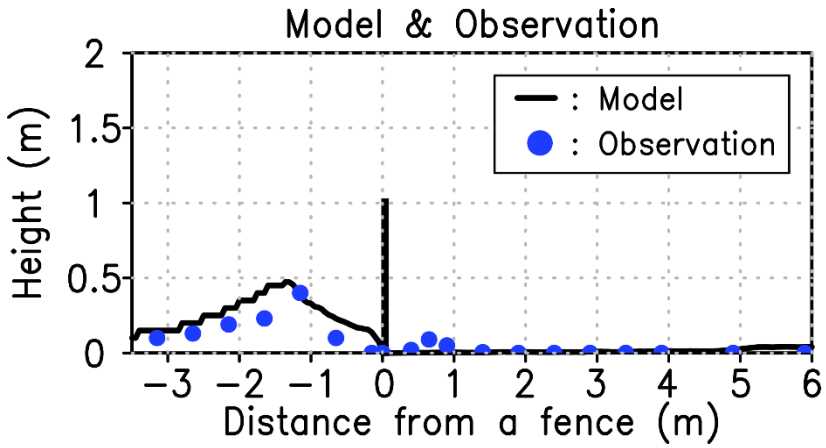

Fig. 3.14. Snowdrift profile around the two-dimensional fence in the cross section along $y = 2.5$ m (line) (as shown in Fig. 3.8a) and the snowdrift profile observed in Okaze et al. (2019) (blue circles).

much and was orthogonal to the fence. The fence setting was quite similar to that in the two-dimensional numerical experiment shown in Section 4.3. Comparing the observation with our results (Fig. 3.14) indicated that the snowdrift distribution in the numerical experiment and the peak location of the snowdrift at about $x = -1$ m were consistent with the observation. However, we cannot compare these results further because of the lack of high-resolution spatiotemporal observation data. Moreover, a fairer comparison is needed to improve the experiment design and improve the model components to represent realistically the inflow and surface boundary conditions and their interactions with drifting snow particles, such as rebounding and resuspension.

Chapter 4. Sensitivity Tests of the LBM Snowdrift Model

4.1. Introduction

Drifting snow particles form snowdrifts where wind speed is patchily weak due to constructions and landforms. Drifting snow is a phenomenon that snow particles on the surface or snowfall particles are blown by the strong wind. Studies of the numerical simulation of snowdrifts clearly increase with advance of the computer technology (Beyers et al. 2004; Tominaga et al. 2011a, 2011b; Zwaaftink et al. 2014; Okaze et al. 2018; Wang and Jia 2018; Zhang et al. 2021; Tanji et al. 2021). Numerical simulation overcomes limited opportunities of drifting snow events in the observation site, and a rough assumption of similarity in the wind tunnel experiments. It also enables us to evaluate essential physical processes by a set of the sensitivity tests. The most important point in the snowdrift simulation is resolving wind profiles around the surface because drifting snow particles move in the air following the wind profile; this movement of drifting snow particles is sometimes regarded as the main process of drifting snow. Uematsu et al. (1991) and Liston et al. (1993) started to calculate snowdrift heights and wind profiles based on the Reynolds-averaged Navier–Stokes equations model with turbulence parameterizations, such as *K*-theory and the k-ε model as a computational fluid dynamics (CFD) method. Recently, various CFD methods are used in the drifting snow simulation model such as the large-eddy simulation (LES; Zwaaftink et al. 2014; Okaze et al. 2018; Wang and Jia 2018) and the lattice Boltzmann method (LBM; Tanji et al. 2021).

Previous studies showed that not only snow particles movement in the air following wind profiles but also snow particles movement nearer the snow surface were essential to simulate drifting snow precisely because a transport amount of snow particles near the surface was generally larger than snow particles in the air above the surface (Matsuzawa and Takeuchi 2002;

Nishimura and Nemoto 2005). Drifting snow particles near the surface mainly consist of blown particles once accumulated on the surface. The process that accumulated snow particles are torn off from the surface by the wind shear stress is called resuspension. The wind strength determines the number of resuspended particles from the snow surface (Shao and Li 1999). Drifting snow particles at a low level above the surface are also influenced by the snow surface. For example, when drifting particles reach and collide the surface, some particles bound on the surface and other particles pop out from the surface by their impacts. The former is called a rebound process and the latter is called a splash process. Snow particles with small kinetic energy after collision with the surface do not rebound and are deposited on the surface. Resuspension, rebound and splash are collectively called sub-processes of drifting snow particles. Conventional models which targeted drifting snow particles' movement have succeeded in reproducing them in limited domains (Zwaaftink et al. 2014; Okaze et al. 2018; Niiya and Nishimura 2022), but no one has applied these models to the simulation of snowdrift formation due to large computational costs in calculating turbulent flow near the surface and tracing drifting snow particles. We now then raise a question how much sub-processes contribute to the snowdrift distribution. In addition, previous studies of the sub-processes demonstrated that the sub-processes development depends on the physical properties of snow particles, such as diameter, density, and shape (Bagnold 1941; Ammi et al. 2009). No one also understand the influence of the physical properties of snow particles on snowdrift formation. In order to make them clear with the numerical simulation, we should resolve the bottlenecks of large computational costs in both of estimation of turbulent wind flow and drifting snow particles' trajectories.

The snowdrift model developed by Tanji et al. (2021) is a suitable tool for simulating snowdrifts with the sub-processes of snow particles because turbulent flow and trajectories of drifting snow particles can be calculated in the model. The model consists of the CFD module

and the snow particle module. The LBM (McNamara and Zanetti 1988) is used as the CFD solver in this model because the LBM algorithm has simpler implementation and higher efficiency in parallel computation than the conventional CFD algorithm (Chen and Doolen 1998; Han et al. 2019). The LBM also had the advantage of the snowdrift simulation in the various structures of obstacles due to its suitability for complicated boundary condition. Snow particles in the snow particles module are traced as the Lagrangian method using the result of the wind profile estimated by the CFD module. To reduce computational costs by tracing all resuspended particles under strong wind conditions (Shao and Li 1999), we cope with a finite number of snow particles as representative ones. Tanji et al. (2021) demonstrated that the model provided reasonable formation of the snowdrift compared with the observation (Tabler 1994) and the conventional numerical simulation (Uematsu et al. 1991; Alhajraf 2004) in a qualitative sense. However, the model by Tanji et al. (2021) cannot estimate snowdrift distribution quantitively because the model calculates only a moving process of drifting snow particles in the air but does not calculate other processes explicitly such as a resuspension process, a rebound process, and a deposition process of drifting snow particles.

This chapter aims to investigate the contribution of the sub-processes and the physical properties of snow particles to the snowdrift distribution with the numerical simulation model. The model we used was the snowdrift model developed by Tanji et al. (2021), which was imposed the sub-processes. Sensitivity tests are conducted about not only the sub-processes but also the physical properties of snow particles because features of snow particles influence both the main process and the sub-processes of drifting snow particles. We targeted 4 factors on the snowdrift distribution, the resuspension process, and the rebound process, and diameter and density of drifting snow particles. The splash process was not considered in this chapter because the splash process developed less often than the resuspension and the rebound processes (Okaze et al. 2018).

Sublimation often occurs on the top of the drifting snow area, but it can be excluded because of less contribution to the snowdrift distribution. We used the observed vertical wind profile as the boundary conditions of the model to compare the results of the snowdrift with the model and observed snowdrift distribution quantitively. The remaining part of this chapter is organized as follows; in Sections 4.2 and Section 4.3, we explain the model method and the observation data we used, respectively; in Sections 4.4, we explain the experiments in detail; in Sections 4.5 we show the observation data, the results of the control experiment, and the results of the sensitivity tests; and in Section 4.6, we conclude the chapter.

4.2. Observation data

We used observation data acquired in Teshikaga Town, in eastern Hokkaido in Japan (144.467°E and 43.502°N; Fig. 4.1; Okaze et al. 2019). This site was a flat field with no obstacle

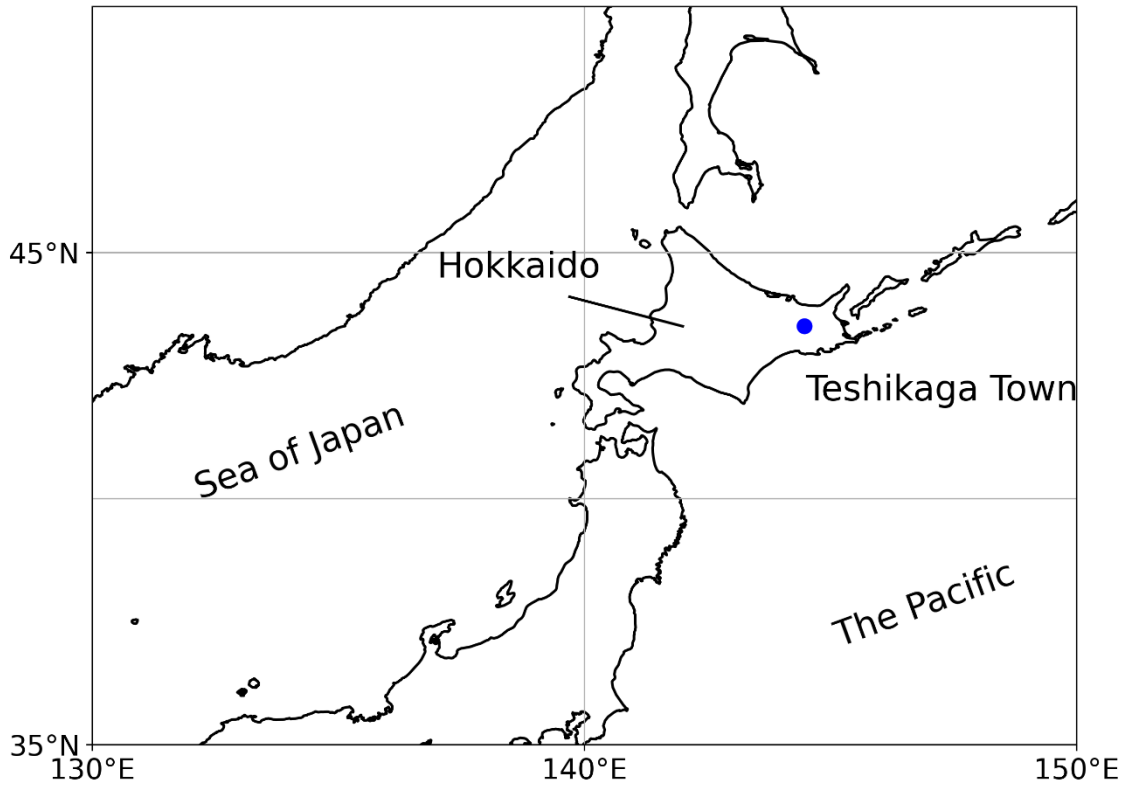

Fig. 4.1. A map around Japan. A blue circle denotes the observation site in Teshikaga Town.

over 500 m on the windward side of the observation point. The solid fence without porous was 6 m length, 4 mm thickness, and 1 m height, and was set perpendicularly to the dominant wind direction on the field (Fig 4.2a). On the site, wind speed and direction were observed with cup anemometers every 10-minute. The anemometers were set at four levels of the observation tower, about 1 m, 1.5 m, 3 m, and 7 m heights above the surface. Amount of drifting snow inflow were also measured at the same levels with snow particles counters (SPCs) every 1 second output.

On 18 Feb 2019, strong wind and drifting snow were recorded in the morning, and a snowdrift was formed around the fence. The day before the drifting snow event, it had snowfall with weak wind, and the field was uniformly covered with about 2 cm of snow height. However, no snowfall was recorded while the drifting snow was developing on 18 February according to observation at AMeDAS point near the site. On the day following the drifting snow event, a 1-dimensional snowdrift height of the cross-section along the center of the fence was measured (Fig 4.2b). We used these data of the wind and the snowdrift height in order to input as the boundary condition of the model and to compare with the result of the model simulation, respectively.

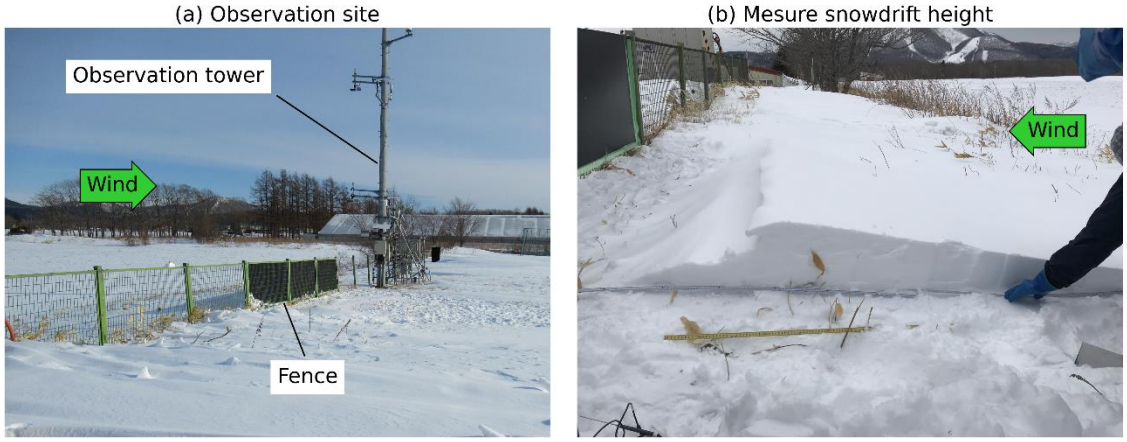

Fig. 4.2. (a) A photo showing the observation tower loaded with anemometers and SPCs and a fence at the observation site. (b) A photo showing the measurement of a snowdrift height in the cross-section along the center of the fence. Vectors show the main wind directions in the site. These photos were taken on another day than the observation day we used in this chapter.

4.3. Model

4.3.1. CFD module

The CFD module in this chapter was the same as the CFD module in Tanji et al. (2021) except for the non-dimensional viscosity of the air which was changed to 2.0×10^{-6} in order to simulate the flow with a higher Reynolds number. The module was based on a three-dimensional LBM model, the D3Q19 model with the single relaxation time collision operator. It was also noted that the sub-grid scale parameterization with the Smagorinsky model was implemented to estimate the eddy kinematic viscosity (Smagorinsky 1963; Feng et al. 2007; Onodera et al. 2013; Wang et al. 2014; Suga et al. 2015).

The model domain was a finite channel in the three-dimensional space spanned by the wind direction, x, the horizontal direction normal to x (or fence direction), y, and the vertical direction, z. Hereafter, for convenience, the negative and positive ends of x in the domain are called the western and eastern boundaries; those of y are called the southern and northern boundaries; and those of z are called the bottom and top boundaries. The western and eastern boundary condition was the inflow and the free-flow boundary conditions (Hecht and Harting 2010), respectively. The value of the initial and the inflow conditions were made by observation data and will be referred to in Section 4.4.1. The eastern boundary contained 20 grids of the damping zone with 500 times larger constant Smagorinsky coefficient than in the other domain (Inagaki et al. 2017). The southern and northern boundaries were imposed as the periodic boundary conditions. The top boundary was a free-slip boundary (*i.e.,* $\frac{d\boldsymbol{u}}{dz} = 0$, where $\boldsymbol{u}$ is the macroscopic velocity) and the bottom and the fence were no-slip boundaries (*i.e.*, $\boldsymbol{u} = 0$).

4.3.2. Snow particle module

The snow particle module in this chapter consisted of 4 processes, a moving process, a resuspension process, a rebound process, and a deposition process.

The moving process described the blown snow particles in the air by the wind. Assuming that drifting snow particles are spherical, electrically neutral, and not driven by the lift force, the equation of motion for the particles is written as

$$\frac{d\boldsymbol{u_p}}{dt} = -\frac{3}{4}\left(\frac{\rho_a}{\rho_p d}\right) C_d V_R \left(\boldsymbol{u_p} - \boldsymbol{u}\right) - g\boldsymbol{k}, \tag{4.1}$$

where $\boldsymbol{u_p}$ (m s^{-1}) is the particle velocity vector, $\boldsymbol{u}$ (m s^{-1}) is the wind vector, $V_R = \left|\boldsymbol{u_p} - \boldsymbol{u}\right|$, $\boldsymbol{k}$ is an unit vector for z direction, g is the gravity acceleration (9.8 m s^{-2}). ρ_a was the densities of air (1.34 kg m^{-3}) which value was equivalent to that in the cold region. The particle diameter d and its density ρ_p were given differently in each experiment (Section 4.4.2). C_d is the drag coefficient for the particle (White 1974), calculated as

$$C_d = \frac{24\nu_0}{V_R d} + \frac{6}{1 + V_R d/\nu_0} + 0.4, \tag{4.2}$$

where ν_0 is the viscosity of the air (10^{-5} m^2 s^{-1}).

The resuspension process was activated when the wind speed near the surface was strong enough to peel off accumulated snow particles on the surface. The threshold value of the resuspension is decided by the friction velocity following Bagnold (1941) and Clifton et al. (2006) as

$$u_{*t} = 0.2\sqrt{\frac{\rho_p - \rho_a}{\rho_a} g d}. \tag{4.3}$$

The friction velocity u_* (m s^{-1}) on the snow surface is estimated with a wall function by a two-layer model in Werner and Wengle (1991) as

$$u_* = \begin{cases} \sqrt{\dfrac{2\nu_0|\boldsymbol{u}(z_b)|}{z_b}} & \text{for } |\boldsymbol{u}(z_b)| \le \dfrac{\nu_0}{2z_b} A^{\frac{2}{1-B}} \\ \left\{ \dfrac{1-B}{2} A^{\frac{1+B}{1-B}} \left(\dfrac{\nu_0}{z_b}\right)^{1+B} + \dfrac{1+B}{A} \left(\dfrac{\nu_0}{z_b}\right)^{B} |\boldsymbol{u}(z_b)| \right\}^{\frac{1}{1+B}} & \text{for } |\boldsymbol{u}(z_b)| \ge \dfrac{\nu_0}{2z_b} A^{\frac{2}{1-B}} \end{cases}, \quad (4.4)$$

where z_b is the height of the bottommost grid just above the snow surface, $A = 8.3$, and $B = 1/7$. A snow particle was launched from a grid where the friction velocity [Eq. (4.4)] exceeded the threshold value [Eq. (4.3)]. The initial velocity of the resuspended particle was equal to the wind speed at two grids above the resuspended point. A single particle had represented snow mass corresponding to the volume of snow on the grid (Section 4.4.1). A launched particle suspended in the air following Eq. (4.1) and the volume was released when the particle accumulated on the surface.

The snow particle which had reached the surface proceeded to the rebound or the deposition process. The process after a collision was determined by the kinetic energy that the snow particle had. When the particle velocity after the collision with the surface was enough to jump to a one-grid height of the CFD calculation, the particle rebounded. Otherwise, the particle proceeded to the deposition process and stayed unless the friction velocity there would be strong enough to activate the resuspension process. Elevation angle θ_r, azimuth angle φ_r, and restitution coefficient e_r are estimated when particles collided with the surface (Fig. 4.3). Although Okaze et al. (2018) suggested that these parameters follow the normal distributions, we gave the fixed values as a function of the incident angle θ_{in} as the elevation angle $\theta_r = 20° + 0.19\theta_{in}$, the azimuth angle $\varphi_r = 0$, and the restitution coefficient $e_r = 0.87 - 0.62\sin\theta_{in}$. We also assumed that a particle would rebound 50 times at most.

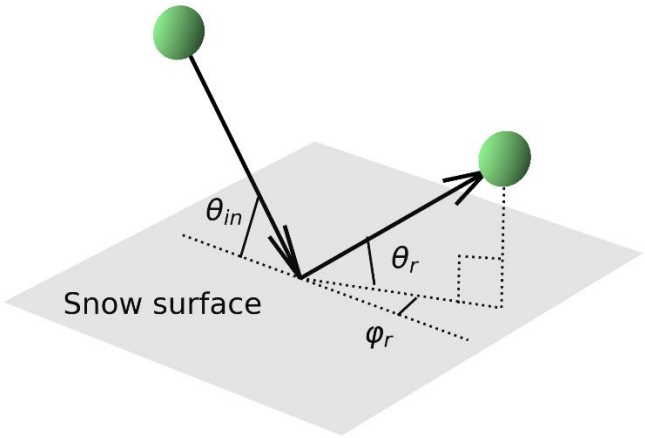

Fig. 4.3. Schematic of the incident angleθ_{in}, the elevation angle θ_r, and the azimuth angle φ_r in the rebound process. Green spheres show snow particles.

4.4. Experiments

4.4.1 Inflow condition

The imposed wind profile as the initial condition and the western boundary condition in the CFD module was the laminar logarithmic profile as

$$u_0(z) = \frac{u_*}{\kappa} \ln\left(\frac{z}{z_0}\right), \tag{4.5}$$

where the roughness length for a flat snow surface $z_0 = 0.1$ (mm) (Nishio and Ishida 1973), and von Karman's constant $\kappa = 0.4$. The friction velocity was determined by observed wind data using the least squares by the following procedure. First, we chose the period of the drifting snow event from the observed wind data and amount of drifting snow data and averaged the wind data at each height over the period. Second, we decided the friction velocity in Eq. (4.5) with the minimum of the root mean square error between the averaged observation data and the logarithmic profile. Finally, we got the logarithmic profile which was close to the observation results. In this chapter, we did not use the inflow turbulence as the inflow condition in the CFD module because the difference of the results between with the laminar inflow and with the inflow turbulence was small. See Appendix A for more detail.

The amount of inflow snow particles from the western boundary was also estimated by

the logarithmic profile decided above. We did not directly use SPCs data as the amount of inflow snow particles, however, because the vertical number of the SPC was not enough to make the vertical profile of the amount of drifting snow particles. Instead, following Tanji et al. (2021), a finite number of snow particles were uniformly distributed on the western boundary plane per 5.0 cm horizontally and per 2.5 cm vertically at the initial time. We assumed that a single particle represented snow mass corresponding to snow volume flux v_f ($\mathrm{m^3\ m^{-2}\ s^{-1}}$) depending on the height as

$$v_f(z) = \alpha \frac{n(z)u_0(z)}{\rho_p}. \tag{4.6}$$

Here, α was the constant to be consistent with the period of the drifting snow event. Snow concentration $n(z)$ (g $\mathrm{m^{-3}}$) is given (Shiotani 1953; Matsuzawa and Takeuchi 2002) by

$$n(z) = \min\left(30, 30\left(\frac{z}{0.15}\right)^{-\frac{0.30}{\kappa u_*}}\right), \tag{4.7}$$

where u_* is the estimated friction velocity.

4.4.2. Simulation set-up

The simulation domain covered with 18 m by 15 m by 5 m on a grid spacing of 0.05 m (Fig. 4.4). The fence was set at the center of the y-axis and 5 m from the western boundary. The fence was non-porous and solid, and the length was 6 m, the thickness was 0.1 m and the height was 1 m, mimicing the fence in the observation site. The location of the fence in x-axis was set as $x = 0$, which was 5 m from the western boundary. In the CFD calculation, the integration time was 3600 s after the spin-up time of 30 s and the time step was 0.5 ms; the results were sampled every 1 s from the initial time.

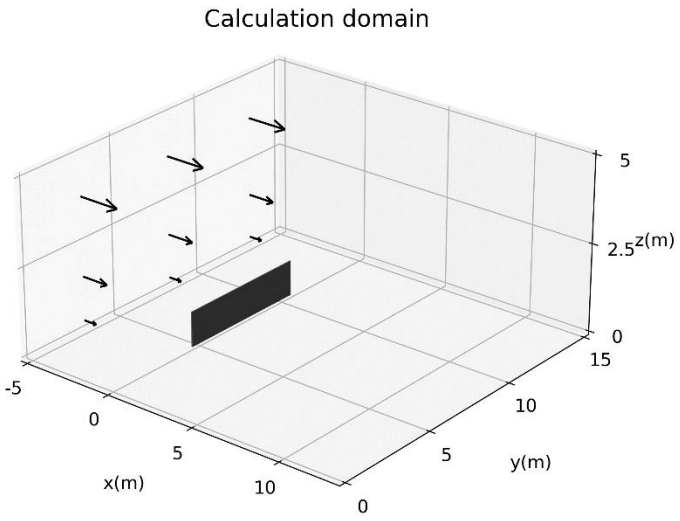

Fig. 4.4. Schematic of the calculation domain and the initial wind vectors in the experiments. A black panel is a fence.

We calculated trajectories of a finite number of snow particles [Eq. (4.1)] with a time interval of 1 ms. The integration time was set to 70 s maximum. The snow particles' calculations were conducted with several initial times of the wind and the snowdrift result was the sum of each member's result (Fig. 4.5). The initial wind profile was given to the snow particle module every 1 s (then, 3600 members in total members) and the wind profile was renewed every 1 s in the calculation. In a case where wind segments stated after 3530 s, the wind data after 3600 s keep the data at 3600 s. An accumulated snow particle gave a snowdrift height on the grid corresponding to the snow volume [Eq. (4.6)] per grid area. Snow particles within the snowdrift did not move, collapse, melt, or sublimate.

We conducted a control run and 4 sensitivity runs on rebound, resuspension, the diameter of the snow particles, and the density of the snow particles. The control run implemented all sub-processes and the diameter $d = 150\ \mu\text{m}$ and density of snow particles $\rho_p = 450\ \text{kg m}^{-3}$. The given diameter was close to the averaged diameter of $135\ \mu\text{m}$ observed at 1 m and 1.5 m heights, mainly caused by snowdrift (Tanji et al. 2021). The snow particles density given here was equivalent to that of compacted snow particles, considering that snowfall occurred

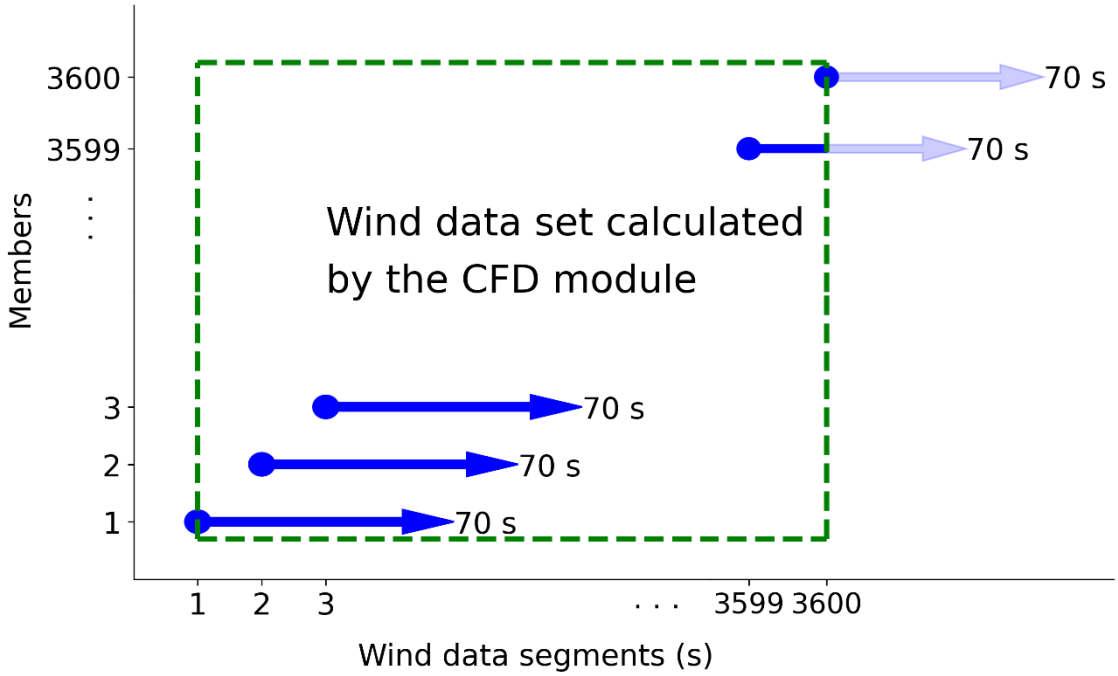

Fig. 4.5. Schematic of the wind data set calculated in the CFD module and the treatment of it in the snow particles module. Blue vectors show that we calculate snow particles' movements for 70 s maximum.

the day before the drifting snow event. In the sensitivity test of the rebound and the resuspension processes, we used the snow particle module without the rebound and the resuspension processes, respectively. In the diameter sensitivity tests, the snow particle module was set to $d = 100$ μm and 200 μm, which are dominant diameters of the drifting snow particles identified in the previous studies (Nemoto and Nishimura 2004; Nishimura et al. 2014). In the density sensitivity tests, the snow particles' module was set to $\rho_p = 910\ \mathrm{kg\ m^{-3}}$ and $200\ \mathrm{kg\ m^{-3}}$. The former value is equivalent to the density of an ice particle and the latter is equivalent to the density of growing compacted snow particles.

4.5. Results

4.5.1. Inflow condition

Figure 4.6 shows the observed time series of the wind speed and the snow volume flux

on 18 February 2019. Both the wind speed and snow volume flux were large between about 8:30 JST to 13:00 JST, especially between about 9:00 JST to 11:00 JST. The most robust wind speed was over $11\ \mathrm{m\ s^{-1}}$ at 7 m height and the largest snow volume flux was over $2.5 \times 10^{-4}\ \mathrm{m^3\ m^{-2}\ min^{-1}}$ at 1 m height in the period. The snow volume flux finely fluctuated even when the drifting snow was developing. The wind speed was abated to under $6\ \mathrm{m\ s^{-1}}$ after 15:00 JST. Figure 4.7 displays the vertical profile of the observed wind speed averaged over 1 hour and the estimated wind speed with the least squares method. The estimated wind speed of each time almost corresponded to the observed values and expressed intensified wind speed during the drifting snow event from 10:00 JST to 12:00 JST (Figs. 4.7b-d), but the wind speed at 3 m height had a little difference between the estimation and the observation. The snow volume flux was calculated by Eq. (4.6) and Eq. (4.7) with these logarithmic profiles of wind in Figure 4.7. The

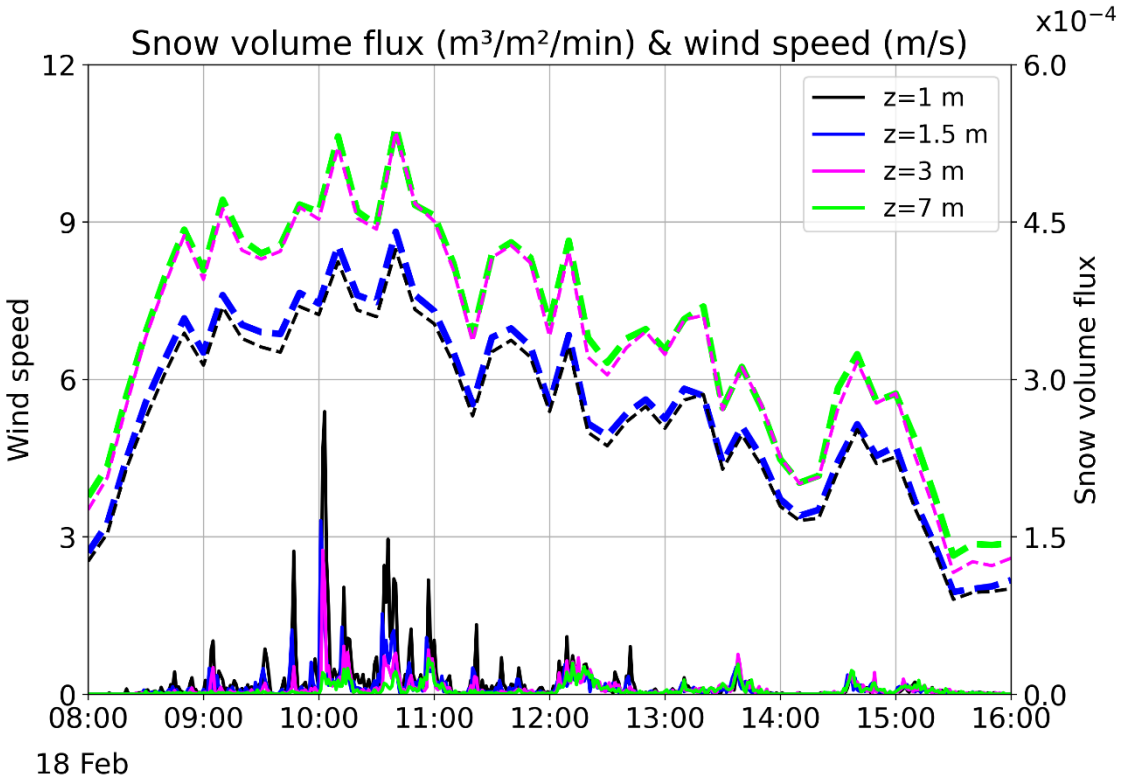

Fig. 4.6. Timeseries of the observed wind (solid line) and snow volume flux (dashed line) at $z = 1\ \mathrm{m}$ (black lines), $z = 1.5\ \mathrm{m}$ (blue lines), $z = 3\ \mathrm{m}$ (pink lines) and $z = 7\ \mathrm{m}$ (green lines) from 8:00 JST to 16:00 JST on 18 Feb 2019.

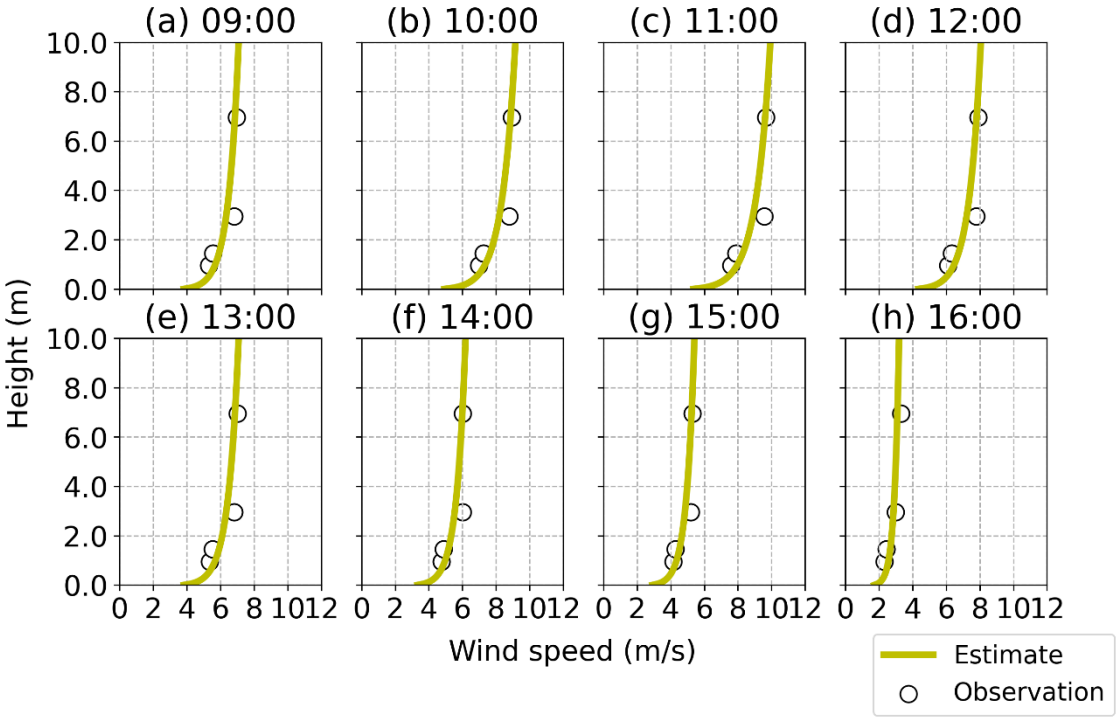

Fig. 4.7. Averaged vertical wind profiles over every 1 hour from 9:00 JST to 16:00 JST. Yellow lines show the estimated log profiles with the least squares and circles show the observed values.

estimated amount of the snow volume flux overestimated the observed ones below 4 m heights, especially during the drifting snow event (Fig. 4.8). However, the estimated vertical profiles indicated the observed feature of larger snow volume flux at lower levels clearly during the drifting snow event. Therefore, we decided that the 4-hour drifting snow event occurred from 9:00 to 13:00 and α is set to 4 because the observed snow volume flux was especially increased in the periods (Figs. 4.8b-e).

Figure 4.9 shows the averaged vertical profiles of the wind speed and the snow volume flux over the 4-hour drifting snow event in the observation. The friction velocity was estimated as $0.297\ \mathrm{m\,s^{-1}}$ with the least squares and Fig. 4.9a displays the logarithmic profile of the estimated wind with the friction velocity. The estimated wind profile almost corresponded to the observed values. The snow volume flux estimated by the friction velocity was still larger than the observed data at lower heights which was equivalent to the volume of 6×10^5 number of snow

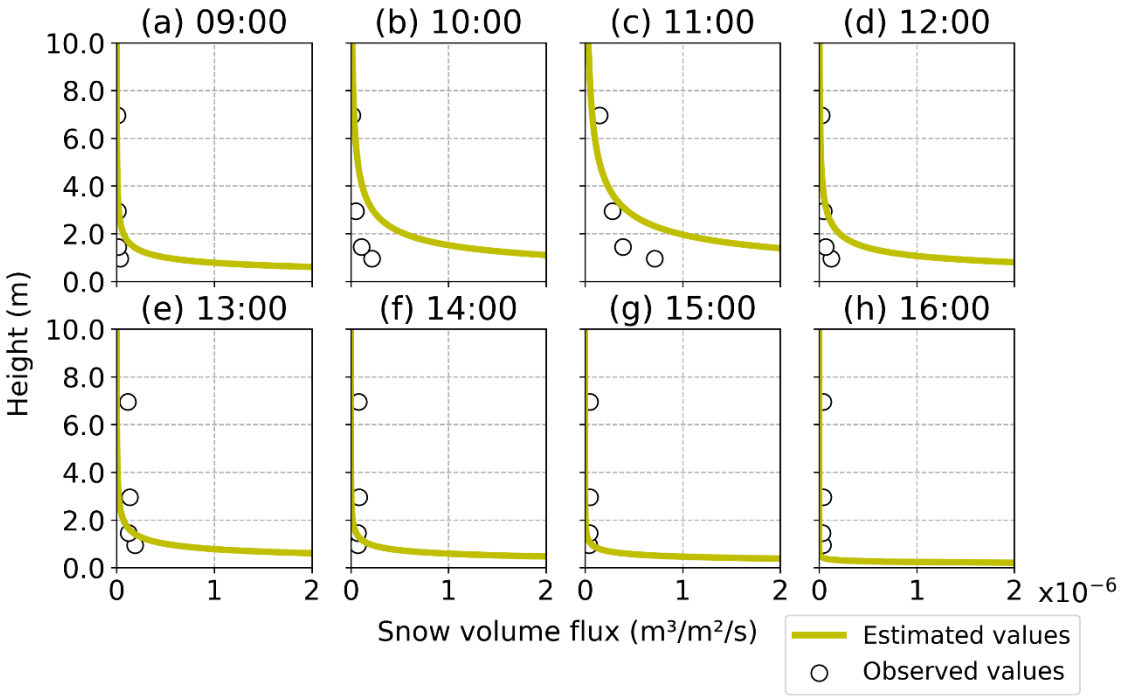

Fig. 4.8. Averaged snow volume flux profiles over every 1 hour from 9:00 JST to 16:00 JST. Yellow lines show the estimated values using Eq. (4.6) and (4.7) and the wind profiles in Fig. 4.7. Circles show the observed values.

particles at 1 m height. However, we considered that the estimated profile ranged in uncertainty in the observed data because the maximum of the observed snow volume flux was one or two orders larger than the averaged observation data, especially at 1 m height. We used these profiles as the western boundary condition in the CFD module and the amount of the inflow snow in the snow particles module.

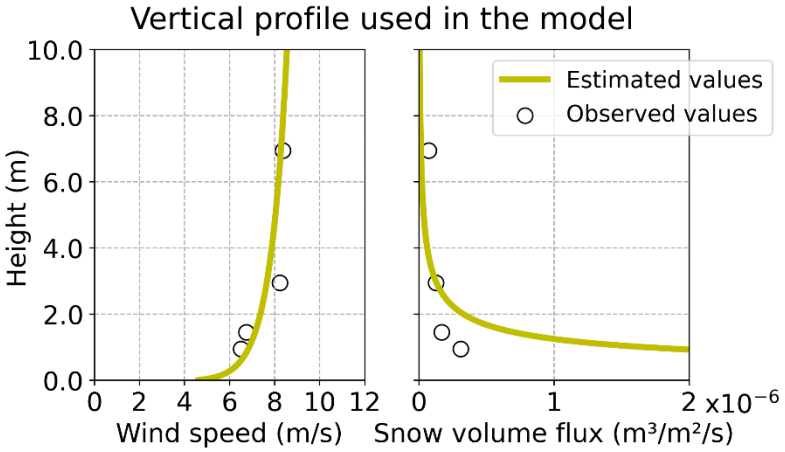

Fig. 4.9. Vertical profiles of the wind speed and the snow volume flux averaged over the drifting snow period. Yellow lines show the estimated profiles and circles show the observed values.

4.5.2. Control run

Figure 4.10 displays the snapshot of the wind profiles at the end of the calculation in the CFD module. The vertical wind profile had three obvious features which a stagnation area was formed around the front of the fence, the wind was intensified at the top of the fence, and the reverse flow was developed behind the fence from $x = 0$ m to $x = 5$ m (Fig. 4.10a). The reverse flow behind the fence was shown more clearly on the horizontal wind profile (Fig. 4.10b). The wind flow horizontally forks on the fence and there was a dipole pattern from $x = 0$ m to $x = 4$ m along $y = 5$ m and $y = 10$ m. These features of the vertical and horizontal wind profiles were consistent with the previous simulation studies (Han et al. 2021; Tanji et al. 2021).

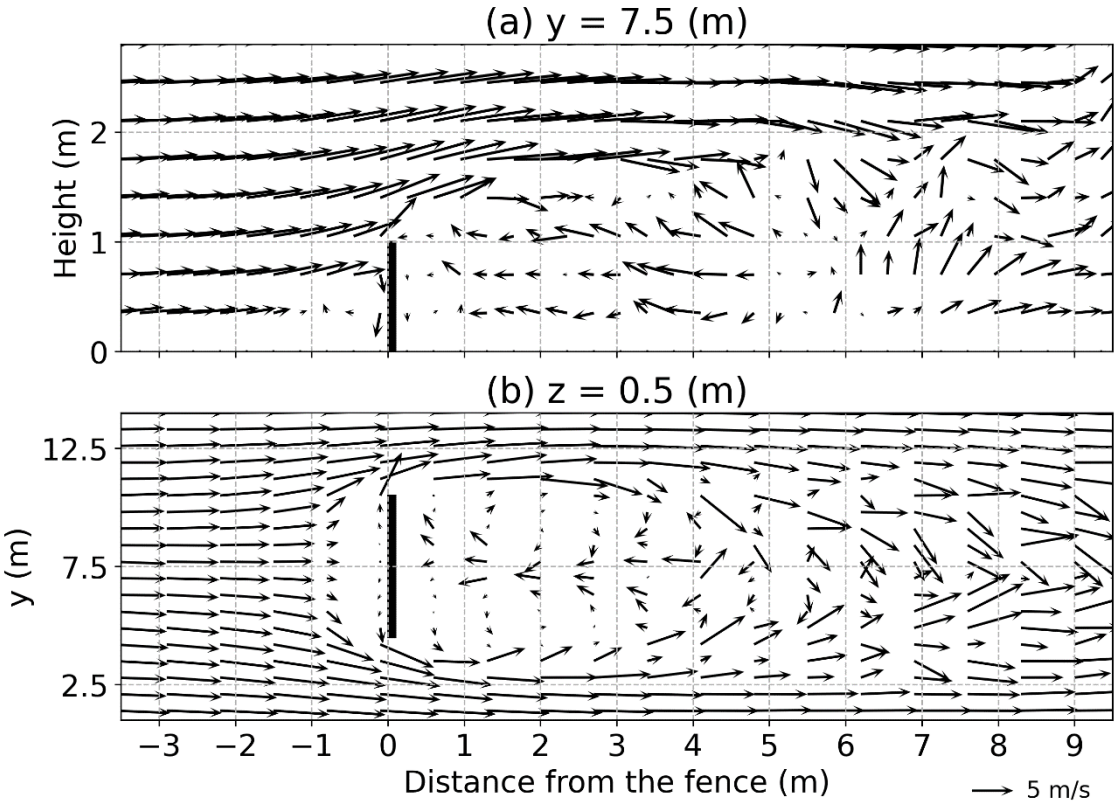

Fig. 4.10. Snapshots of the wind vectors (vectors) around the fence at the last segment in the cross-section along (a) $y = 7.5$ m and (b) $z = 0.5$ m. The solid lines at $x = 0$ show the fences.

Figure 4.11a shows the profile of the snowdrift distribution around the fence. The higher snowdrift was closer to the fence on the windward side, but the snowdrift just front of the fence had a low height. Compared with the observation, the snowdrift height estimated by the model agreed with the observed profile in the cross-section along the center of the fence (Fig. 4.11b), with a peak around $x = -1$ m and the peak height was about 0.35 m. This profile was also consistent with many previous simulation studies (Uematsu et al. 1991; Alhajraf 2004; Tanji et al. 2021) and the previous observation (Tabler 1994). This snowdrift formation was made by the weaker wind near the fence (Fig. 4.10a). About 0.3 m height snowdrifts could be seen on about from $x = -0.1$ m to $x = 0$ m only in the model and only observation had small snowdrift just behind of the fence around $x = 0.5$ m in Fig. 4.11b. We considered that there might be an unintended small gap between panel and the snow surface at the observation site. Some snow particles were blown to the leeward from the gap and accumulated just behind of the fence. This

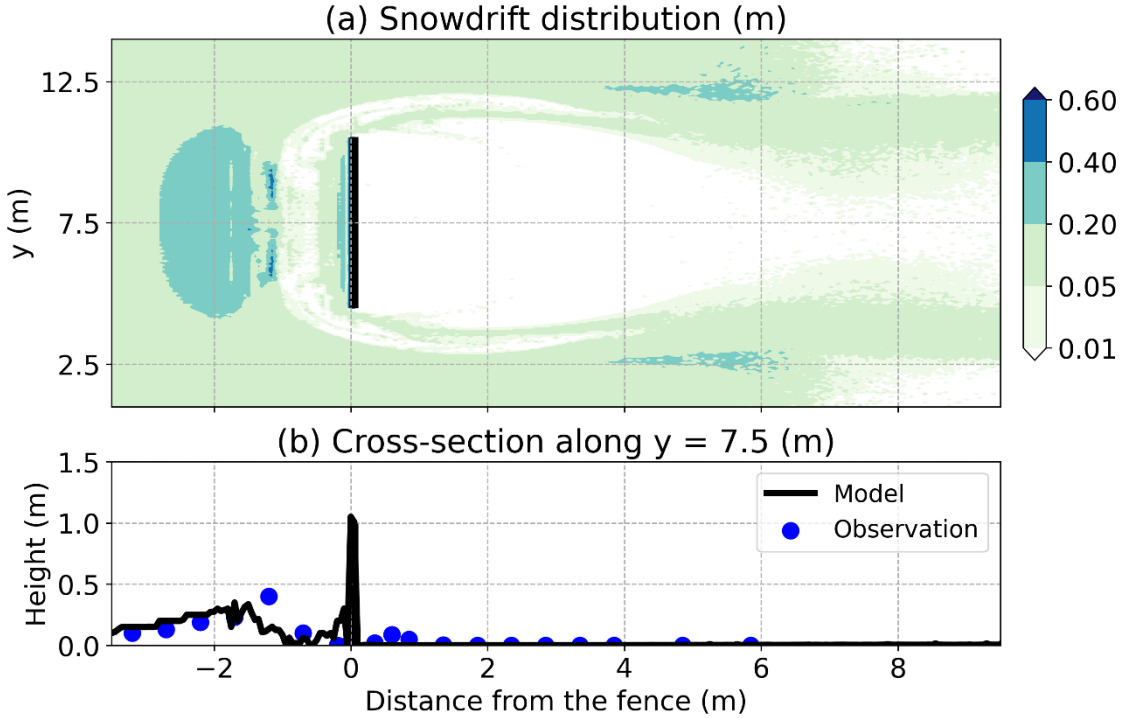

Fig. 4.11. (a) Snowdrift height distribution around the fence. (b) Snowdrift height in the cross-section along $y = 7.5$ m. The solid line shows the model result and the blue circles show the observed heights. Slid lines at $x = 0$ m in (a) and (b) show the fences.

gap could make the differences of the snowdrift height between simulation and observation around the $x = 0$ m.

The snowdrift distribution on the leeward side of the fence had the arc formations on the no-fence zone, but the snowdrift was not formed just behind the fence. These features were similar to that of the previous studies (Beyers et al. 2004; Okaze et al. 2013; Tanji et al 2021). The arc formations were made by snow particles following the split flow from the sides of the fence (Fig. 4.10b). Few snow particles on the flow could reach just behind the fence and almost no snowdrift was formed along the center of the fence on the leeward in both simulation and observation (Fig. 4.11b). The peak of the snowdrift on the leeward was $y = 12.5$ m and $y = 2.5$ m from $x = 4$ m to $x = 6$ m.

4.5.3. Sensitivity tests

4.5.3.1 Physical properties of snow particles

The result of the sensitivity test about the snow particles' density had a larger difference because the density of particles decided snow particles' weight and volume. Figure 4.12a displays the difference of the snowdrift height between the control result and the result with particles of a smaller density. It was clarified that particles of a smaller density were blown farther from the inflow boundary on both the windward and the leeward side of the fence. The snowdrift height from $x = -4$ m to $x = -1.8$ m on the cross-section along $y = 7.5$ m was lower than that in the control experiment because snow particles of a smaller density had lighter weight and were resuspended easily by the wind [Fig. 12c; Eq. (4.3)]. These blown snow particles made a higher snowdrift peak at closer position to the fence, which was about on $x = 1$ m (Fig. 12c). Snowdrift in the downstream of $x = 5$ m around the center of the fence was also considered to be formed by these blown particles on the windward. On the other hand, snow particles of a lager density

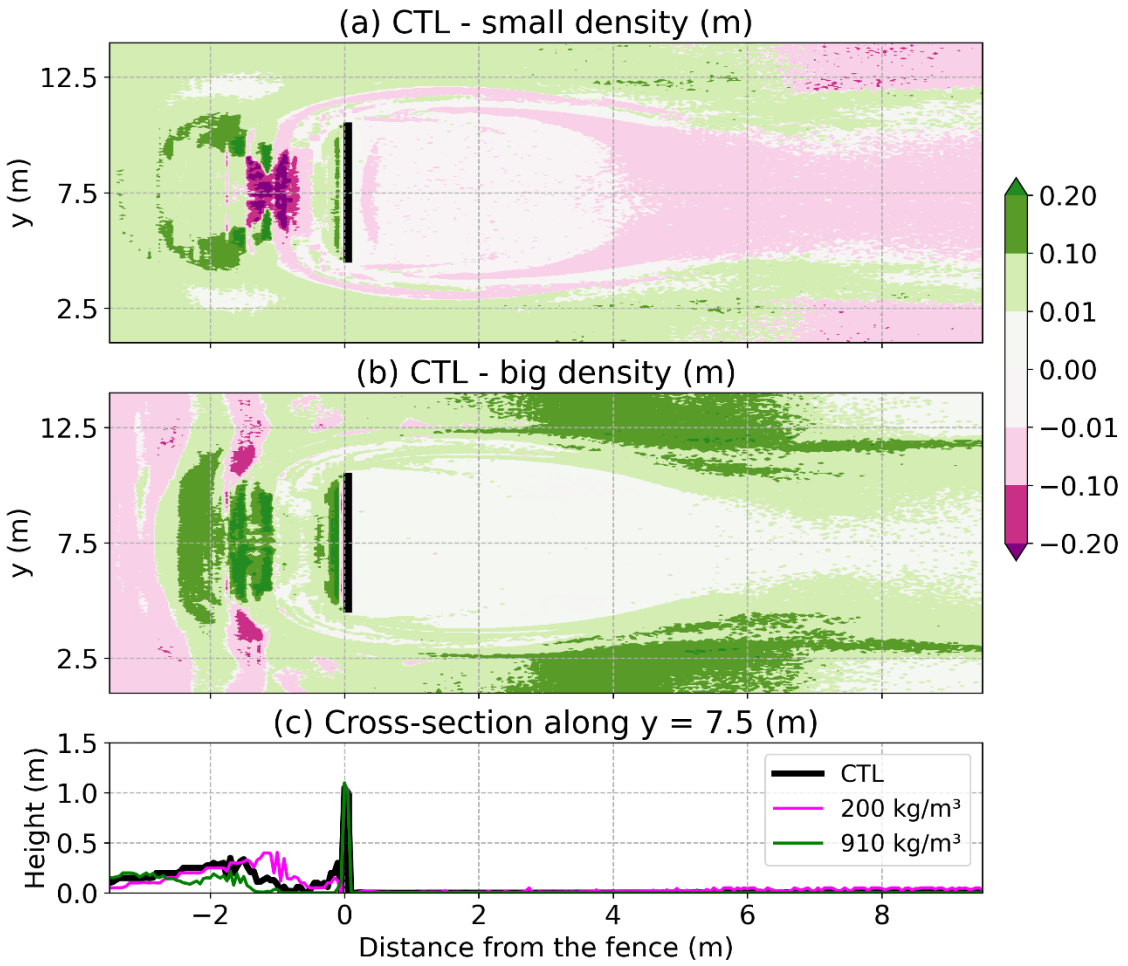

Fig. 4.12. The difference between the result of snowdrift height in the control experiment and in the experiment with snow particles of (a) small density and (b) big density. Green areas show the areas where snowdrift in the control experiment is higher than the other experiment. Pink areas show the opposite. (c) Snowdrift height in the cross-section along $y = 7.5$ m in the control experiment (a solid black line) and in the experiment with particles of small density (a pink line) and big density (a green line). Black solid lines in (a)-(c) show the fences.

fell immediately and formed the snowdrift around the inflow boundary due to its weight. These particles also were not blown by the wind easily. These particles' features made higher snowdrift than that in the control experiment from $x = -4$ m to $x = -3$ m (Fig. 4.12b). Few particles of larger density fell just on the front of the fence and the peak of the snowdrift height was not clear on the cross-section along $y = 7.5$ m (Fig. 4.12c). We considered that the snowdrift created by snow particles of a larger density was immature and growing in this experiment.

Figure 4.13 displays the result of the sensitivity test of the diameter of the particles. The experiment with a smaller diameter had a lower snowdrift height on the front of the fence because smaller particles were lifted by the turbulent wind more easily [Eq. (4.3); Fig. 4.13a]. This feature was obvious on the cross-section of $y = 7.5\,\mathrm{m}$ (Fig. 4.13c). Moreover, snow particles of a small diameter formed the snowdrift which had a peak far from the fence $x = -1.8\,\mathrm{m}$ (Fig.

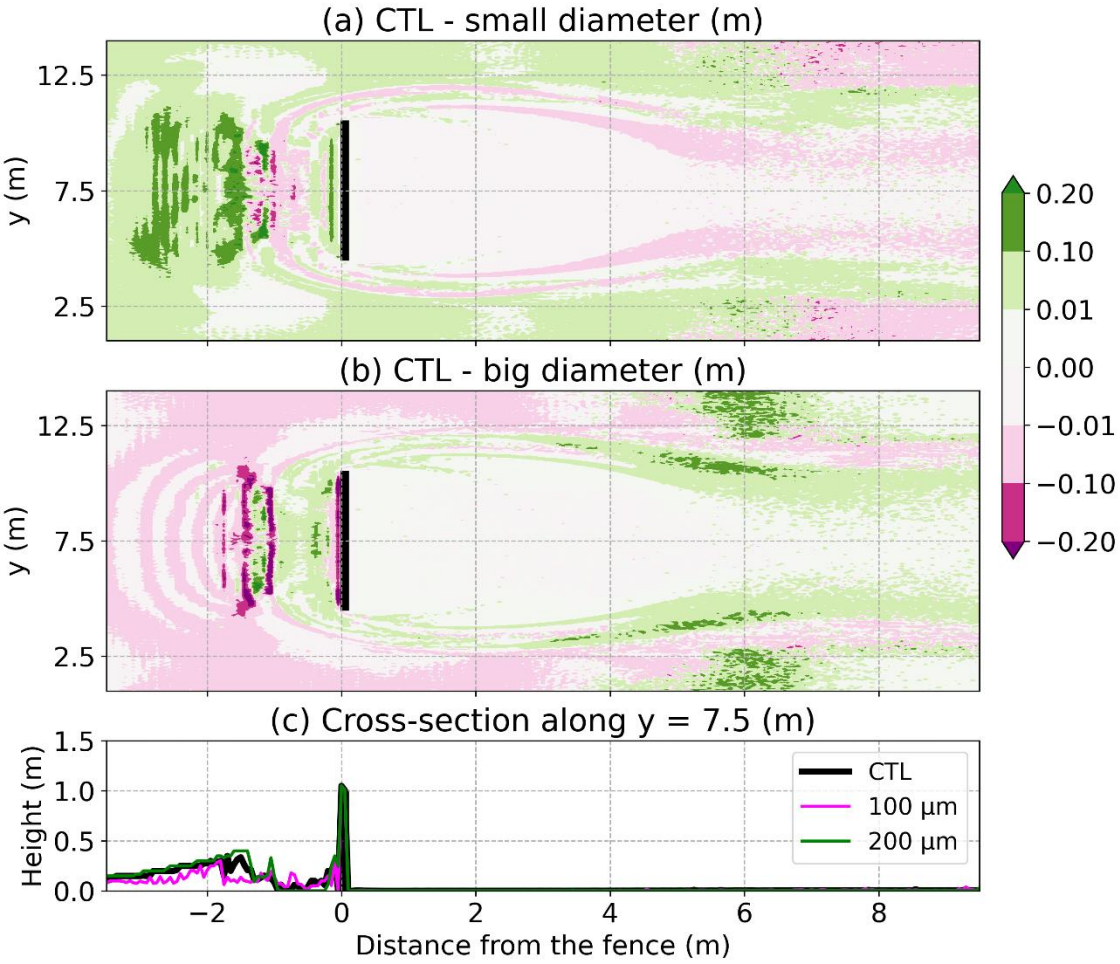

Fig. 4.13. The difference between the result of snowdrift height in the control experiment and in the experiment with snow particles of (a) small diameter and (b) big diameter. Green areas show the areas where snowdrift in the control experiment is higher than the other experiment. Pink areas show the opposite. (c) Snowdrift height in the cross-section along $y = 7.5\,\mathrm{m}$ in the control experiment (a solid black line) and in the experiment with particles of small diameter (a pink line) and big diameter (a green line). Black solid lines in (a)-(c) show the fences.

4.13c). In the experiment with the snow particles of a larger diameter, the snowdrift distribution had the opposite features to the experiment with a smaller diameter (Fig. 4.13b). Larger snow particles made the snowdrift of a higher peak, 0.4 m height, and its peak was closer to the fence $x = -1.5$ m (Fig. 4.13c). However, the difference between the result with larger particles and the control result was larger than that between the result with smaller particles and the control result because snowdrift height was dependent not only on the threshold friction velocity characterized by the physical property of the snow particles [Eq. (4.3)] but also on the wind profile determined by the fence height and fence position. Smaller particles also tended to reach and accumulate behind the fence from $x = 4$ m to $x = 6$ m and farther area from the windward compared with the control experiment in the downstream of $x = 7$ m. Snow particles of a smaller diameter accelerated more easily [Eq. (4.1)] and were blown following the reverse flow and the fork wind flow (Fig. 10b), which particles made these snowdrift distributions. This model reproduced the different features of the snowdrift distribution regarding densities and diameters of snow particles which were equivalent to ice particles and new snowfall particles.

4.5.3.2. Sub-processes of snow particles

Figure 4.14a displays the difference of the snowdrift height between the result of the control experiment and that of the no-resuspension experiment. The difference was particularly seen on the leeward side of the fence. There were two large difference areas around $x = 4.5$ m along $y = 4$ m and $y = 11$ m, because snowdrifts were trend to be formed on closer to the fence on the leeward without the resuspension process. These peaks were about twice higher than the peaks of the result of the control experiment (Fig. 4.14a). The result suggested that the resuspension process had an effect to blow snow particles farther away to the leeward. However, in the cross-section along $y = 7.5$ m, the snowdrift height had little difference between the

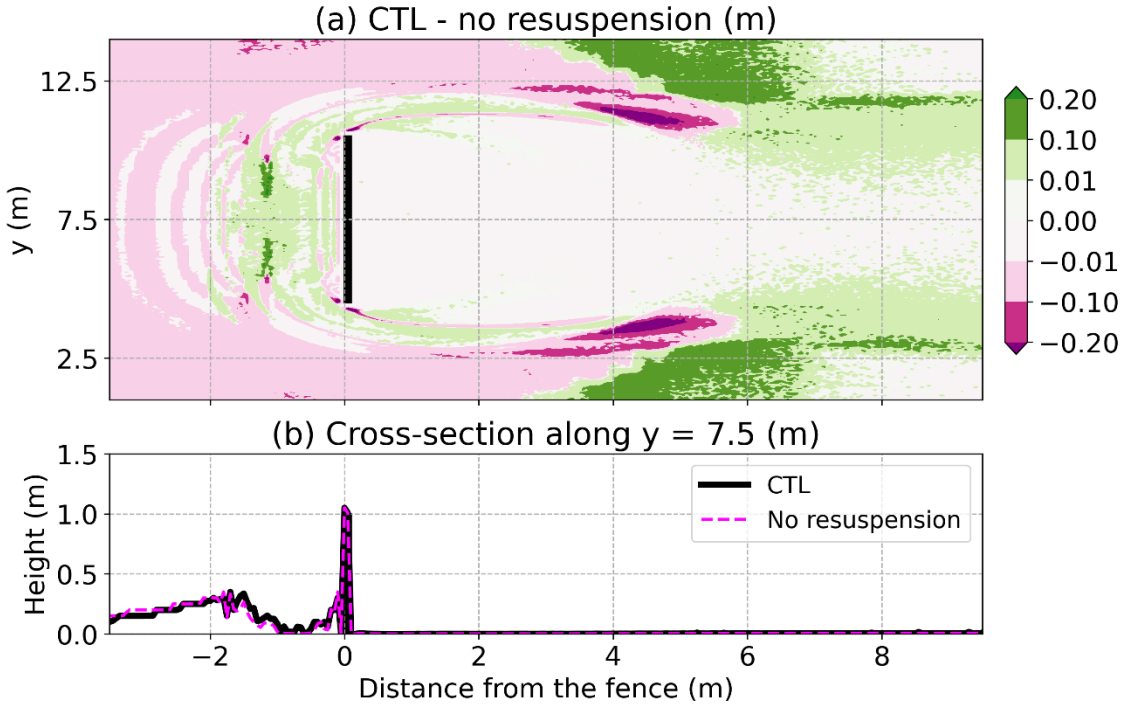

Fig. 4.14. (a) The difference between the result of snowdrift height in the control experiment and the no-resuspension experiment. Green areas show the areas where snowdrift in the control experiment is higher than that in the no-resuspension experiment. Pink areas show the opposite. (b) Snowdrift height in the cross-section along $y = 7.5$ m in the control experiment (a solid black line) and the no-resuspension experiment (a pink broken line). Black solid lines in (a) and (b) show the fences.

control experiment and the experiment without the resuspension process except for the peak position. The peak along it was 0.1 m closer to the fence in the control experiment than in the no-resuspension experiment (Fig. 4.14b). It was also suggested that the resuspension process did not contribute to the snowdrift just behind the fence because the snowdrift height there was so small both in the control experiment and in the experiment without the resuspension process (Fig. 4.11a).

The result of the snowdrift distribution in the experiment without the rebound process was even closer to that of the control experiment (Fig. 4.15). Small differences were shown around the fence and the leeside of the snowdrift, but almost all the area had under 0.1 m difference at

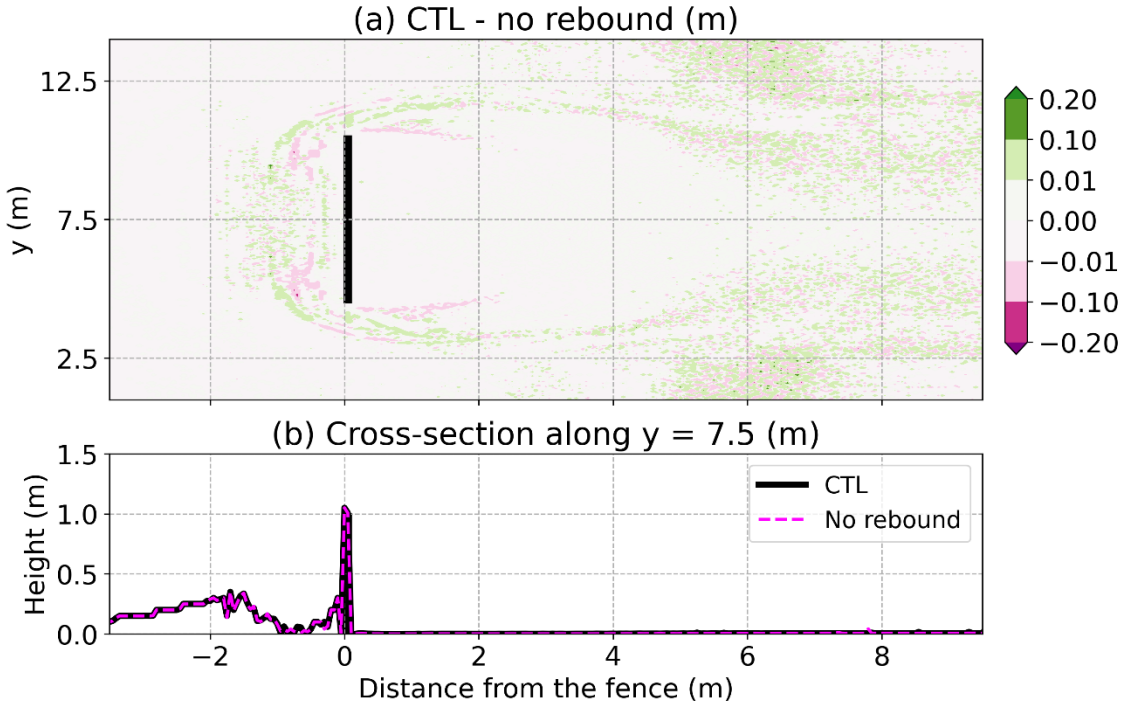

Fig. 4.15. (a) The difference between the result of snowdrift height in the control experiment and the no-rebound experiment. Green areas show the areas where snowdrift in the control experiment is higher than that in the no-rebound experiment. Pink areas show the opposite. (b) Snowdrift height in the cross-section along $y = 7.5$ m in the control experiment (a solid black line) and the no-rebound experiment (a pink broken line). Black solid lines show the fences.

most (Fig. 4.15a). The snowdrift height on the cross-section along $y = 7.5$ m was also just like the height of the control experiment (Fig. 4.15b). The contribution of the rebound process to the snowdrift distribution was small in the whole area.

4.6. Conclusions and discussion

We conducted sensitivity tests with the numerical simulation model of Tanji et al. (2021) in order to evaluate their contribution of the resuspension process, the rebound process, diameter, and density of drifting snow particles. Before the tests, we implemented the resuspension and the rebound process to the LBM snowdrift model developed by Tanji et al.

(2021). We used the observed vertical wind profile of the 4-hour drifting snow event in Teshikaga Town as the inflow boundary conditions in the model. The numerical simulation was conducted in a finite channel installed with a finite solid fence which was the same condition on the observation site. The control experiment was set to snow particles' diameter as $d = 150$ μm and density as $\rho_p = 450$ kg/m^3. The result of the snowdrift height simulated by the LBM snowdrift model corresponded to the observed snowdrift height along the center of the fence. It can be demonstrated that this model could reproduce the snowdrift distribution quantitively. In the sensitivity tests of the physical properties of the snow particles such as density and diameter, the physical properties influenced the snowdrift distribution both on the leeward and on the windward side of the fence because the physical properties decided the maximum height of the snowdrift and the drifting snow particles' motions. The sensitivity test of the sub-processes showed that the resuspension process contributed to the snowdrift distribution more largely than the rebound process, especially to the snowdrift on the leeward side of the fence.

These results in the sensitivity test suggested that using the proper parameter of the snow particles in the numerical model was a key to reproduce the equivalent snowdrift distribution to the observed distribution. For example, snow particles of a smaller diameter and smaller density tended to form the snowdrift not only on the windward but also on the leeward side of the fence, which properties were consistent with the new snowfall particles. The physical snowpack models such as SNOWPACK (Bartelt and Lehning 2002) and CROCUS (Brun et al. 1992) are powerful tools for accumulated snow particle conditions such as grain shape and density three-dimensionally using the meteorological data (Katsuyama et al. 2020). It is desired to use the estimated value of diameter and density by the physical snowpack model as the condition of snow particles in the numerical simulation models of the snowdrift.

Observation data was not enough to be implemented as the inflow boundary condition

in this chapter. For example, we did not directly use the observed amount of drifting snow particles as the boundary condition due to the insufficient vertical resolution above the snow surface. Instead, we used the estimated value by the observed wind data. Tanji et al. (2021) demonstrated that the inflow snow particles from under 1 m height above the surface are important to form the snowdrift around the 1 m-height fence. However, measuring snow volume flux just above the surface is difficult because the observation instruments might be buried in the snowdrift during the events. Even the trench method that measures the amount of snow particles on the tranches installed on the surface (Nishimura 2009) is not practical at the moment due to large costs. Hence, the estimation of the inflow snow particles in this chapter was a practical method as long as the wind logarithmic profile [Eq. (4.5)] is consistent with the condition.

We should compare the results of the snowdrift simulation with that of the observation not only on the windward but also on the leeward side of the fence to validate the model performance. The observed snowdrift height that we used in this study was 1-dimensional data measured by cutting the snowdrift along the center of the fence. This gauge observation crossing at the fence centre was not helpful to check whether the folk structure aside of the fence in the leeward was well simulated in the model. Recently, the photogrammetry and the Light Detection And Ranging (LiDAR) were attempted to measure the horizontal distribution of snowdrift heights. The photogrammetry mainly uses photos taken by the unmanned aerial vehicle (UAV). Niiya et al. (2021) took aerial images by the UAV before and after a drifting snow event and made a digital surface model of the snowdrift around a snow fence. The result of snowdrift height by this measurement was consistent with the result of the cross-sectional observation. The photogrammetry is a novel tool for observing the snowdrift though the UVA cannot fly under strong wind conditions and the image is not available at the night. LiDAR can mitigate these weak points of the photogrammetry because this method measures reflected light of near-infrared

radiation or ultraviolet radiation. LiDAR can also find the snowdrift growing during the drifting snow event. Okaze et al. (2022) showed that snowdrift distribution observed by LiDAR corresponded to the snowdrift observed by the photogrammetry. Ohara et al. (2022) compared the snowdrift model simulation with these observations. Our model could be validated by these methods. However, this point will be addressed in future work.

In this chapter, we only focus on the sensitivity of the sub-process and the physical properties of drifting snow particles, but the interaction between the wind profile and the snowdrift distribution also should be considered. Snowdrift formation influences the wind profile because matured snowdrifts are treated as obstacles for wind. Some studies implemented the momentum exchange between the wind and the particles into the numerical models (Zwaaftink et al. 2014), but no studies considered the wind flow variation influenced by the snowdrift distribution because the boundary condition of the snowdrift was complicated. However, the model in this chapter can resolve this problem because the LBM is simpler than other algorithms and more suitable for complicated boundary conditions, such as not only around snow fences but also snowdrifts. However, this point also will be addressed in future work.

The sensitivity of the variability of the physical properties of snow particles is an also interesting topic. In the sensitivity tests in this chapter, physical properties of particles such as diameter and density are set to constant values, but in reality, the values of properties can be shown as the distribution function and drifting snow particles might be mixed with different physical properties. For example, the diameter distribution of the drifting snow particles was reported to be well-fitted to the gamma distribution (Schmidt 1982; Nemoto and Nishimura 2004; Nishimura et al. 2014). The physical properties of drifting snow particles should be given not as the constant value but as the distribution function in order to estimate more accurate snowdrift distribution.

This study displayed that the snowdrift distribution simulated by the LBM snowdrift model quantitively corresponded well to the observed one when imposed properties of snow particles were proper. Therefore, this model can be applied to resolving many problems regarding snowdrifts around roads. Snow fences were installed on the side of the roads in order to protect the roads from snowdrifts on the leeward. However, no one knows what structures of snow fences are the most optimal not for developing snowdrifts on roads. The LBM snowdrift model is suitable for researching the structure with many experiments because the model has high efficiency in parallel computation. Snowdrift formed around the lateral gap between the snow fences are also serious problems on road administration because the gap must be made around the intersections. Snowdrifts around the various structure of the road can be estimated in this model. This model also can be applied to the estimation of visibility due to drifting snow on roads, which is the main cause of the traffic disruption in the snowy area. Visibility due to drifting snow is related amount of snow-drift flux (Budd et al. 1966; Takeuchi and Fukuzawa 1976; Matsuzawa and Takeuchi 2002). Transport amount of drifting snow can be calculated explicitly in this model through tracing drifting snow particles.

In the mountainous area, redistribution of snow particles by drifting snow plays an important role in the avalanche potential, but previous studies did not calculate the redistribution explicitly (Bartelt and Lehning 2002; Brun et al. 1992). The boundary conditions and snowdrift distribution in mountainous areas are more complicated than around a snow fence but the LBM can calculate the turbulent flow there due to its suitability for complicated boundary conditions. Tracing drifting snow particles is also helpful for the estimation of the avalanche potential because the potential is strongly associated with the condition of the snowpack layers. The snowpack layer due to drifting snow particles has different features from that due to snowfall particles because the shape of particles is different. Therefore, the model in this chapter has the potential to resolve

problems brought on the drifting snow in the mountainous area.

Chapter 5. General Summary

In Chapter 2, we estimated snow concentration and visibility under blowing snow events around Sapporo, Hokkaido with the dynamical downscaled meteorological data of 1-km resolution. This chapter showed that time-series of snow concentration and visibility could be well reproduced with the down-scaled data but the original data of 5-km resolution did not. This is because the wind at 10-m height reproduced sudden and local wind strengthening with 1-km resolution data. This part concluded that wind speed was required with a higher resolution such as 1-km resolution for the diagnosis of blowing snow development. However, only two cases of blowing snow events were estimated around Sapporo in this chapter. Inatsu et al. (2020) analyzed visibility around Ishikari plane in the 2017/2018 winter with the same method as this chapter and examined three typical blowing snow events with different synoptic situations. This study demonstrated that the down-scaled output was more useful than the data of 5-km resolution on Ishikari plane for the case which involved westerly or north-westerly wind advected multiple heavy-snow streaks from the Sea of Japan. Tanji et al. (2021) also expanded this study to research the area where blowing snow events frequently developed in the 2017/2018 winter all over Hokkaido. This study also examined the synoptic situations which brought blowing snow events using a self-organizing map (Kohonen 1995; Kawazoe et al. 2020). These studies showed that down-scaled meteorological data well estimated blowing snow potential for several blowing snow events.

In Chapter 3 and 4, we developed a numerical model for simulating snowdrifts around obstacles. The model was consisted of the conventional fluid dynamics module with the lattice Boltzmann method (LBM) and the snow particles module with the conventional methods. This model could simulate the snowdrifts around the solid fences. The simulated snowdrifts

corresponded to that of observation in the term of the peak position and peak height of the snowdrift on the windward side of the fence. These results were brought by reproducing the wind flow profile around the fences estimated with the LBM. The model could also simulate snow particle trajectories in the drifting snow. Drifting snow particles flowing from a lower height contributed to the snowdrift formation. The sensitivity test of sub-processes and physical properties of snow particles revealed that the physical properties influenced snowdrift shape and height, and the potential of snowdrift formation. Therefore, we should use proper values of snow particle properties to simulate snowdrift around obstacles.

Snow surface condition is a key word in the synthesis of this thesis. New snow particles just after reaching the surface are easily detached from it, but they combine with snowpack immediately under wet conditions or otherwise sintering in the timescales. However, the study in the former part diagnosed the snow surface condition only by surface air temperature. This simple diagnosis method brought overestimates of blowing snow events. The study in the latter part also assumed that the windward of the calculation domain always had drifting snow potential and infinite drifting snow particles flowed in the domain. In addition, this study elucidated that the physical properties of snow particles play an important role on the snowdrift distribution in the latter part. The physical snowpack models such as SNOWPACK (Bartelt and Lehning 2002) and CROCUS (Brun et al. 1992) can resolve these problems. The physical snowpack models can calculate the condition of the snow surface such as grain shape and density using the meteorological data. Combining the physical snowpack models with the studies in this thesis will be able to estimate blowing snow potential and snowdrift distribution more accurately. However, this point will be retained as a future work.

The products in two study parts in this thesis and the physical snowpack model can be combined (Fig. 5.1). The diagnosis method in the former part estimates background conditions

with a 1-km resolution, such as wind speed, and transport amount of blowing and drifting snow particles around the surface. The results can use in the conventional physical snowpack model and the LBM snowdrift model as the boundary conditions. The physical snowpack model calculates the condition and physical properties of the snow particles on the surface and the LBM snowdrift model calculates snowdrift distribution. This combination assumes that micro-scale snowdrifts can be estimated by the meso-scale meteorological data. In addition, the snowdrift results such as snow cover distribution calculated by the LBM snowdrift model can feedback to the snowpack model. The influence of the redistribution of snow particles due to drifting and blowing snow is more remarkable on the mountain where the snow accumulation is formed patchily due to the complicated turbulent flow around the surface. We considered the blowing and drifting snow mainly around the road but the studies in this thesis will give impacts on not only the traffic engineering but also the earth science in the feature.

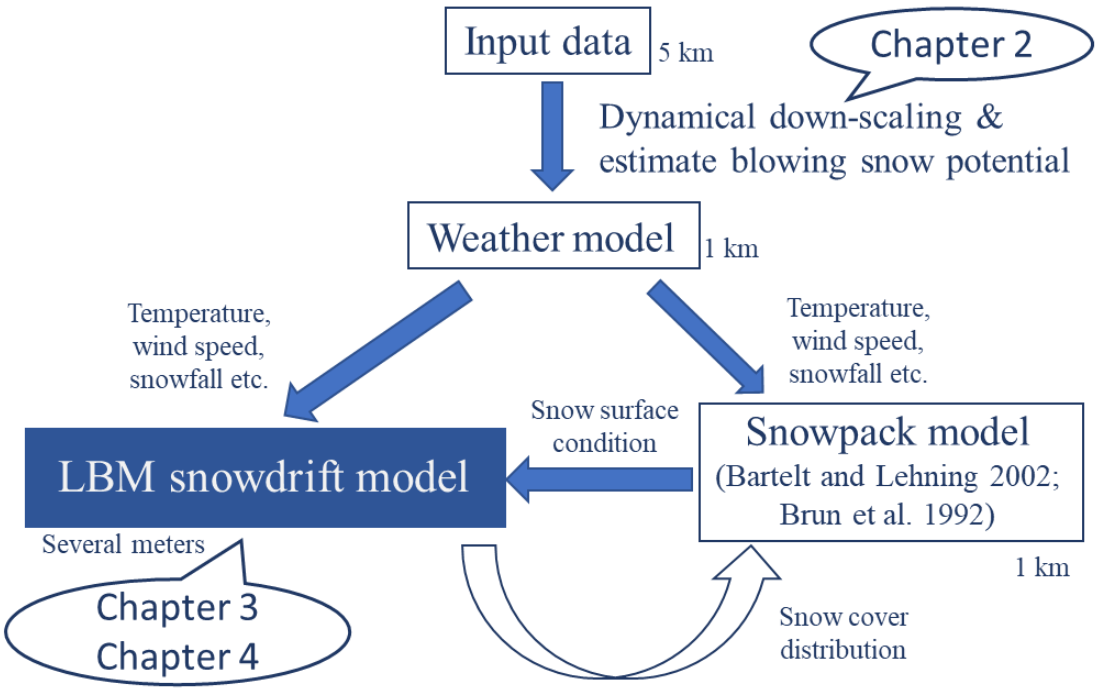

Fig. 5.1. Schematic of the interaction between three models, a weather model, a snowpack model and the LBM snowdrift model.

Acknowledgments

This work was supported by JST SPRING, Grant Number JPMJSP2119. The meteorological observation data were provided by the JMA, by Hokkaido Regional Development Bureau, and by East Nippon Expressway Company Ltd. Scalable Computing for Advanced Library and Environment (SCALE) was developed by RIKEN Center for Computational Science. This work was partly achieved through the use of the supercomputer system at the information initiative center, Hokkaido University, Sapporo, Japan. The observed data of wind speed, amount of drifting snow particles, and snowdrift distribution at Teshikaga town was provided by Dr. Yusuke Harada, Dr. Satoshi Ohmiya of Civil Engineering Research Institute for Cold Region, and Dr. Tsubasa Okaze of Tokyo Institute of Technology.

I would like to express my gratitude thanks to Prof. Masaru Inatsu, who is the chief referee of my doctoral thesis, for supporting this study and suggesting valuable comments and discussions. I also deeply thank all associate referees, Prof. Shosihro Minobe, Dr. Yoshinori Sasaki, Dr. Yosuke Sato, and Dr. Tsubasa Okaze. I would like to thank Dr. Satoshi Ohmiya, Dr. Yusuke Harada, Prof. Kouichi Nishimura, Mr. Naoki Matsuoka, Dr. Masaki Nemoto, Dr. Masaru Matsuzawa, Dr. Hirofumi Niiya, and Dr. Yuta Katsuyama for giving me many suggestions for my work about drifting snow. I thank Prof. Tsutomu Watanabe and Seiya Nishizawa for giving me many suggestions for my work about the Lattice Boltzmann method and SCALE, respectively. I also thank Dr. Sho Kawazoe and Dr. Takumi Honda for giving me insightful comments to this work. I thank Ms. Fumiko Yoshioka and Ms. Atsuko Kobayashi for supporting office procedures and thank the other laboratory members for giving me great time. Finally, I really thank my parents for encouraging me to continue to a doctoral course and be a researcher.

References

Akhtar M, Ahmad N, Booij MJ (2008) The impact of climate change on the water resources of Hindukush–Karakorum–Himalaya region under different glacier coverage scenarios. J. Hydrol., 355:148–163. doi: 10.1016/j.jhydrol.2008.03.015.

Ammi M, Oger L, Beladjine D, Valance A (2009) Three-dimensional analysis of the collision process of a bead on a granular packing. Phys. Rev., E, 79:021305. doi:10.1103/PhysRevE.79.021305.

Alhajraf S (2004) Computational fluid dynamic modeling of drifting particles at porous fences. Env. Modelling & Software, 19:163–170. doi:10.1016/S1364–8152(03)00118-X.

Bagnold RA (1941) The physics of blown sand and desert dunes. Methuen, London

Bartelt P, Lehning M (2002) A physical SNOWPACK model for the Swiss avalanche warning. Part I. numericalmodel. Cold Reg. Sci. Techl., 35:3:123-145. doi:10.1016/s0165-232x(02)00074-5.

Benzi R, Succi S, Vergassola M (1992) The Lattice Boltzmann equation: theory and applications. Phys. Rep., 222:145–197. doi:10.1016/0370-1573(92)90090-M.

Bernasch M, Fatica M, Melchionna S, Succi S, Kaxiras E (2009) A flexible high-performance Lattice Boltzmann GPU code for the simulations of fluid flows in complex geometries. Concurrency and Computation: Practice and Experience, 22:1–14. doi:10.1002/cpe.1466.

Bernhardt M, Liston GE, Strasser U, Zängl G, Schulz K (2010) High resolution modelling of snow transport in complex terrain using downscaled MM5 wind fields. The Cryosphere, 4:99–113. doi: 10.5194/tc-4-99-2010.

Beyers JHM, Sundsbo PA, Harms TM (2004) Numerical simulation of three-dimensional, transient snow drifting around a cube. J. Wind Eng. Ind. Aerodyn., 92:725–747. doi:10.1016/j.jweia.2004.03.011.

Brown AR, Derbyshire SH, Mason PJ (1994) Large-eddy simulation of stable atmospheric boundary layers with a revised stochastic subgrid model. Quarterly J. Royal Meteor. Soc., 120:1485–1512. doi: 10.1256/smsqj.52003.

Brun E, David P, Sudul M Brunot G (1992) A numerical-model to simulate snow-cover stratigraphy for operational avalanche forecasting. J. Glaciol., 38:128:13-22. doi:10.3198/1992JoG38-128-13-22.

Budd WF, Dingle R, Radok U (1966) The Byrd Snow Drift Project: Outline and Basic Results. Studies in Antarctic Meteorology. Antarctic Research Series, 9:71–134. doi: 10.1029/AR009p0071.

Cayan DR, Maurer EP, Dettinger MD, Tyree M, Hayhoe K (2008) Climate change scenarios for the California region. Climatic Change, 87:21–42. doi: 10.1007/s10584-007-9377-6.

Chen H, Chen S, Matthaeus WH (1992) Recovery of the Navier Stokes equations using a lattice-gas Boltzmann method. Phys. Rev., A45:5339–5342. doi:10.1103/PhysRevA.45.R5339.

Chen S, Doolen GD (1998) Lattice Boltzmann method for fluid flows. Annu. Rev. Fluid Mech., 30:329–364. doi:10.1146/annurev.fluid.30.1.329.

Clifton A, Rüedi JD, Lehning M (2006) Snow saltation threshold measurements in a drifting snow wind tunnel. J. Glaciol., 39:585–596. doi:10.3189/172756506781828430.

Deiterding R, Wood SL (2016) Predictive wind turbine simulation with an adaptive lattice Boltzmann method for moving boundaries. J. Phys. Conf. Ser., 753:082005.

doi:10.1088/1742-6596/753/8/082005.

Delpech P, Palier P, Gandemer J (1998) Snowdrifting simulation around Antarctic buildings. J. Wind Eng. Ind. Aerod., 74–76:567–576. doi:10.1016/S0167-6105(98)00051-8.

Durand Y, Giraud G, Brun E, Merindol L, Martin E (1999) A computer-based system simulating snowpack structures as a tool for regional avalanche forecasting. J. Glaciol., 45:469–484. doi: 10.3189/S0022143000001337.

Durand Y, Guyomarc'h G, Merindol L, Corripio JG (2005) Improvement of a numerical snow drift model and field validation. Cold Reg. Sci. and Tech., 43:93–103. doi: 10.1016/j.coldregions.2005.05.008.

Elghobashi S (1994) On predicting particle-laden turbulent flows. Appl. Sci. Res., 52:309–329. doi:10.1007/BF00936835.

Feng YT, Han K, Owen DRJ (2007) Coupled lattice Boltzmann method and discrete element modelling of particle transport in turbulent fluid flows: Computational issues. Int. J. Numer. Meth. Engng., 72:1111–1134. doi:10.1002/nme.2114.

Geier M, Greiner A, Korvink JG (2009) A factorized central moment lattice Boltzmann method. Eur. Phys. J. Spec. Top., 171(1): 55–61. doi: 10.1140/epjst/e2009-01011-1.

Geier M, Schönherr M, Pasquali A, Krafczyk M (2015) The cumulant lattice Boltzmann equation in three dimensions: theory and validation. Comp. Math. Appl., 70(4): 507–547. doi: 10.1016/j.camwa.2015.05.001.

Han M, Ooka R, Kikumoto H (2019) Lattice Boltzmann method-based large-eddy simulation of indoor isothermal airflow. Int. J. Heat Mass Transf., 130:700–709. doi: 10.1016/j.ijheatmasstransfer.2018.10.137.

Han M, Ooka R, Kikumoto H (2021) Effects of wall function model in lattice Boltzmann method-based large-eddy simulation on built environment flows. Build. and Env., 195: 107764. doi:10.1016/j.buildenv.2021.107764.

Hecht M, Harting J (2010) Implementation of on-site velocity boundary conditions for D3Q19 lattice Boltzmann simulations. J. Stat. Mech., P01018. doi: 10.1088/1742-5468/2010/01/P01018.

Inagaki A, Kanda M, Ahmad HN, Yagi A, Onodera N, Aoki T (2017) A numerical study of turbulence statistics and the structure of a spatially-developing boundary layer over a realistic urban geometry. Bound.-Layer Meteor., 164:1651–181. doi:10.1007/s10546-017-0249-y.

Inatsu M, Tanji S, Sato Y (2020) Toward predicting expressway closures due to blowing snow events. Cold Reg. Sci. Tech., 177:103123. doi: doi.org/10.1016/j.coldregions.2020.103123.

Iversen JD (1981) Comparison of wind-tunnel model and full-scale snow fence drifts. J. Wind Eng. Ind. Aerod., 8:3:231–249. doi: 10.1016/0167-6105(81)90023-4.

Kaneko M, Matsuzawa M, Watanabe T (2011) Experiments on snowdrift development and vehicle starting limit. Technical research presentation 2011, 4pp. (in Japanese)

Katsuyama Y, Inatsu M, Nakamura K, Matoba S (2017) Global warming response of snowpack at mountain range in northern Japan estimated using multiple dynamically downscaled data. Cold Reg. Sci. Tech., 136:62–71. doi: 10.1016/j.coldregions.2017.01.006.

Katsuyama Y, Inatsu M, Shirakawa T (2020) Response of snowpack to +2℃ global warming in Hokkaido. Japan. J. Glaciol., 66:255:83–96, doi:10.1017/jog.2019.85.

Kawazoe S, Fujita M, Sugimoto S, Okada Y, Watanabe S (2020) Projected changes of extremely cool summer days over northeastern Japan simulated by 20 km-mesh large ensemble experiment. J. Meteor. Soc. Japan, 98: 1305–1319, doi:10.2151/jmsj.2020-067.

King MF, Khan A, Delbosc N, Gough HL, Halios C, Barlow JF, Noakes CJ (2017) Modelling urban airflow and natural ventilation using a GPU-based lattice-Boltzmann method. Buld. and Env., 125:273–284. doi:10.1016/j.buildenv.2017.08.048.

Klein M, Sadiki A, Janicka J (2003) A digital filter based generation of inflow data for spatially developing direct numerical or large eddy simulations. J. Comput. Phys., 186:652–665. doi:10.1016/S0021-9991(03)00090-1.

Kohonen T (1995) Self-Organizing Maps. Springer Series in Information Sciences, Vol. 30, Springer-Verlag, 362 pp.

Kusaka H, Kondo H, Kikegawa Y, Kimura F (2001) A simple single-layer urban canopy model for atmospheric models: comparison with multi-layer and slab models. Bound.-Layer Meteor., 101:329–358. doi: 10.1023/A:1019207923078.

Lehning M, Volksch I, Gustafsson D, Nguyen TA, Stahli M, Zappa M (2006): ALPINE3D: A detailed model of mountain surface processes and its application to snow hydrology. Hydrol. Proc., 20:2111−2128. doi:10.1002/hyp.6204.

Lehning M, Löwe H, Ryser M, Raderschall N (2008) Inhomogeneous precipitation distribution and snow transport in steep terrain. Water Resour. Res. 44:W07404. doi:10.1029/2007WR006545.

Lilly DK (1962) On the numerical simulation of buoyant convection. Tellus, 14:148–171. doi: 10.1111/j.2153-3490.1962.tb00128.x.

Liston GE, Brown RL, Dent JD (1993) A two-dimensional computational model of turbulent atmospheric surface flows with drifting snow. Ann. Glaciol., 18:281–286. doi:10.3189/S0260305500011654.

Liu D, Li Y, Wang B, Hu P, Zhang J (2016) Mechanism and effects of Snow accumulations and controls by lightweight snow fences. J. Mod. Transport, 24:261–269. doi:10.1007/s40534-016-0115-5.

Liu H, Kang Q, Leonardi CR, Schmieschek S, Narváez A, Jones BD, Williams JR, Valocchi AJ, Harting J (2016) Multiphase lattice Boltzmann simulations for porous media applications. Comput. Geosci., 20:777–805. doi:10.1007/s10596-015-9542-3.

Lu GP, DePaolo DJ, Kang QJ, Zhang DX (2009) Lattice Boltzmann simulation of snow crystal growth in clouds. J. Geophys. Res., 114: D07305. doi:10.1029/2008JD011087.

Maeno N (1982) Fubuki no Hassei Kikou to Yuki no Ryudoka. Kagaku, Iwanami Shoten., 52:34–41. (in Japanese)

Matsuo T, Sasyo Y (1981) Melting of snowflakes below freezing level in the atmosphere. J. Meteor. Soc. of Japan, 59:10–25. doi: 10.2151/jmsj1965.59.1_10.

Matsuzawa M, Takeuchi M (2002) A study of methods to estimate visibility based on weather conditions. Seppyo, 64:77−85. doi: 10.5331/SEPPYO.64.77. (in Japanese)

Matsuzawa M, Takechi H, Omiya S, Kokubu T, Harada Y (2014) A study on the improvement of the snowstorm visibility estimation method - Sensitivity analysis of the model of Matsuzawa and Takeuchi (2002). Proceedings of the 30th Cold Region Technology Conference, 69–73. (in Japanese)

McNamara GR, Zanetti G (1988) Use of the Boltzmann equation to simulate lattice-gas automata.

Phys. Rev. Lett., 61:2332–2335. doi:10.1103/PhysRevLett.61.2332.

Mellor GL, Yamada T (1982) Development of a turbulence closure model for geophysical fluid problems. Rev. of Geophysics and Space Physics, 20:851–875. doi: 10.1029/RG020i004p00851.

Mott R, Schirmer M, Bavay M, Grünewald T, Lehning M (2010) Understanding snow-transport processes shaping the mountain snow-cover. Cryosphere, 4:545–559. doi:10.5194/tc-4-545-2010.

Nakanishi M, Niino H (2004) An improved Mellor-Yamada level-3 model with condensation physics: Its design and verification. Bound.-Layer Meteor., 112:1–31. doi: 10.1023/B:BOUN.0000020164.04146.98.

Nemoto M, Nishimura K (2004) Numerical simulation of snow saltation and suspension in a turbulent boundary layer. J. Geophys. Res., 109:D18206. doi:10.1029/2004JD004657.

Nijssen B, O'Donnell GM, Hamlet AF, Lettenmaier DP (2001) Hydrologic sensitivity of global river to climate change. Climatic Change, 50:143–175. doi: 10.1023/A:1010616428763.

Niiya H, Nishimura K (2022) Hysteresis and Surface Shear Stresses During Snow-Particle Aeolian Transportation. Bound.-Layer Meteor., 183:447–467. doi: s10546-022-00688-8.

Niiya H, Omiya S, Sunako S, Nishimura K, Okaze T (2021) Snowdrift Observation around Fence by UAV-SfM Photogrammetry. JSSI & JSSE Joint Conference 2021 in Online. (in Japanese)

Nishimura K (2009) Measurement of Blowing Snow. Nagare, 28:455–460. (in Japanese)

Nishimura K, Hunt JCR (2000) Saltation and incipient suspension above a flat particle bed below

a turbulent boundary layer. J. Fluid Mech., 417:77–102. doi:10.1017/S0022112000001014.

Nishimura K, Nemoto M (2005) Blowing Snow at Mizuho Station, Antarctica. Phil. Trans. R. Soc., A:363:1647-1662. doi: 10.1098/rsta.2005.1599.

Nishimura K, Yokoyama C, Ito Y, Nemoto M, Naaim-Bouvet F, Bellot H, Fujita K (2014) Snow particle speeds in drifting snow. J. Geophys. Res., 119:9901–9913. doi:10.1002/2014JD021686.

Nishio F, Ishida T (1973) Rate of Turbulent Energy Dissipation During Snow Drifting. Low Temp. Sci. Series A, Phys. Sci., 31:69–85. (in Japanese)

Nishizawa S, Yashiro H, Sato Y, Miyamoto Y, Tomita H (2015) Influence of grid aspect ratio on planetary boundary layer turbulence in large-eddy simulations. Geoscientific Model Develop., 8:3393–3419. doi: 10.5194/gmd-8-3393-2015.

Noh HM (2019) Numerical analysis of aerodynamic noise from pantograph in high-speed trains using lattice Boltzmann method. Adv. Mech. Eng., 11(7):1–12. doi:10.1177/1687814019863995.

Ohara N, He S, Parsekian AD, Jones BM, Rangel RC, Nichols IO, Hinkel KM (2022) Spatial snowdrift modelling for an open natural terrain using a physically-based linear particle distribution equation. Hydrol. Processes, 36. doi: 10.1002/hyp.14468.

Okaze T, Kikumoto H, Ono H, Imano M, Ikegaya N, Hasama T, Nakao K, Kishida T, Tabata Y, Nakajima K, Yoshie R, Tominaga Y (2021) Large-eddy simulation of flow around an isolated building: A step-by-step analysis of influencing factors on turbulent statistics. Build. and Env. doi:10.1016/j.buildenv.2021.108021.

Okaze T, Mochida A (2017) Cholesky decomposition–based generation of artificial inflow turbulence including scalar fluctuation. Comput. Fluids., 159:23–32. doi:10.1016/j.compfluid.2017.09.005.

Okaze T, Mochida A (2018) Generation of artificial Inflow turbulence with digital filter method for LES within built-up environment. 25th Symposium of Wind Eng., 211–216. (in Japanese)

Okaze T, Mochida A, Tominaga Y, Nemoto M, Sato T, Sasaki Y, Ichinohe K (2012) Wind tunnel investigation of drifting snow development in a boundary layer. J. Wind Eng. Ind. Aerod., 104–106:532–539. doi:10.1016/j.jweia.2012.04.002.

Okaze T, Niiya H, Nishimura K (2018) Development of a large-eddy simulation coupled with Lagrangian snow transport model. J. Wind Eng. Ind. Aerod. 183:35–43. doi:10.1016/j.jweia.2018.09.027.

Okaze T, Niiya H, Omiya S, Sunako S, Nishimura K (2019) Observation of snowdrift around two-dimensional fence during a drifting snow event. JSSI & JSSE Joint Conference 2019 in Yamagata, 110. (in Japanese)

Okaze T, Niiya H, Omiya S, Sunako S, Kawashima R, Tanji S, Nishimura K (2022) Measurement of Snowdrift around a Fence with LiDAR for In-vehicle Use. JSSI & JSSE Joint Conference 2022 in Sapporo. (in Japanese)

Okaze T, Tominaga Y, Mochida A (2013) Development of new snowdrift model based on two transport equations of drifting snow density, numerical prediction of snowdrift around buildings using CFD (Part 2). J. Environ. Eng., AIJ 78:149–156. doi: 10.3130/aije.78.149. (in Japanese)

Okuma T, Kanda J, Tamura Y (1996) Windproof design of buildings. Kajima Syuppan-kai, 261pp.

(in Japanese)

Onodera N, Aoki T, Shimokawabe T, Kobayashi H (2013) A large-scale LES wind simulation using Lattice Boltzmann Method for a 10km × 10km area in Tokyo. High Perf. Comput. Symp., 123–131. (in Japanese)

Pomeroy JW, Gray DM, Landine PG (1993) The Prairie Blowing Snow Model: Characteristics, validation, operation. J. Hydrol., 144:165–192. doi: 10.1016/0022-1694(93)90171-5.

Qian Y, d'Humieres D, Lallemand P (1992) Lattice BGK models for Navier-Stokes equation. Europhys. Lett., 17:479–484. doi: 10.1209/0295-5075/17/6/001.

Qian YH, Succi S, Orszag SA (1995) Recent advances in lattice Boltzmann computing. Annu. Rev. Comput. Phys., 3:195–242. doi:10.1142/9789812830647_0006.

Saito H (1971) Visibility in Snow Storms. Research Report in National Research Institute for Earth Science and Disaster Resilience, 5:33–40. doi: 10.24732/nied.00000682. (in Japanese)

Saito K, Fujita T, Yamada Y, Ishida J, Kumagai Y, Aranami K, Ohmori S, Nagasawa R, Kumagai S, Muroi C, Kato T, Eito H (2006) The operational JMA nonhydrostatic mesoscale model. Mon. Weather Rev., 134:1266–1298. doi: 10.1175/MWR3120.1.

Sato Y, Nishizawa S, Yashiro H, Miyamoto Y, Kajikawa Y, Tomita H (2015) Impacts of cloud microphysics on trade wind cumulus: Which cloud microphysics processes contribute to the diversity in a large eddy simulation? Prog. in Earth and Planet. Sci., 2:23. doi: 10.1186/s40645-015-0053-6.

Schmidt RA (1982) Vertical profiles of wind speed, snow concentration, and humidity in blowing snow. Bound.-Layer Meteor., 23:2:223–246. doi: 10.1007/BF00123299.

Scotti A, Meneveau C, Lilly DK (1993) Generalized smagorinsky model for anisotropic grids. Physics of Fluids., 5:2306–2308. doi: 10.1063/1.858537.

Shao Y, Li A (1999) Numerical modelling of saltation in the atmospheric surface layer. Bound.-Layer Meteor., 91:199–225. doi:10.1023/A:1001816013475.

Shiotani M (1953) Note on the vertical distribution of density of blowing snow in the snow storm. Seppyo, 15:6–9. (in Japanese)

Smagorinsky J (1963) General circulation experiments with the primitive equations. I. the basic experiment. Mon. Wea. Rev., 91:99–164. doi:10.1175/1520-0493(1963)091<0099:GCEWTP>2.3.CO;2.

Suga K, Kuwata Y, Takashima K, Chikasue R (2015) A D3Q27 multiple-relaxation-time lattice Boltzmann method for turbulent flows. Comp. & Math. App., 69:518–529. doi:10.1016/j.camwa.2015.01.010.

Tabler RD (1980) Geometry and density of drifts formed by snow fences. J. Glaciol., 26:405–419. doi:10.3189/S0022143000010935.

Tabler RD (1986) Snow fence handbook (Release 1.0). Tabler and Associates, Laramie, Wyoming.

Tabler RD (1994) Design guidelines for the control of blowing and drifting snow. Strategic Highway Research Program Report SHRP-H-381.

Takemi T, Ito Rui (2020) Benefits of high-resolution downscaling experiments for assessing strong wind hazard at local scales in complex terrain: a case study of Typhoon Songda (2004). Prog. in Earth and Planet. Sci., 7:4. doi: 10.1186/s40645-019-0317-7.

Takeuchi M (1980) Vertical profile and horizontal increase of drift-snow transport. J. Glaciol., 26:481–492. doi:10.3189/S0022143000010996.

Takeuchi M, Fukuzawa Y (1976) On the Light Attenuation and Visibility in Snow drift. Seppyo, 38:4:165–170. doi: 10.5331/seppyo.38.4_165. (in Japanese)

Takeuchi M, Ishimoto K, Nohara T, Fukuzawa Y (1986) Dynamic threshold wind speed for suspension. Proc. the annual meeting of the Japanese Society of Snow and Ice. (in Japanese)

Takeuchi Y, Kobayashi S, Sato T, Izumi K, Kosugi K, Xin W, Zhang JP, Peng YH (2001) The effect of wind direction on drift control by snow fences. Annuals of Glaciology, 32: 159–162. doi: 10.3189/172756401781819175.

Tanji S, Inatsu M (2019) Case study of drifting snow potential diagnosis with dynamical downscaling. SOLA., 15:32–36. doi: 10.2151/sola.2019-007.

Tanji S, Inatsu M, Kawazoe S, Sato Y (2021) Blowing snow map of Hokkaido in 2017/2018 winter. Seppyo, 83:3:275–284. doi: 10.5331/seppyo.83.3_275. (in Japanese)

Tanji S, Inatsu M, Okaze T (2021) Development of a snowdrift model with the lattice Boltzmann method. Prog. in Earth and Planet. Sci., 8:57. doi: 10.1186/s40645-021-00449-0.

Tominaga Y, Mochida A, Murakami S, Sawaki S (2008) Comparison of various revised k–ε models and LES applied to flow around a high-rise building model with 1:1:2 shape placed within the surface boundary layer. J. Wind Eng. Ind. Aerod., 96:389–411. doi:10.1016/j.jweia.2008.01.004.

Tominaga Y, Mochida A, Okaze T, Sato T, Nemoto M, Motoyoshi H, Nakai S, Tsutsumi T, Otsuki M, Uamatsu T, Yoshino H (2011a) Development of a system for predicting snow distribution in built-up environments: combining a mesoscale meteorological model and a CFD model. J. Wind Eng. Ind. Aerod., 99:460–468. doi:10.1016/j.jweia.2010.12.004.

Tominaga Y, Okaze T, Mochida A (2011b) CFD modeling of snowdrift around abuilding: an overview of models and evaluation of a new approach. Build. Environ., 46:899–910. doi:10.1016/j.buildenv.2010.10.020.

Tomita H (2008) New microphysical schemes with five and six categories by diagnostic generation of cloud ice. J. Meteor. Soc. of Japan, 86:121–142. doi: 10.2151/jmsj.86A.121.

Uematsu T, Nakata T, Takeuchi K, Arisawa Y, Kaneda Y (1991) Three-dimensional numerical simulation of snowdrift. Cold Reg. Sci. Tech., 20:65−73. doi:10.1016/0165-232X(91)90057-N.

Vionnet V, Martin E, Masson V, Lac C, Bouvet F, Guyomarc'h G (2017) High-resolution large eddy simulation of snow accumulation in Alpine terrain. J. Geophys. Res., 122:11,005−11,021. doi:10.1002/2017JD026947.

Wang CB, Wang ZY, Xia T, Peng QS (2006) Real-time snowing simulation. Visual Comput,, 22:315–323. doi:10.1007/s00371-006-0012-8.

Wang X, Shangguan YQ, Onodera N, Kobayashi H, Aoki T (2014) Direct numerical simulation and large eddy simulation on a turbulent wall-bounded flow using Lattice Boltzmann Method and multiple GPUs. Math. Probl. Eng., 742432. doi:10.1155/2014/742432.

Wang YQ, Leung LR, Mcgregor JL, Lee DK, Wang WC, Ding Y, Kimura F (2004) Regional climate modeling: progress, challenges, and prospects. J. Meteor. Soc. of Japan, 82:1599–1628. doi: 10.2151/jmsj.82.1599.

Wang Z, Jia S (2018) A simulation of a large-scale drifting snowstorm in the turbulent boundary layer. The Cryosphere, 12:3841–3851. doi:10.5194/tc-12-3841-2018.

Watanabe T, Shimoyama K, Kawashima M, Mizoguchi Y, Inagaki A (2020) Large-Eddy Simulation of Neutrally-Stratified Turbulent Flow Within and Above Plant Canopy Using the Central-Moments-Based Lattice Boltzmann Method. Bound.-Layer Meteor., 176:35–60. doi:10.1007/s10546-020-00519-8.

Werner H, Wenglem H (1991) Large-eddy simulation of turbulent flow over and around a cube in a plate channel. In Proceedings of 8th Symposium on Turbulent Shear Flows, 155–158. doi:10.1007/978-3-642-77674-8_12.

White F (1974) Viscous fluid flow. McGraw-Hill Inc., US.

Xie ZT, Castro IP (2008) Efficient generation of inflow conditions for Large Eddy Simulation of street-scale flows. Flow Turbulence Combust, 81:449–470. doi:10.1007/s10494-008-9151-5.

Zhang J, Johnson PC, Popel AS (2008) Red blood cell aggregation and dissociation in shear flows simulated by lattice Boltzmann method. J. Biomech., 41:47–55. doi:10.1016/j.jbiomech.2007.07.020.

Zhang G, Zhang Q, Fan F, Shen S (2021) Numerical simulations of development of snowdrifts on long-span spherical roofs. Cold Reg. Sci. Tech., 182:103211. doi: 10.1016/j.coldregions.2020.103211.

Zhou X, Hu J, Gu M (2014) Wind tunnel test of snow loads on a stepped flat roof using different granular materials. Nat. Hazards, 74:1629–1648. doi:10.1007/s11069-014-1296-z.

Zwaaftink CDG, Diebold M, Horender S, Overney J, Lieberherr G, Parlange MB, Lehning M (2014) Modelling small-scale drifting snow with a Lagrangian stochastic model based on large-eddy simulations. Bound.-Layer Meteor., 153:117−139. doi:10.1007/s10546-014-9934-2.

Appendix A

The sensitivity test of the inflow turbulence was conducted with the snowdrift model in Chapter 3. We conducted the experiment with the laminar inflow and compared the snowdrift result with that of the three-dimensional experiment in Chapter 3. We use the same calculation setting with the experiment in Chapter 3 because the inflow turbulence generation needed large computational costs. The fence was set 4 m from the western boundary and was centered in the channel. The fence was non-porous, solid, and the thickness was 0.1 m, the height was 1 m and the length was 1.5 m. The channel size was 15.75 × 5 × 5 m, with the grid spacing at 0.05 m. The integration time was 30 s and we used the wind data after 10 s every 0.1 s in the conventional fluid dynamics module. The inflow turbulence was generated with the same method in Chapter 3 (Okaze and Mochida 2017; Xie and Castro 2008). The time-averaged wind speed in the experiment with the inflow turbulence and the laminar flow in the experiment without the inflow turbulence were 6 m s^{-1} westerly at 10 m aloft in the log profile [Eq. (4.5)].

Figure A shows the difference of the snowdrift height between the experiment with the laminar inflow and that with the inflow turbulence. In the most area, the difference was under 0.1 m. In the cross-section along $y = 2.5$ m, the snowdrift peak height and the peak position with the laminar inflow corresponded to those with the inflow turbulence. However, the result with the inflow turbulence had over 0.1 m higher snowdrift than that with the laminar inflow in front of the fence (Fig. Aa). The cross-section along $y = 2.5$ m displayed this difference was made by the unsmooth formation in the laminar flow experiment (Fig. Ab). We considered that this was because the number of wind data in Tanji et al. (2021) in this experiment was so few, which was 200. However, the snowdrift shape was expected be smooth and be same with that with the inflow turbulence even in the laminar inflow experiment because 3600 number of wind data was used in

Chapter 4. Therefore, we used the laminar inflow in Chapter 4.

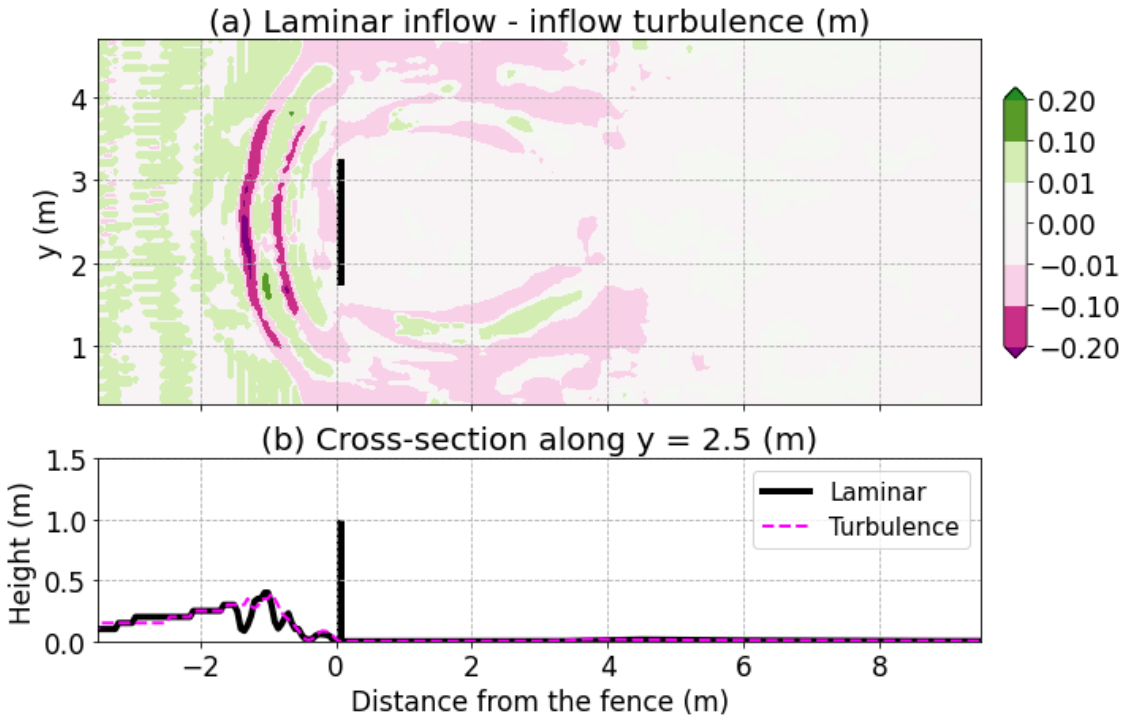

Fig. A (a) The difference between the result of snowdrift height in the laminar inflow experiment and the inflow turbulence experiment. Green areas show the areas where snowdrift with the laminar inflow is higher than that with the inflow turbulence. Pink areas show the opposite. (b) Snowdrift height in the cross-section along y = 2.5 m in the laminar inflow experiment (a solid black line) and in the inflow turbulence experiment (a pink broken line). Black solid lines in (a) and (b) show the fences.